Large Volume Artefact for Calibration of Multi-Sensor Projected Fringe Systems

by

Tahir Rehan Tarvaz

A Doctoral Thesis
submitted in partial fulfilment of the requirements
for the award of
Doctor of Philosophy of Loughborough University

April, 2015

Abstract

Fringe projection is a commonly used optical technique for measuring the shapes of objects with dimensions of up to about 1 m across. There are however many instances in the aerospace and automotive industries where it would be desirable to extend the benefits of the technique (e.g., high temporal and spatial sampling rates, non-contacting measurements) to much larger measurement volumes. This thesis describes a process that has been developed to allow the creation of a large global measurement volume from two or more independent shape measurement systems.

A new 3-D large volume calibration artefact, together with a hexapod positioning stage, have been designed and manufactured to allow calibration of volumes of up to $3 \times 1 \times 1$ m^3. The artefact was built from carbon fibre composite tubes, chrome steel spheres, and mild steel end caps with rare earth rod magnets. The major advantage over other commonly used artefacts is the dimensionally stable relationship between features spanning multiple individual measurement volumes, thereby allowing calibration of several scanners within a global coordinate system, even when they have non-overlapping fields of view.

The calibration artefact is modular, providing the scalability needed to address still larger measurement volumes and volumes of different geometries. Both it and the translation stage are easy to transport and to assemble on site. The artefact also provides traceabitity for calibration through independent measurements on a mechanical CMM. The dimensions of the assembled artefact have been found to be consistent with those of the individual tube lengths, demonstrating that gravitational distortion corrections are not needed for the artefact size considered here. Deformations due to thermal and hygral effects have also been experimentally quantified.

The thesis describes the complete calibration procedure: large volume calibration artefact design, manufacture and testing; initial estimation of the sensor geometry parameters; processing of the calibration data from manually selected regions-of-interest (ROI) of the artefact features; artefact pose estimation; automated control point selection, and finally bundle adjustment. An accuracy of one part in 17 000 of the global measurement volume diagonal was achieved and verified.

Acknowledgements

Financial support through a scholarship from Loughborough University and Airbus UK is greatly acknowledged and appreciated. My sincerest gratitude goes to my supervisor, Prof. Jon Huntley for his help, guidance and academic support throughout the research period. I would also like to thank the engineers at both Airbus and Phase Vision Ltd for all their help and technical assistance, Mr Amir Kayani, Dr Richard Burguete, Dr Russell Coggrave, Dr Martin Davies and Mr Dave Sanderson.

Also appreciated is Dr Jon Petzing for his useful input and discussions on calibration in metrology. Many thanks go to Mr Jagpal Singh for providing assistance and support; in particular whenever I had to use the mechanical coordinate measuring machine (CMM) for performing the numerous measurements on my artefacts. My sincere appreciation goes to Dr Michael McCarthy and his team at the National Physical Laboratory (NPL) for allowing me access and use of their facilities and equipment.

I would like to thank members of the Optical Engineering Research Group for their invaluable help and discussions. To my friends at Loughborough and beyond, for your constant encouragement and friendship, you have my sincere gratitude.

Finally, I would like to thank my family for their patience, understanding and unwavering support through several years of study.

Table of Contents

Chapter 1

Introduction

1.1. Background

Metrology or the science of measurement plays a vital role in almost every aspect of modern society [1]–[4]. An incorrect measurement can have a tremendous economical and societal impact [5]. A measurement can be defined as the process of gathering information from the physical world [6]. Consequently, a major aspect of metrology is focussed on characterising through physical quantities, the shape of objects present in the physical world. The shape of an object (or object shape) can be described by the geometric features that are attributed to that object in space, whether it is one-dimensional (1-D), two-dimensional (2-D) or three-dimensional (3-D).

These geometric features refer to the different types of curves and surface profiles present in an object, which when combined together through measurement, can be used to describe the object. Hence, the measured shape of an object offers a unique way for describing and identifying that object. Advanced improvements in computer aided design (CAD) and computer aided manufacture (CAM), has meant that real life objects with multifaceted shapes can be designed on a computer and then subsequently manufactured. Dimensional measurements of these shapes is very important in manufacturing, since there is a requirement for high accuracy [7]. As a result, industries that manufacture objects require quick and accurate shape measurements.

Computer aided design (CAD) is also relied upon heavily by Designers and Engineers in industry for conceptualising their ideas and/or products. When a designed product is manufactured, it is often essential that the manufactured product is measured and validated against the dimensions detailed in the design specification, e.g. against an engineering drawing or a CAD model. In industry, the most common type of instrument for measuring object shape, to high accuracy, is a mechanical coordinate measuring machine (CMM). A mechanical CMM will typically measure object shape by

physically probing points at as many different locations on the object as possible. In more recent times, optical shape measurement systems (SMS) have also been developed.

Optical SMSs eliminate the need to make contact with the object surface when carrying out measurements [8], [9], and provide considerably more 3-D coordinates in much shorter timescales in comparison to CMMs. Optical SMSs also have the capability of making 360 degree measurements by combining multiple sensors. However, the environmental conditions that optical SMSs often require for their correct functionality, has limited their use in industry to date. For example, environmental conditions typically found at industrial sites, such as low frequency vibration, uncontrolled temperature and background illumination, adversely affects measurement accuracy and reliability [10]. The rigorous nature of calibration, measurement setup time and procedure, are all further issues that affect overall measurement accuracy.

This chapter aims to provide an introduction to the thesis by highlighting the projects aims and objectives. Some of the principal concepts of measurement, namely accuracy, precision, uncertainty and traceability, are presented. Mechanical CMMs and optical SMSs as measurement instruments, alongside the measurement principle of an optical SMS, are explained further. The chapter closes by outlining the scope of the thesis by indicating the key discussion points in the following chapters.

1.2. Project aims and objectives

Shape measurements of 3-D objects using optical methods have been developing rapidly over the last ten to twenty years [11]. These developments have largely been driven by the demands of industries looking for fast and accurate measurements of components. Hence, a wide variety of optical shape measurement techniques have been developed for measuring 3D objects to high accuracy. These include; time of flight, laser scanning, moiré, photogrammetry, interferometry and projected structured light [10], [12]. Despite all of these measurement techniques, the technique that will be focussed on for this project will be projected structured light systems, and more specifically, projected fringe systems. Any reference from now on to an optical SMS will be to a projected fringe system that projects sinusoidal intensity patterns [11].

Research has been on-going at Loughborough University since 1996 on an optical SMS based on the projection of sinusoidal fringe patterns using low cost data projector(s) and digital camera(s) to obtain 3-D coordinates [10], [13]–[18]. Advances in the technology since then have led to a patented measurement technique that involves projecting a sequence of computer-generated patterns of light and dark horizontal and vertical fringes onto the object being measured, using a spatial light modulator (SLM) e.g. as found in a data projector. Decoding of the fringe pattern from a digital camera, whose optical axis is off-set by a fixed angle with respect to that of the projector, allows a depth value to be calculated at each camera pixel. A university spin-out company, Phase Vision Ltd, was setup to assist in the transfer of this technology to industry.

The SMS developed by Phase Vision Ltd, based on one digital camera and one data projector, has a high scan rate of order 10^6 3-D coordinates s^{-1}. The 3-D coordinates calculated, produce a 'point cloud'. The 'point cloud', representing the geometric shape of the object under inspection, can then be exported to other software tools for inspection and further analysis. In terms of application, this project aims to extend the use of projected fringe SMS technology for larger volume metrology. The SMS offers measurement accuracy of around one part in 20,000 across the measurement volume diagonal [17], [18], e.g. around 50 μm over a measurement dimension of order 1 m across. In order to measure larger volumes than this and to allow multiple views from different directions to overcome occlusion problems, it becomes desirable to link multiple SMSs contiguously. Therefore, the primary objective of this work is the development of a calibration method suitable for a multi-sensor optical SMS arrangement, that expands the measurement volume diagonal that can be calibrated from the current ~1 m across to ~3 m across.

The calibration process initially developed by Ogundana [19], is further enhanced in this work for linking adjacent SMSs with non-overlapping measurement volumes, and still provides a fast, user friendly and traceable calibration. The model is based on a photogrammetric approach, which combined with the advantages of a projected fringe system that has high coordinate output, provides for a robust and accurate calibration

[20]. The individual parameters are described for the principal sensors in the optical SMS (14 in total, including three translation parameters, three rotation parameters (Euler angles), perpendicular distance of sensor pinhole from image plane (the principal distance), principal point in the image plane axes, and five lens distortion parameters). The calibration process is useable over large measurement volumes, while providing high precision over large areas of object surface at any one time, and integrates the means of linking multiple SMSs.

1.3. Fundamental concepts of measurement

1.3.1. Accuracy, precision and uncertainty

In the modern world, metrology plays a vital role to protect the consumer and to ensure that manufactured goods conform to approved dimensional and quality standards [1], [2]. The terms 'accuracy' and 'precision', are regularly used wrongly and interchangeably. The accuracy of a measurement is the degree of closeness to the true value, a quantity whose value has in principle been measured without error [1], [6]. It should also be noted that the standard metrology temperature when trying to determine the accuracy of a measurement is fixed at 20° C. The precision of a measurement is the degree of scatter of the measurement result, when the measurement is repeated a number of times under specified conditions [1]. Although the term precision is used only in the general sense, it cannot be quoted as a numerical characteristic of a measurement system [6].

In reality, the true value of a measurement cannot be obtained experimentally, whichever measurement process is used there will always be error in the measurement [21]. A measurement must therefore be accompanied by a corresponding value stating the level of correctness of the stated result. Here, the concept of measurement 'uncertainty' is introduced to help quantify what the correctness from the true value should be [22]–[25]. The only way to obtain an estimate of the uncertainty is to use a higher level measurement standard in place of the measuring instrument to perform the measurement [21]. Measurement uncertainty is a statement of how well someone thinks they have measured something. It can therefore be considered as a guide to the quality of the measurement that can be used to compare results in a meaningful manner.

Uncertainty evaluations are normally used to quantify the repeatability of a measurement process using both statistical and non-statistical methods, referred to as 'Type A' and 'Type B' evaluations respectively [22], [26]–[28]. Repeatability refers to the closeness of the agreement between results of successive measurements carried out under the same conditions of measurement within a relatively short interval of time [1]. There is also reproducibility, which refers to the closeness of agreement between results of successive measurements carried out under changed conditions of measurement [1]. Reproducibility is rarely computed in metrology, though widely used and useful in certain cases [1]. Generally, in a Type A evaluation, the standard deviation of the mean is calculated and quoted as the standard uncertainty of a set of measurements. Individual sets of measurements might not follow a normal distribution, but the average values of many sets of measurements will generally have a normal distribution [21].

All Type B uncertainties associated with a set of measurements must be evaluated by scientific judgement. Using all possible sources of information, a metrologist is required to draw on experience and general knowledge about processes to make reliable decisions regarding Type B uncertainties. It must be emphasised though that Type B uncertainties are usually the most difficult to evaluate due to rigorous scientific methodology required to substantiate a particular position about uncertainty. If treated in a trivial manner, components of Type B uncertainties can produce meaningless results. Possible information about Type B contributions can come from [21]:

- previous measurement data on the same or similar system(s),
- manufacturer's specifications,
- figures from calibration certificates,
- uncertainties associated with reference data from handbooks,
- previous experience with the behaviour of certain instrumentation.

Once both Type A and Type B uncertainties have been established, they must be combined into one number, usually referred to as the 'combined standard uncertainty'. The combined standard uncertainty is calculated by quadrature addition, it is the

combined standard uncertainty that is normally quoted as the overall measurement uncertainty of the measurement process [21]. The combined standard uncertainty can be multiplied by a coverage factor, k, to provide a greater level of confidence, e.g. the coverage factor, k, for 95% confidence is 1.96.

1.3.2. Measurement standards

Measurement standards can be categorized into levels based on metrological quality or geographical location [1], [2], [29], [30]. With regard to metrological quality, the different levels of measurement standards include:

1. primary
2. secondary
3. working

Primary standards have the highest metrological quality and their values are not referenced to other standards of the same quantity [1], [2], [29], [30]. The International Bureau of Weights and Measures (BIPM) is the body responsible for upholding the primary standards to which national physical standards laboratories of different countries reference their standards to. The National Physical Laboratory (NPL) of the UK and Physikalisch-Technische Bundesanstalt (PTB) of Germany are two examples of national physical standards laboratories. The International System (SI) of units is the current form of the metric metrology system. The base units are metre, kilogram, second, ampere, mole, Kelvin and candela.

For example, the base unit of length, the metre, is defined by the BIPM as "the length of the path travelled by light in vacuum during a time interval of 1/299 792 458 of a second" [1]. It is from these base units that other units are derived for quantities such as velocity, acceleration, momentum, etc. Secondary standards are standards whose values are assigned by comparison with the primary standards of the same quantity [1], [2], [29], [30]. A working standard, is a standard used to calibrate or check the accuracy of measurement instruments [1]. Industrial and general purpose measuring instruments

have a working standard metrological quality. The hierarchy by geographical location within a given country can be categorised into the following levels [1], [2]:

1. international standard
2. national standard
3. tertiary standard

Usually, the national hierarchy scheme is incorporated in the metrology law of the country [1], [2]. The upkeep of a hierarchy of measurement standards provides the key concept to traceability in metrology. The traceability of a measuring instrument indicates that its value has been determined by an unbroken chain of comparisons with a series of higher level standards with stated uncertainties [1]. Strict guidelines are set by national bodies for maintaining traceability, as it is largely dependent on the type of measurement instrument and the time interval between comparisons [1].

1.4. Coordinate measuring machines

Mechanical coordinate measuring machines (CMMs) are used to gather 3-D point data from objects to help define the shape of the objects they are measuring. The CMM is assisted by computer software that allows it to compute through algorithms, from the measured points, many different types of dimensional quantities. These range from but are not limited to: the position of features within the calibrated measurement volume, distance between the position of features, sizes of features, and the different forms of features, such as flatness, circularity, cylindricity and the angular relationships between features such as perpendicularity [31], [32].

Traditional mechanical CMMs measure object shape by probing the surface at many distinct measuring points using suitably sized touch probes. Usually, they consist of a granite base, main structure (bridge, horizontal, vertical, gantry etc.), and a probing system consisting of a probe head with stylus, stylus tip (normally made of Ruby), and computer software. A list of the major CMM manufacturers would include Zeiss, Metris LK, Leitz, Mitutoyo and Hexagon Metrology. The cost of mechanical CMMs is directly reliant on measurement accuracy, which is determined through the calibration process

set out in ISO 10360 [33]. This specifies the attainable accuracy of measurement, together with probing error and scanning error. The overall accuracy will also be affected by other influences such as structural, hygral and thermal stability of all critical components, type of probe stylus and head selected, and the quality of the computer software used. For example, a mechanical CMM with a maximum permissible length error of 0.9 µm + $^{L}/_{400}$ and maximum volume error of 1.3 µm + $^{L}/_{400}$, where L = length in mm within the measurement volume, probing error of 1.5 µm and scanning error of 1.5 µm in 45 s, can cost as much as £150k.

Although mechanical CMMs can produce high accuracy measurements, their major shortcoming includes the need for contact with the surface of the object being measured within the localised measurement volume [10]. Under certain circumstances it can be difficult or even impossible to use a CMM for example when dealing with fragile or compliant samples. This limitation has led to a large interest in developing optical metrology techniques and systems [10].

1.5. Optical shape measurement system

Optical SMSs provide a non-contact means of evaluating the physical properties of 3-D objects, and can measure millions of coordinates in the space of a few seconds, making them a significantly quicker alternative to mechanical CMMs. Other benefits include lower inspection costs; leading to fewer defects and faster production times [34]. A list of the major optical SMS manufacturers would include Phase Vision, Steinbichler, Gom, Breuckmann and Cognitens. The steps involved in the data acquisition and processing chain of the Phase Vision optical SMS include: phase measurement, calibration, data processing and data presentation [35].

1.5.1. Phase Measurement

Phase measurement is the term used to describe the data acquisition process for the 3-D coordinates in an optical SMS based on projected fringes or interferometry. Non-contact measurement of a surface profile is usually dependent on techniques based on image cues, triangulation, projection of structured light and various interferometric methods –

including wavelength change, displacement of the test surface and shifting the illumination beams [10]. Passive profile sensors measure the test surface under natural illumination by examining image cues such as shading, while active profile sensors typically require temporal control of the illumination, focus, or relative position of the test surface [10].

In an optical SMS, locating a point **P** (*X*,*Y*,*Z*) on the surface of an object requires input from both the camera and projector. Coordinates (*X*,*Y*) are translated from the camera image plane, while (*Z*) is decoded from the intensity values of the 2-D light (fringe) patterns projected on to the objects surface. The projection of these fringe patterns produces a sequence of intensities across the measurement volume that uniquely identifies each section within it. The 2-D fringe pattern (or interferogram) can be represented by the following continuous intensity function [10]:

$$I(m,n) = I_0(m,n) + I_M(m,n)\cos\phi(m,n) \tag{1-1}$$

where (m,n) = spatial coordinates in the reference frame of the image,
$I_0(m,n)$ = background illumination,
$I_M(m,n)$ = intensity modulation,
$\phi(m,n)$ = phase term related to the physical quantity being measured.

Due to the nature of the arctangent function for phase, phase values and phase change values are normally wrapped back in the principal range [$-\pi,\pi$], before continuing on with the phase unwrapping process. The relationship between the wrapped phase and unwrapped phase may be stated as [10]:

$$\phi(m,n,t) = \phi_W(m,n,t) + 2\pi v(m,n,t) \tag{1-2}$$

where $\phi(m,n,t)$ = the unwrapped phase at time, t,
$\phi_W(m,n,t)$ = the wrapped phase at time, t,
$v(m,n,t)$ = an integer valued correcting field at time, t.

The *wrapped* phase is *unwrapped* using an appropriate phase unwrapping algorithm. In the present optical SMS, the *temporal phase unwrapping* technique is used, the phase values and phase change values are unwrapped independently at each pixel, and as a function of time. The main advantages of temporal phase unwrapping are that it is inherently simple to implement, and that phase maps with discontinuities are unwrapped correctly. The main drawbacks are that the computational effort needed is substantial, and that rapid sampling of the phase as a function of time is required [10], [16], [17], [36].

1.5.2. Calibration

Calibration is defined as a traceable process, which correctly calculates values of parameters in a calibration model, so that measured phase values can be converted into accurate real world Cartesian coordinates. In the context of the optical SMS this can also be referred to as the process that determines the external and internal parameters of the camera and projector. There are 14 external and internal parameters in total per sensor (the camera and projector are both regarded as sensors); three translational parameters, three rotational parameters, principal distance (i.e. the distance of sensor pinhole to the image plane along the optical axis), image plane coordinates of the optical axis, three radial distortion parameters and two tangential distortion parameters. Calibration also forms the coordinate system of the SMS; measurements captured by the SMS post calibration are measured relative to this coordinate system, hence it is essential that the calibration process is as accurate as possible.

1.5.3. Data processing and presentation

When measurements are taken by the optical SMS; many ‘point clouds’ containing large amounts of data are produced (approximately 200 Gb for every measurement dataset). Managing this data so that it is efficient to process and can be easily presented is essential. This is largely achieved by allowing the ‘point clouds’ to be converted to file formats that are suitable for importing into visualisation and/or inspection software. Nevertheless, due to the large amounts of data, careful consideration still needs to be given to structuring the data in readiness for processing efficiently, thus minimising processing time.

1.6. Thesis outline

In Chapter 2, calibration methods utilised in photogrammetry and computer vision are discussed. A mathematical model for sensor calibration is described in terms of the sensor parameters that govern both the sensor imaging geometry and the real world Cartesian coordinates. The novel calibration process developed for multiple-sensors in this work, for extending the use of the optical SMS for larger volumes is also described.

The challenges involved in designing and developing the calibration artefact necessary for utilising the calibration process are highlighted in Chapter 3. The complete design process including the design intent alongside the structural analysis carried out is fully explained.

The detailed design and subsequent manufacture of the positioning device used for manipulating the large volume calibration artefact is discussed in Chapter 4. Proof of principle experiments are carried out to validate the robustness of the manipulator.

Chapter 5 focuses on the experimental analysis of measurement errors that are present due to the nature of the optical SMS and the feature geometry of the calibration artefact. Proof of principle experiments are carried out to show the magnitude of the errors present during measurement, and the best practice for accounting for these errors.

The application of the calibration process for working with larger volumes is described in Chapter 6. The methods used for optimising data extraction for bundle adjustment is also described. Also discussed in this chapter are the experimental results for calibrating the larger volume multi-sensor SMS setup, while utilising the large calibration artefact.

Finally, in Chapter 7, overviews of the main novel aspects of the work are discussed, and recommendations for further work are suggested.

1.7. Figures

Figure 1-1: Phase Vision Ltd optical shape measurement system, SMS1200, introduced to the market in 2009.

Figure 1-2: A mechanical CMM with a bridge structure.

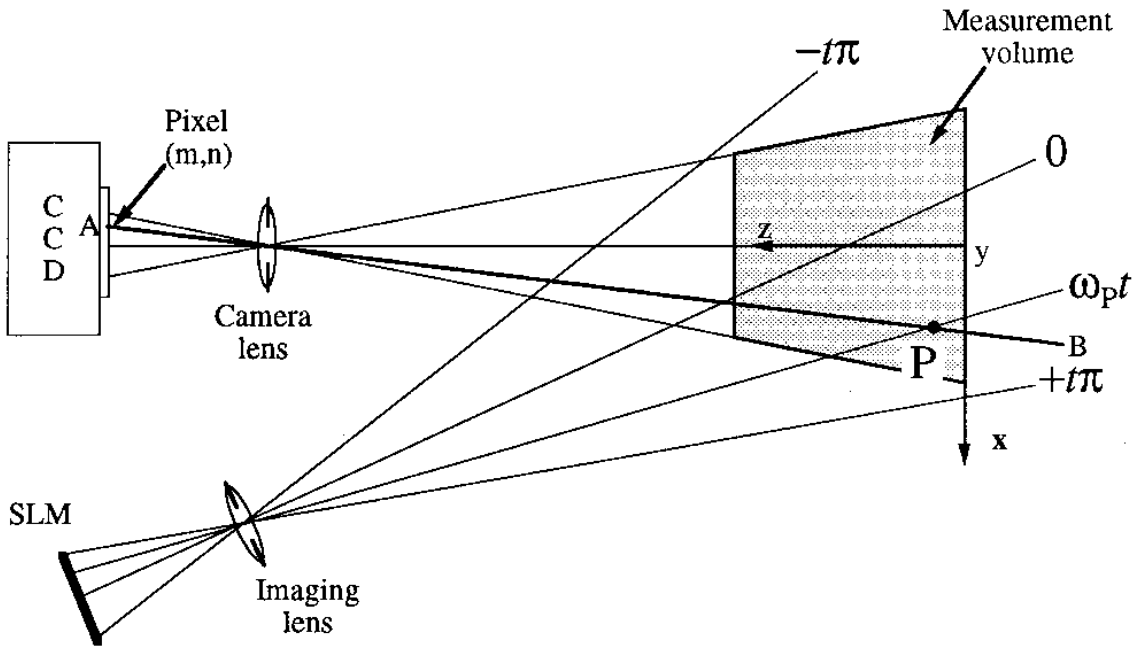

Figure 1-3: Measurement principle of the optical SMS; locating point **P** (x,y,z) involves contributions from both the camera and projector (SLM) [17].

Chapter 2

Literature review

2.1. Calibration methods

The imaging sensor and light source are crucial factors for overall accuracy in optical 3-D shape measurement systems (SMS) [12]. Crucial factors for an imaging sensor (usually a charge coupled device (CCD) or charge injection device (CID)), are speed, dynamic range and accuracy. For the light source they include weight, intensity profile and speckle or dot size [12]. Calibration techniques of optical 3-D SMSs typically refer to the use of a calibration artefact, the number of images required and the implementation used to estimate the calibration parameters [20]. In a structured light system, the measured values are the phase values of projected fringes, and the pixel or image coordinates of a camera [20].

In this chapter, the major areas of discussion will focus on sensor calibration techniques in the photogrammetry and computer vision fields. The direct linear transformation (DLT) method used when estimating the sensor parameters is described. The bundle adjustment process is also explained, along with how it is integrated into the calibration process developed for the optical SMS.

2.2. Sensor calibration techniques

2.2.1. Calibration in photogrammetry

Photogrammetry can be defined as the "science of measuring in photos", which allows modelling of 3-D object space using 2-D images [37]–[39]. It is an optical metrology technique that forms the geometric relationship between the captured image and the object measured, as it existed at the time of the imaging event [40]. This geometric relationship is expressed as a mathematical model of the camera as a projective geometry (as shown in Figure 2-1), where the purpose of the calibration process is to efficiently and accurately estimate the parameters that describe the camera model. The

measurement accuracy depends on the illumination conditions, the noise of the image recording, the camera resolution, and on the geometry of the stereo arrangement [41].

The following mathematical model is based on that presented by Schreiber and Notni [20], which in turn follows the analysis in the classic photogrammetry text book of Kraus [42], where the lenses of the sensors are represented as pinholes with compensation for lens distortion. From Figure 2-1 the following can be expressed:

$$\begin{bmatrix} \xi_M^{(c)} \\ \eta_M^{(c)} \end{bmatrix} = -\frac{c}{z'}\begin{pmatrix} x' \\ y' \end{pmatrix} + \begin{pmatrix} \xi_H \\ \eta_H \end{pmatrix} \tag{2-1}$$

where $\xi_M^{(c)}$, $\eta_M^{(c)}$ = image coordinates,

x', y', z' = auxiliary coordinate system, with its origin in the projection centre and the x'-y' plane parallel to the ξ-η plane of the image coordinate system (not shown in Figure 2-1),

c = camera constant, the distance between the projection centre and image plane along the optical axis, i.e. the perpendicular distance to the image plane,

ξ_H , η_H = image coordinates of the principal point.

Deviations $d\xi$ and $d\eta$ from the image plane origin can be described with functions that contain additional parameters. For example, as given in [20], the correction for radial distortion can be written as:

$$d\xi = \left(\xi_M^{(c)} - \xi_H^{(c)}\right)(k_1 r^2 + k_2 r^4 + k_3 r^6 + \cdots) \tag{2-2}$$

$$d\eta = \left(\eta_M^{(c)} - \eta_H^{(c)}\right)(k_1 r^2 + k_2 r^4 + k_3 r^6 + \cdots) \tag{2-3}$$

with $$r = \left[\left(\xi_M^{(c)} - \xi_H^{(c)}\right)^2 + \left(\eta_M^{(c)} - \eta_H^{(c)}\right)^2\right]^{1/2}$$

$k_1, k_2, k_3 \ldots$ are referred to as radial distortion parameters.

In [43], Chen concludes that k_1 is the most significant distortion parameter, and is typically sufficient for an accurate model [43]. Hence, Eqn. (2-1) can be written with the additional terms to take account of distortion.

$$\begin{bmatrix} \xi_M^{(c)} \\ \eta_M^{(c)} \end{bmatrix} = -\frac{c}{z'}\begin{pmatrix} x' \\ y' \end{pmatrix} + \begin{pmatrix} \xi_H \\ \eta_H \end{pmatrix} + \begin{pmatrix} d\xi \\ d\eta \end{pmatrix} \tag{2-4}$$

The change from the local coordinate system to the world coordinate system is made by a six-parameter transformation:

$$\begin{pmatrix} x' \\ y' \\ z' \end{pmatrix} = \mathbf{R}(\omega, \phi, \kappa)\begin{bmatrix} x_M - x_O^{(c)} \\ y_M - y_O^{(c)} \\ z_M - z_O^{(c)} \end{bmatrix} \tag{2-5}$$

where x_M, y_M, z_M = world coordinates of the object,

$x_O^{(c)}, y_O^{(c)}, z_O^{(c)}$ = world coordinates of the projection centre,

ω, ϕ, κ are Euler angles (see Figure 2-2),

$\mathbf{R}(\omega, \phi, \kappa)$ = orthonormal rotation matrix, which rotates the world coordinate system parallel to the auxiliary system.

$$\mathbf{R} = \begin{bmatrix} r_{11} & r_{12} & r_{13} \\ r_{21} & r_{22} & r_{23} \\ r_{31} & r_{32} & r_{33} \end{bmatrix}$$

$$= \begin{bmatrix} \cos\phi\cos\kappa & \cos\omega\sin\kappa + \sin\omega\sin\phi\cos\kappa & \sin\omega\sin\kappa - \cos\omega\sin\phi\cos\kappa \\ -\cos\phi\sin\kappa & \cos\omega\cos\kappa - \sin\omega\sin\phi\sin\kappa & \sin\omega\cos\kappa + \cos\omega\sin\phi\sin\kappa \\ \sin\phi & -\sin\omega\cos\phi & \cos\omega\cos\phi \end{bmatrix}$$

From this, the relationship between the image coordinates $\xi_M^{(c)}$ and $\eta_M^{(c)}$ and the coordinates x_M, y_M, and z_M (i.e. object space) is given by:

$$\left[\xi_M^{(c)} - \xi_H^{(c)}\right](k_1 r^2 + k_2 r^4 + k_3 r^6 + \cdots) = -c\frac{r_{11}\left(x_M - x_0^{(c)}\right) + r_{12}\left(y_M - y_0^{(c)}\right) + r_{11}\left(z_M - z_0^{(c)}\right)}{r_{31}\left(x_M - x_0^{(c)}\right) + r_{32}\left(y_M - y_0^{(c)}\right) + r_{33}\left(z_M - z_0^{(c)}\right)}$$

and (2-6)

$$\left[\eta_M^{(c)} - \eta_H^{(c)}\right](k_1 r^2 + k_2 r^4 + k_3 r^6 + \cdots) = -c\frac{r_{21}\left(x_M - x_0^{(c)}\right) + r_{22}\left(y_M - y_0^{(c)}\right) + r_{23}\left(z_M - z_0^{(c)}\right)}{r_{31}\left(x_M - x_0^{(c)}\right) + r_{32}\left(y_M - y_0^{(c)}\right) + r_{33}\left(z_M - z_0^{(c)}\right)}$$

In photogrammetry, the known 3-D coordinates (referred to as control points) are measured as part of the calibration process, and the 'bundles' of light rays are adjusted in a minimisation process called bundle adjustment. 'Calibration' in photogrammetry is generally used to refer to the acquisition of only the internal lens parameters and the lens distortion parameters, thus providing a quantitative interpretation of the imaging geometry of the camera used, and its lens. A 'calibrated' camera is therefore one where the internal and lens distortion parameters are obtainable [40], [44].

Acquiring the external parameters of a camera, i.e. its position and orientation in 3-D space, is known as *resection*. The resection of a camera requires at least three non-collinear control points to be measured, assuming the internal parameters are known [40], [44]. The process of computing real world coordinates from image coordinates utilising the camera parameters, is known as *intersection.* Consequently, *resection* is only a transitional stage which is typically followed by *intersection* or bundle adjustment [40], [44]. Bundle adjustment is the process of refining a visual reconstruction to produce jointly optimal 3-D structure (real world coordinates) and viewing parameter (internal and/or external) estimates [45]. This means that the

parameter estimates are found by minimising some non-linear cost function that quantifies the model fitting error [45]. Cost functions can be put into two main groups: those based on minimising an algebraic error, and those based on minimising a geometric or statistical image distance [46].

The addition of extra parameters into the bundle adjustment came about as the need for determining the internal geometry of the camera to high accuracy became greater. Determining the extra parameters, expressed in Eqn. (2-6), is required for high accuracy to be achievable. These parameters include radial distortion, tangential distortion, out-of-plane and in-plane image distortion [47], [48]. As a result Eqn. (2-2) can now be expressed as:

$$d\xi = d\xi_r + d\xi_d + d\xi_u + d\xi_f \tag{2-7}$$

where $d\xi_r$ = radial distortion, $d\xi_d$ = tangential distortion, $d\xi_u$ = image plane unflatness, $d\xi_f$ = in-plane distortion.

Further details on how to optimally model the effect of such additional parameters, and lens calibration methods, can be found in key photogrammetry papers and books such as [42], [44], [48].

2.2.2. Calibration in computer vision

Computer vision deals with the extraction of 3-D information from images captured by cameras in many forms, such as video sequences, views from multiple cameras or multi-dimensional data. Stereo-vision is the most popular method of computer vision; this method uses two cameras to capture 2-D images of a 3-D object from different viewing angles, and through triangulation, recreates the 3-D scene [49]. The pin-hole camera model is usually used in stereo-vision to determine the unknown parameters of the model. Determining these camera parameters is referred to as calibration.

The models for calibration in computer vision mostly have their foundation in photogrammetry, and the sensor model is similar to the one described in section 2.2.1.

In computer vision, the conversion from 2-D image points to 3-D world coordinates is usually expressed as a linear mapping of homogeneous coordinates as follows:

$$\mathbf{U} = \mathbf{VM} \tag{2-8}$$

where **U** = image point coordinates expressed as $\mathbf{U} = [\mathbf{U_1}\mathbf{U_2}\mathbf{U_3}]^T$, where $\mathbf{U_1}$ and $\mathbf{U_2}$ are column vectors with $\mathbf{U_3}$ a column vector of ones,

V = a 3×4 matrix, called the *camera matrix*,

M = object space points expressed as $\mathbf{M} = [\mathbf{M_1}\mathbf{M_2}\mathbf{M_3}\mathbf{M_4}]$, where $\mathbf{M_i}$ (i = 1…4) are column vectors.

The camera matrix can be further expressed as:

$$\mathbf{V} = \mathbf{KE} \tag{2-9}$$

where **K** is an upper triangular 3x3 matrix, called the camera calibration matrix, which contains the camera's internal parameters.

E is a 3x4 matrix, which contains the camera's external parameters.

Further details on the various models utilised in computer vision can be found in reference [46].

The drawbacks with this type of linear calibration technique or indeed any linear calibration technique is that they are not optimal estimators, and they ignore lens distortion [50], [51]. The latter point is not necessarily a fundamental obstacle: Chen [43] for example advises that when the distortion parameters are negligible, trying to recover them would lead to over-parameterisation, which could affect the calibration process. Despite the deficiencies, they are computationally efficient and provide a good starting point for iterative methods (usually non-linear methods), enhancing the latter's ability to converge to a global minimum.

2.2.3. Direct linear transformation (DLT)

The DLT method [52] has its roots in both the photogrammetry and computer vision fields for initialising internal and external sensor parameters, which are then further refined by some other iterative method. If no distortion is present, the 3-D DLT between a point (x_M, y_M, z_M) in object space and its corresponding image coordinates $\left(\xi_M^{(c)}, \eta_M^{(c)}\right)$ can be expressed by the linear fractional equations:

$$\xi_M^{(c)} = \frac{L_1 x_M + L_2 y_M + L_3 z_M + L_4}{L_9 x_M + L_{10} y_M + L_{11} z_M + 1}$$

and (2-10)

$$\eta_M^{(c)} = \frac{L_5 x_M + L_6 y_M + L_7 z_M + L_8}{L_9 x_M + L_{10} y_M + L_{11} z_M + 1}$$

where L_i (i = 1,…,11) are known as the DLT parameters.

These equations are based on the collinearity condition that the object point, pinhole, and ideal image point all lie on a straight line. The equation above, Eqn. (2-10), can be written in matrix form also:

$$\begin{bmatrix} \xi_M^{(c)} \\ \eta_M^{(c)} \end{bmatrix} = \begin{bmatrix} x_M & y_M & z_M & 1 & 0 & 0 & 0 & 0 & -\xi_M^{(c)} x_M & -\xi_M^{(c)} y_M & -\xi_M^{(c)} z_M \\ 0 & 0 & 0 & 0 & x_M & y_M & z_M & 1 & -\eta_M^{(c)} x_M & -\eta_M^{(c)} y_M & -\eta_M^{(c)} z_M \end{bmatrix} \begin{bmatrix} L_1 \\ L_2 \\ L_3 \\ L_4 \\ L_5 \\ L_6 \\ L_7 \\ L_8 \\ L_9 \\ L_{10} \\ L_{11} \end{bmatrix} \quad (2\text{-}11)$$

This can be simplified to:

$$\begin{bmatrix} \xi_M^{(c)} \\ \eta_M^{(c)} \end{bmatrix} = \mathbf{ML} \tag{2-12}$$

where $\mathbf{M} = \begin{bmatrix} x_M y_M z_M 1 & 0 & 0 & 0 & 0 & 0 & -\xi_M^{(c)} x_M & -\xi_M^{(c)} y_M & -\xi_M^{(c)} z_M \\ 0 & 0 & 0 & 0 & x_M y_M z_M & 1 & -\eta_M^{(c)} x_M & -\eta_M^{(c)} y_M & -\eta_M^{(c)} z_M \end{bmatrix}$ a 2×11 matrix, and **L** is an 11×1 matrix as shown in Eqn. (2-11) which can also be rearranged into a 3×4 matrix, known as the camera matrix **A**:

$$\mathbf{A} = \begin{bmatrix} L_1 & L_2 & L_3 & L_4 \\ L_5 & L_6 & L_7 & L_8 \\ L_9 & L_{10} & L_{11} & 1 \end{bmatrix}$$

The minimum error over a set of corresponding points in image space $\left(\xi_M^{(c)}, \eta_M^{(c)}\right)$ and object space (x_m, y_m, z_m), can be represented as:

$$\min_L \Sigma \left(\begin{bmatrix} \xi_M^{(c)} \\ \eta_M^{(c)} \end{bmatrix} - \mathbf{ML} \right)^2$$

The camera matrix, **A**, can then be calculated to retrieve all the internal and external parameters (excluding lens distortion). The internal parameters can be retrieved by:

$$\xi_H^{(c)} = \frac{L_1 L_9 + L_2 L_{10} + L_3 L_{11}}{{L_9}^2 + {L_{10}}^2 + {L_{11}}^2} \tag{2-13}$$

$$\eta_H^{(c)} = \frac{L_5 L_9 + L_6 L_{10} + L_7 L_{11}}{{L_9}^2 + {L_{10}}^2 + {L_{11}}^2} \tag{2-14}$$

$$c_x = \sqrt{\frac{{L_1}^2 + {L_2}^2 + {L_3}^2}{{L_9}^2 + {L_{10}}^2 + {L_{11}}^2} - \left(\xi_M^{(c)}\right)^2} \tag{2-15}$$

$$c_y = \sqrt{\frac{{L_5}^2 + {L_6}^2 + {L_7}^2}{{L_9}^2 + {L_{10}}^2 + {L_{11}}^2} - \left(\eta_M^{(c)}\right)^2} \tag{2-16}$$

$$c = \frac{c_x + c_y}{2} \tag{2-17}$$

The sensor's pinhole coordinates $\left(x_O^{(c)}, y_O^{(c)}, z_O^{(c)}\right)$, with respect to the world coordinates can be calculated by:

$$\begin{bmatrix} x_O^{(c)} \\ y_O^{(c)} \\ z_O^{(c)} \end{bmatrix} = -\begin{bmatrix} L_1 & L_2 & L_3 \\ L_5 & L_6 & L_7 \\ L_9 & L_{10} & L_{11} \end{bmatrix}^{-1} \begin{bmatrix} L_4 \\ L_8 \\ 1 \end{bmatrix} \tag{2-18}$$

Since the DLT method uses known coordinates (x_M, y_M, z_M), with their corresponding image coordinates $\left(\xi_M^{(c)}, \eta_M^{(c)}\right)$, to determine the camera's parameters, a minimum of six 3-D object space control points are required in order to obtain a solution. Using the DLT parameters $L_1 – L_{11}$, 3-D coordinates of image coordinates can be calculated with a

minimum of two images (i.e. two images of object space, with a minimum of six 3-D object space control points) from the following equation:

$$\begin{pmatrix} \xi_M^{(c)} - \xi_H^{(c)} \\ \eta_M^{(c)} - \eta_H^{(c)} \\ -c \end{pmatrix} = S[\mathbf{R}(\omega, \phi, \kappa)] \begin{bmatrix} x_M - x_O^{(c)} \\ y_M - y_O^{(c)} \\ z_M - z_O^{(c)} \end{bmatrix} \tag{2-19}$$

where S is the aspect ratio from Eqn. (2-9), and is normally set to 1.

Some of the major sources of error in a calibration are: inadequacy in modelling lens distortion; changes in illumination conditions between camera exposures; camera electronic noise; and uncertainty in the measurements of the 3-D coordinates of the control points [50].

2.3. Calibration process of optical SMS

2.3.1. Introduction

The calibration process used by the optical shape measurement system (SMS) has been developed to utilise a bundle adjustment model proposed by Huntley [53]. This calibration process can be split into two separate stages: (1) initialisation and (2) refinement. During the initialisation stage, the sensor parameters are initialised using a linear calibration method, such as the DLT method (described in the previous section). The refinement stage involves non-linear optimisation of the calibration model parameters in a bundle adjustment. Hence, in this section, the model for the bundle adjustment is presented, as well as the calibration model and the method of computing 3-D Cartesian coordinates from the data captured by the optical SMS are described. The objective function that must be minimised in the bundle adjustment is also discussed, and is followed up by a summary of the calibration process as a whole.

2.3.2. Model for bundle adjustment

The model for bundle adjustment developed by Huntley [53] differs from conventional bundle adjustment. In conventional bundle adjustment coordinates of points on an object surface are understood to be unknowns and are solved for as part of a large matrix inversion process. An optical SMS can have 10^6 or more unknown coordinates; even though the equivalent matrices are sparse, handling such a large number of unknowns becomes cumbersome. In order to avoid this, Huntley's method [53] involves projecting the camera and projector rays through the sensor pinholes and minimising either the minimum distances between points of closest approach of the two rays, or the distances between the points of closest approach and known control point coordinates. As a result, the minimisation is in object space and not in image space. Furthermore, the size of the matrices is fixed by the number of unknown calibration parameters, and not by the number of pixels or control points. The sensor model is based on the photogrammetric approach (as described earlier in the chapter), and is made up of 14 parameters:

- the external parameters: x_0, y_0, z_0 (pinhole coordinates), ω, ϕ, κ (Euler angles describing orientation of the image coordinate system relative to the world coordinate system),

- the internal parameters: ξ_H, η_H, and c,

- the lens distortion parameters: k_1, k_2, k_3 are the coefficients for the polynomial describing radial distortion, whilst p_1 and p_2 are the coefficients for the polynomial describing tangential distortion.

Throughout the model, three right-handed coordinate systems are used (see Figure 2-3), the sensor parameters describing the relationship between the following three coordinate systems:

- the sensor coordinate system (SCS), with the sensor pinhole position origin, $\mathbf{O}_c$,

- the image coordinate system (ICS), defined on the image plane and parallel to the SCS, having the centre of the image as the origin,

- the world coordinate system (WCS).

The calibration process involves positioning a calibration artefact in multiple orientations and locations ('poses') within the measurement volume, while measurements are taken using the required combinations of cameras and projectors. As a result, the bundle adjustment requires the estimates of the sensor parameters and also the estimates of each pose of the calibration artefact.

In each camera-projector pair, the temporal phase gradient information is obtained for the horizontal and vertical fringe patterns, τ_x and τ_y (in the range $-\pi$ to $+\pi$), which convert the shape information of the artefact in each pose. Further details on the shape data acquisition process are discussed in Chapter 6, but in simple terms a τ_x value at a given pixel defines a vertical plane, on which the scattering point must lie. The plane passes through the projector's pinhole and intersects the sensor, along a line. Likewise, a τ_y value at the same pixel defines a horizontal plane on which the scattering point must lie and a corresponding line on the projector's spatial light modulator. The intersection of the two planes defines a line, or a ray coming from the projector, that should pass through the scattering point location.

The dimensions of each phase gradient map are the same as the pixel resolution of the camera, with each valid pixel representing a 3-D point on the object surface. Hence, a camera with a resolution of 1024×1024 pixels will produce a pair of phase gradient maps (τ_x and τ_y), each map consisting of a 1024×1024 matrix. Therefore, the corresponding point cloud computed from a single projector fringe sequence can be expressed as three 1024×1024 matrices for the respective x, y, z coordinates. Estimating every pose of the calibration artefact from the set of point clouds can be achieved through identifying specific features on the artefact (e.g. sphere centres), either by manually selecting the features or by using an appropriate feature detection technique. The measured 3-D Cartesian coordinates of the identified features are then used to

calculate the initial estimate of the parameters defining the transformation from the local artefact coordinate system to the coordinate system of the SMS.

2.3.3. Computing a point cloud

In a single-camera single-projector SMS, provided the initial estimates of the sensor parameters are available, the location of the camera and projector lens pinholes can be represented by the position vectors $\mathbf{R_1}$ and $\mathbf{R_2}$, as seen in Figure 2-4. To compute a given point within a point cloud, the rays coming from the pixel coordinates (ξ_c,η_c) (camera) and (ξ_p,η_p) (projector) are projected out from the scanner into the measurement volume. The camera pixel coordinates are specified by the indices of the pixel in the 2D sensor array, whereas the projector pixel coordinates are defined by the two measured phase values at that pixel, as will be explained in more detail later in the section. These rays start at the sensor pinholes and can be represented by the vectors $\mathbf{u_1}$ and $\mathbf{u_2}$ respectively. The location of the small region on the object surface that scattered light onto the pixel of interest is assumed to be centred on a point with position vector **s**, as shown in Figure 2-4. The location of this point is calculated as the midpoint between the two points of closest approach between the vectors $\mathbf{u_1}$ and $\mathbf{u_2}$. The length of this shortest distance is labelled ε_1. Hence, by knowing $\mathbf{R_1}$, $\mathbf{R_2}$, $\mathbf{u_1}$ and $\mathbf{u_2}$, it is possible to calculate the required position vector **s**. The process of conversion from phase maps to 3-D Cartesian coordinates can be expressed as a function:

$$\mathbf{s} = \begin{pmatrix} x \\ y \\ z \end{pmatrix} = \boldsymbol{f}(\xi_c, \eta_c, \omega_x, \omega_y, C_1 \dots C_{14}, P_1 \dots P_{14}) \tag{2-20}$$

where x, y, z = world coordinates in a standard Cartesian system,,

ξ_c = image plane coordinates of the camera along *x-axis*,

η_c = image plane coordinates of the camera along *y-axis*,

ω_x = image plane coordinates of projector (phase values) along *x-axis*, lying in range $-\pi$ to π,

ω_y = image plane coordinates of projector (phase values) along *y-axis*, lying in range –π to π,

$C_1 \ldots C_{14}$ = Fourteen parameters of the camera based on the photogrammetric model of external, internal and distortion parameters,

$P_1 \ldots P_{14}$ = Fourteen parameters of the projector based on the photogrammetric model of external, internal and distortion parameters.

In order to apply Eqn. (2-20), the non-dimensional image plane coordinates (i.e. pixel indices) of the camera, $U = 1,2, \ldots, M$ and $V = 1,2, \ldots, N$ are scaled to a physical length (in the Phase Vision scanners the standard units are millimetres) from the knowledge of the physical dimensions of the charge coupled device (CCD), and by defining the origin to be located at the centre of the image plane. It should be pointed out that the origin of the camera's $M \times N$ pixel coordinate system is at the top left corner of the image, following the standard convention used in image processing. The projector image plane coordinates, ω_x and ω_y, are converted from radians to millimetres by using prior knowledge of the physical dimensions of the spatial light modulator (SLM). Therefore, both the camera and projector image plane coordinates can be calculated in the appropriate units of length by the following equations:

$$\xi_c = \left(\frac{\mathrm{U}-1}{M-1} - 0.5\right) N_{x,c}$$
$$\eta_c = \left(\frac{\mathrm{V}-1}{N-1} - 0.5\right) N_{y,c} \quad (2\text{-}21)$$

$$\xi_p = \left(\frac{\boldsymbol{\omega_x}}{2\pi}\right) N_{x,p}$$
$$\eta_p = \left(\frac{\boldsymbol{\omega_y}}{2\pi}\right) N_{y,p} \quad (2\text{-}22)$$

where $N_{x,c}$, $N_{y,c}$ = length of camera CCD – physical dimensions along ξ_c and η_c axes, respectively,

$N_{x,p}$, $N_{y,p}$= length of projector SLM – physical dimensions along ξ_p and η_p axes, respectively.

2.3.4. Description of the 'pose' of an artefact

During the calibration of a multi-sensor SMS, measurement scans of the calibration artefact being used can be obtained by different camera-projector pairings, hence, the respective computed point clouds will give different 3-D views of the artefact. When individual artefact features are identified or detected in their respective point clouds, the scattering points (alongside their corresponding pixel coordinates in the phase maps) belonging to each feature need to be labelled consistently across all the point clouds of all poses of the artefact. With this method, each feature parameter (e.g. the coordinates of a sphere centre) is uniquely linked across all poses, and across the different camera-projector pairings.

The estimate of each pose is the transformation that is applied to go from a local coordinate system in which the key features of the artefact are defined (acquired for example by a mechanical CMM), to the world coordinate system (WCS) that characterises the measurement volume of the SMS. This is described in terms of position and orientation by six parameters, t_x, t_y, t_z (constituents of a translation vector along the *x, y, z* axes), and the Euler angles, ω, ϕ, κ (rotations about the *x, y, z* axes). The transformation is expressed as:

$$\mathbf{W_s} = \mathbf{R_s W_c} + \mathbf{T_s} \tag{2-23}$$

where $\mathbf{W_s}$ = Cartesian coordinates of an artefact feature in the world coordinate system,

$\mathbf{R_s}$ = rotation matrix computed from the Euler angles,

$$= \begin{bmatrix} \cos\phi\cos\kappa & \cos\omega\sin\kappa + \sin\omega\sin\phi\cos\kappa & \sin\omega\sin\kappa - \cos\omega\sin\phi\cos\kappa \\ -\cos\phi\sin\kappa & \cos\omega\cos\kappa - \sin\omega\sin\phi\sin\kappa & \sin\omega\cos\kappa + \cos\omega\sin\phi\sin\kappa \\ \sin\phi & -\sin\omega\cos\phi & \cos\omega\cos\phi \end{bmatrix}$$

$\mathbf{W_c}$ = coordinates of the feature in the local coordinate system,

$\mathbf{T_s} = \begin{bmatrix} t_x \\ t_y \\ t_z \end{bmatrix}$ = translation vector.

During the bundle adjustment process, the 6 parameters defining $\mathbf{R_s}$ and $\mathbf{T_s}$ are refined and applied to $\mathbf{W_c}$ in Eqn. (2-23) to compute $\mathbf{W_s}$. The number of parameters that should be refined can be reduced for certain artefacts with special symmetries. For example, for an artefact consisting only of a single sphere just the three displacement parameters should be allowed to vary during the bundle adjustment as the surface of the sphere is invariant under rotation about any of the three axes. Likewise, an artefact with cylindrical symmetry about the *z*-axis has five degrees of freedom, with κ fixed during the adjustment.

2.3.5. Bundle adjustment in object space

Bundle adjustment is the problem of refining a visual reconstruction to produce jointly optimal 3D structure (real world coordinates) and viewing parameter (external and/or internal) estimates [54]. The bundle adjustment process for the optical SMS involves the minimisation in object space of two quantities in a non-linear least squares sense: the minimum distances between distances of closest approach of the rays from camera and projector, α_1, and the distances between the points of closest approach and known control point coordinates, α_2. This is expressed as an objective function, *F*, with two terms:

$$F = \gamma_1 \sum_i {\alpha_{1,i}}^2 + \gamma_2 \sum_i {\alpha_{2,i}}^2 \qquad (2\text{-}24)$$

The summation applies over all the pixels (or some representative sub-set of the pixels) for the camera-projector pair containing shape data, where γ_1 and γ_2 are scalars that allow for different weighting of terms, though typically they are both set to unity [53]. The first term on the right hand side is the sum of the squares of α_1 errors between the rays projected from camera and projector pinholes. The second term is the sum of the squares of α_2 errors between the known and calculated control point coordinates. The calculation of α_2 therefore depends on the type of geometric features present on the calibration artefact, and further details of how it is calculated for the calibration artefact used will be shown in Chapter 6. Subscript i on the α_1 and α_2 variables is used to denote the value of these quantities for the *i*th pixel.

The minimisation process involves differentiating F with respect to the model parameters:

$$\frac{\mathrm{d}F}{\mathrm{d}t} = 2\gamma_1 \sum_i \alpha_{1,i} \frac{\mathrm{d}\alpha_{1,i}}{\mathrm{d}t} + 2\gamma_2 \sum_i \alpha_{2,i} \frac{\mathrm{d}\alpha_{2,i}}{\mathrm{d}t} \tag{2-25}$$

where t = a generic parameter referring to the parameters which are free to change.

The number of parameters, N_p, can be calculated by:

$$N_p = N_{fs} + N_{fa} \tag{2-26}$$

where N_{fs} = number of free sensor parameters (both camera and projector),
N_{fa} = number of artefact poses × number of free artefact parameters.

The bundle adjustment refines both the camera and projector parameters alongside the estimate of orientation parameters for each pose of the calibration artefact. Therefore, the calibration artefact is free to undertake arbitrary rigid body translation and rotation

during bundle adjustment. A full explanation of the bundle adjustment process including why the above objective function is used can be found in [53].

2.3.6. Optimisation of parameters

Eqn. (2-24) is nonlinear and hence cannot be solved directly [53]. Instead, an iterative scheme is used which involves solving for the vector **d** in the equation:

$$\mathbf{Hd} = -\mathbf{g} \tag{2-27}$$

where **g** is a column vector of the derivatives of F with respect to each of the N_p parameters, and **H** is the Hessian matrix (i.e. the matrix of second derivatives such that $H_{ij} = \partial^2 F / \partial x_i \partial x_j$).

The estimate of the solution vector **x** (an $N_p \times 1$ vector containing the current estimate of all the required parameters) is then updated as follows at the kth step:

$$\mathbf{x_{k+1}} = \mathbf{x_k} + \mathbf{d_k} \tag{2-28}$$

where from Eqn. (2-27), $\mathbf{d}_\mathrm{k} = -\mathbf{H_k^{-1}}\mathbf{g_k}$. Evaluation of the Hessian matrix would be cumbersome, so instead, the Gauss-Newton method is used, in which an approximation to the Hessian matrix is given by $\mathbf{J_k^T J_k}$, where **J** is the Jacobian:

$$\mathbf{H} \approx 2\begin{pmatrix} \sum_i \left(\frac{\partial \varepsilon_i}{\partial x_1}\right)^2 & \sum_i \left(\frac{\partial \varepsilon_i}{\partial x_1}\right)\left(\frac{\partial \varepsilon_i}{\partial x_2}\right) & \cdot & \cdot \\ \sum_i \left(\frac{\partial \varepsilon_i}{\partial x_2}\right)\left(\frac{\partial \varepsilon_i}{\partial x_1}\right) & \sum_i \left(\frac{\partial \varepsilon_i}{\partial x_2}\right)^2 & \cdot & \cdot \\ \cdot & \cdot & \cdot & \cdot \\ \cdot & \cdot & \cdot & \sum_i \left(\frac{\partial \varepsilon_i}{\partial x_1}\right)^2 \end{pmatrix} \tag{2-29}$$

Eqns. (2-27) and (2-28) are iterated from an initial estimate for **x** until convergence is achieved. However, the Gauss-Newton experiences difficulties if $\mathbf{H_k}$ is close to singular, which subsequently affects the performance and rate of convergence [55]. Eqn. (2-27) is adapted to the Levenberg-Marquardt method as a result, with the implementation using Fletcher's strategy [55] for modifying the scalar, μ_k in

$$-\mathbf{g_k} = (\mathbf{H_k} + \mu_k \mathbf{I})\mathbf{d_k} \tag{2-30}$$

where $\mu_k \geq 0$ and **I** is an identity matrix with the same matrix size as $\mathbf{H_k}$.

In order to improve the robustness of the optimisation still further, Eqn. (2-28) is also revised by introducing a scalar, α, thus:

$$\mathbf{x_{k+1}} = \mathbf{x_k} + \alpha\mathbf{d_k} \tag{2-31}$$

α is generally set to 1 at the start of the bundle adjustment. However, if at the k^{th} iteration, the current value of α increases *F*, then a new value for α that minimises *F* is computed. The updated α is then used for subsequent iterations in Eqn. (2-31). In this way, the cost function is guaranteed to be continually reduced thus preventing divergence of the algorithm.

2.3.7. Calibration Process

The two separate stages of the calibration process mentioned earlier, i.e. (1) initialisation and (2) refinement can be further broken down into four sub-processes:

1. shape data acquisition,
2. sensor parameter initialisation,
3. shape data post-processing,
4. bundle adjustment.

Shape data acquisition covers the first half of the initialisation stage, and refers to the capture of shape information of the calibration artefact during measurement. When a measurement is performed, a sequence of fringe patterns is projected from the projector(s), whilst the camera(s) captures images of the patterns projected. The shape information for each camera-projector pairing is contained in a pair of unwrapped phase maps, ω_x and ω_y respectively, the first resulting from the projection of vertical fringes the other from the projection of horizontal fringes. The unwrapped phase maps are then converted to a point cloud, with detected artefact features from the point cloud being used to estimate the initial artefact poses. During the second half of the initialisation stage, measurements are taken by all camera-projector pairings of a set number of poses of an artefact. The necessary features on the artefact are then detected from the acquired measurements in image space, and used by the DLT method to calculate initial estimates of all the camera and projector parameters (for all relevant camera-projector pairings).

The refinement stage of the calibration process covers shape data post-processing and bundle adjustment. Shape data post-processing selects from the artefact features previously detected, the required number of control points and saves this information. The control point information, artefact pose and the sensor parameters are then used as initial estimates in a bundle adjustment. The bundle adjustment refines all the sensor parameters and artefact poses, and in the process, minimises the objective function describing the calibration model.

2.4. Calibration artefacts

In this section, discussion will focus on the calibration artefacts used in calibration methods similar to those already discussed earlier in this chapter. Examples of artefacts used in calibration methods for non-contact measurement techniques include regular shapes such as circles, rectangles, cylinders, cubes and spheres; such shapes suggest that both 2-D and 3-D artefacts are used. 2-D artefacts are disadvantageous to a certain extent as a complete set of sensor parameters can’t be recovered without prior knowledge of the setup, normally, the internal geometry such as sensor size and the principal distance. Meanwhile, 3-D calibration artefacts enable a more accurate

calibration, as they provide greater information of the environment within the measurement volume. This extra information then supports the strong recovery of sensor parameters.

A popular form of artefact is a planar surface or multiple planar surfaces of a particular colour, speckle pattern, or a combination of both. For example, a calibration artefact consisting of two perpendicular planes with 256 circles on each plane was used by Heikkila [50]. A planar checkerboard was used by Zhang and Huang to calibrate a structured light system [56], camera calibration was done using a planar black and white coloured checkerboard, whilst a planar red and blue coloured checkerboard was used for projector calibration. A planar checkerboard artefact was also used by Ke et al. [57] to calibrate a structured light system.

Liu et al. [58] used a 3-D object as a calibration artefact; the artefact consisted of a three-step plane with circular targets. Planar surfaces can also be combined to produce calibration artefacts, for example, two nominally parallel planes can be created by separating two plates, by a known fixed distance, provided the plates are manufactured to a high tolerance in terms of flatness and parallelism. This then provides a length scale as the perpendicular distance between the two plates is known, a useful property for detecting and identifying the orientation of the artefact during the calibration process.

Sun et al. [59] used targets produced by two 19” LCD (liquid crystal display) monitors side-by-side, as-well-as, a length bar with a target at each end separated by a known fixed distance, to calibrate a stereo vision system with a large field-of-view. The monitors displayed an image of ten co-linear feature points with an interval of 38.67 mm, whilst the length bar had two target features separated by 1218.64 mm. A non-overlapping multiple vision system was calibrated by Liu et al. [60] using targets displayed on a monitor and a planar calibration grid combined. The monitor display had 31 feature points evenly spaced along the target with an interval of 10.56 mm, whilst the planar calibration grid had a 10 × 10 matrix of feature points with an interval of 9 mm. The rotation matrix between two neighbouring vision sensors was computed using the co-linearity property of the targets. Then the translation vector was computed according

to the known distances between the feature points on the targets. The global calibration of all the vision sensors was realised by repeating this process on all combinations of neighbouring vision sensors.

Baker and Aloimonos [61] calibrated a multi-camera network into a global coordinate frame, where it was not necessary for all the cameras to have a common field of view. By switching off the room lights and waving a wand with an LED at the end of it, very large sets of point correspondences were captured. These point correspondences were then used in a large, nonlinear eigenvalue minimisation whose basis was epipolar constraint. The eigenvalue matrix encapsulates all point correspondences between every pair of cameras in a way that minimising the smallest eigenvalue results in the projection matrices, to within a single perspective transformation. In a second step, given additional data from waving a rod with two LEDs (one at each end) the full projection matrices are calculated. The method was extremely accurate – the reprojections of the reconstructed points were within one pixel.

Klaas et al. [62] used a combination of a standard industrial robot, a photogrammetric system and a 3-D white light scanner for precise automated digitalisation of large objects. It was clear that the simple approach of using just a scanner mounted on a robot would not be sufficiently accurate, hence, a new approach was selected to compensate the limited absolute 3-D accuracy of the robot with an additional large volume optical tracking system. This optical tracking system consisted of a standard white light scanner fitted with a dimensionally stable structure holding LEDs, which was tracked by the photogrammetric tracking system. With LED measurements the tracking system was able to calculate the white light scanners position and orientation in its local coordinate system. These positions were then used to correct the less accurate positions read from the robot control unit. The coordinate systems of the white light scanner and the optical tracking system were then aligned into one global coordinate system.

Chen and Liao [63] used an artefact built from two objects for calibrating a fringe projection system. One of the objects, a calibration block, was manufactured from laser lithography with accurately referenced patterns. The second object was a silicon

substrate with a chemical vapour deposition synthesised surface coating applied to it. The artefact was translated along the third axis at discrete intervals to form a non-planar measurement space. A similar mechanism was used by Sitnik et al. [64] to calibrate a fringe projection system, except that the artefact consisted of a matrix of circles. Different forms of this type of artefact have now also been adopted by commercial manufacturers of fringe projection systems for calibration. Hu et al. [65] manufactured an aluminium plate with holes and spray painted it white to calibrate a fringe projection system. Mapping the 3-D position of the holes was determined through prior measurement on a mechanical CMM.

The use of cubes as calibration objects has been demonstrated in some systems; Godhwani et al. [66] used a cube combined with a set of rings for calibrating cameras in a multiple-sensor structured light system. A cube of 150 mm with 72 circular fiducial marks on three of the faces was used for calibrating a structured light sensor by Valkenburg and McIvor [67]. The location of each fiducial mark was independently determined to an uncertainty of 0.1 mm; nevertheless, it was proposed that the system calibration could be improved by increasing the density of the fiducial marks and improving their distribution across the artefact. The major drawback of using cubes as artefacts for multiple sensor systems is that a cube, in a certain orientation, would provide multiple different views when seen from the position of the sensors, e.g. two individual sensors placed apart would see the artefact differently; hence, the shape data captured would differ. A planar artefact also suffers from this same drawback.

A precision sphere, such as a ball bearing, was used by Penna [68] for calibrating the scale factor of a camera, using the relationship between the scale factor and the distortion in an image of a circle. The use of spheres as calibration objects has been expanded by others; multiple images of three spheres was used by Xu et al. [69] to calibrate the internal and external parameters of a camera, this was further expanded by Zhang et al. [70], [71], Agrawal and Davies, for calibrating the sensor parameters of multiple cameras. A sphere has the unique property that from whichever location it is viewed from, it reveals a curved surface that can be used for determining the position of its centre. This feature was fully utilised by Ogundana [19], in which the calibration of a

multiple-sensor fringe projection system was demonstrated comprehensively, using a motorised carbon fibre length bar supporting two spheres, separated by a known fixed distance. This approach was then for some time also used by Phase Vision Ltd for calibrating all of their commercially available fringe projection shape measurement systems.

Evidence of the large variety of artefacts used for calibration of optical 3-D measurement systems suggests that standardised reference artefacts and procedures for calibration (and verification) currently do not exist [72], hence, traceability of these measurement systems is still an open issue. Manufacturers of such systems try to overcome this by developing in-house forms of system calibration, that do provide an element of traceability e.g. through compliance with tactile measurements that do have traceability. Although in 2002, a German guideline VDI/VDE 2634 was introduced for verification of optical 3-D scanning system performances. In order to verify the accuracy of a measurement volume(s), a verification artefact needs to be measured in several positions, a minimum of three but it is recommended to use five to seven [72], [73].

2.5. Summary

Calibration of the projector and imaging sensor are crucial factors that affect the overall measurement accuracy of an optical SMS. Models describing quantitatively the sensor imaging geometry have been introduced. Some of the calibration techniques which have been developed within the photogrammetry and computer vision fields have been highlighted, as well as their adaptation to the calibration of an optical SMS based on the projected fringe method.

The calibration process based on a bundle adjustment model has been presented. The model is characterised by both sensor and artefact pose parameters; these are optimised by the bundle adjustment through the utilisation of a reference artefact with well-defined geometric features used as control points and which is characterised on an independent measurement instrument, such as a mechanical CMM. The sensor parameters provide a conversion from the sensor coordinate system to the world

coordinate system, whilst the pose parameters provide the rigid body transformation for the control point coordinates from a local coordinate system to the world coordinate system.

A by-product of using multiple poses of the artefact for calibration, results in the operator of the optical SMS having to process and manage a large quantity of data. Care must be taken to ensure that all geometric features and scattering points are labelled consistently across all the point clouds of all the poses being used by the calibration process.

2.6. Figures

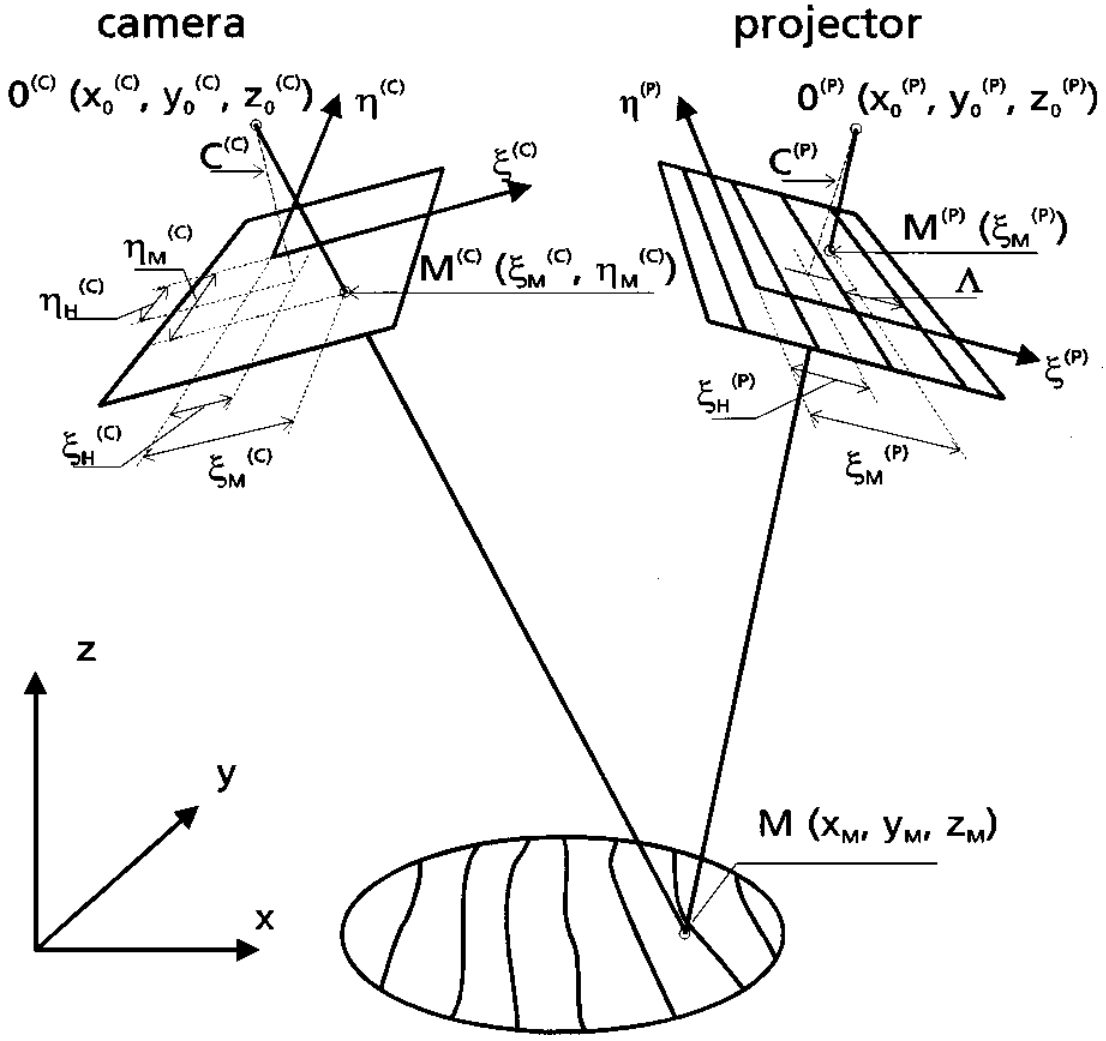

Figure 2-1: Relationship between measurement values and 3-D coordinates in a fringe projection system [20].

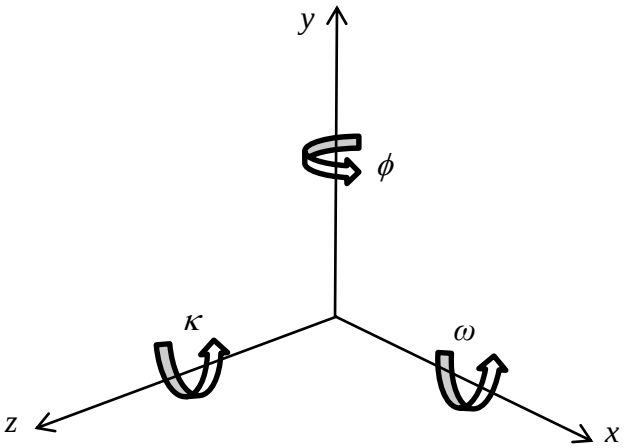

Figure 2-2: *x, y, z* axes along with their corresponding Euler angles, ω, ϕ, κ.

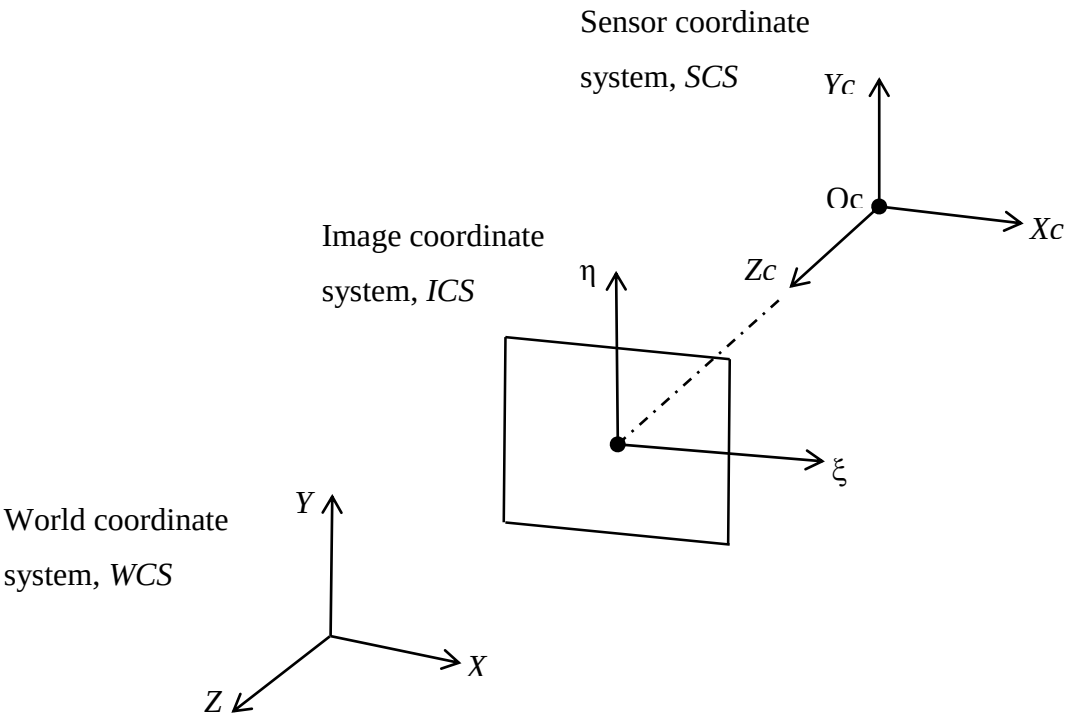

Figure 2-3: Coordinate systems in the optical SMS, where Oc is the pinhole of the sensors

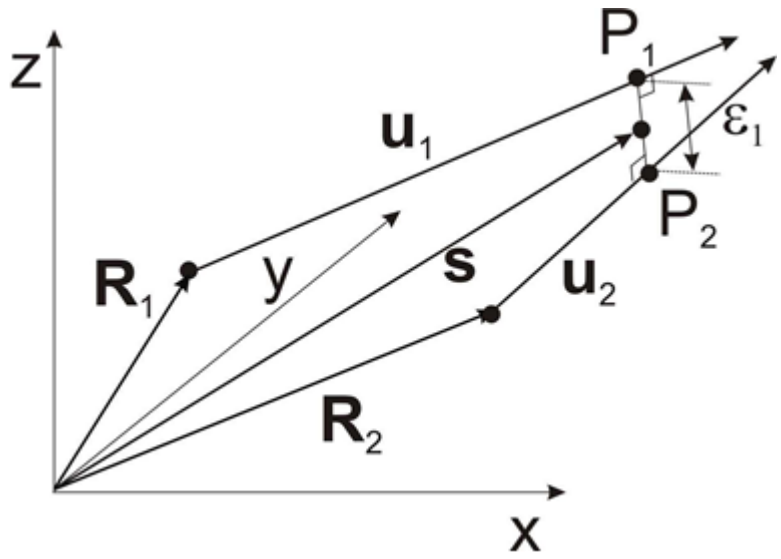

Figure 2-4: Bundle adjustment model in object space – vector diagram [53].

Chapter 3

Large volume calibration artefact

3.1. Introduction

In previous work a ball-bar calibration artefact was used by Ogundana [19] in implementing the calibration process for the Phase Vision Ltd optical 3-D SMS. The approach involved placing the artefact in multiple locations, and introducing the known sphere-sphere separation as a constraint during the bundle adjustment on each pose. The main drawback in using a ball-bar artefact for large volumes is the small coverage it provides of the measurement volume in any given point cloud. A single measurement of the artefact is insufficient to provide a reliable calibration of the sensors [56], [74], hence, provisions have to be made for positioning the artefact at different locations within the measurement volume. A ball bar becomes inappropriate when a second, adjacent, non-overlapping measurement volume is introduced as there is only one part of the artefact defining a length scale (the sphere-sphere separation) which cannot simultaneously be present in both the measurement volumes.

Planar artefacts have been developed by Phase Vision and other manufacturers, where several lengthscales are present simultaneously (usually these are an array of circles of squares with centres or corners at known positions) but as the deflections due to gravitational forces scale rapidly with the dimension of such artefacts, they are inapplicable for the larger measurement volumes of interest here. In this chapter, an alternative calibration artefact is presented, which aims to overcome these major drawbacks. Both the theoretical background and the practical issues associated with such an artefact are discussed.

3.2. Artefact design considerations

3.2.1. Geometric considerations

Important considerations when designing a calibration artefact are its size and shape: a major source of error in calibration often comes from the level of accuracy to which the

dimensions of an artefact geometry are known [50], [74]–[76]. Hence, an appropriate design should address the balance between a geometry that on the one hand allows a 3-D optical SMS to make a valid measurement, whilst also being representative of real world objects, and on the other hand can also be measured by traditional measuring instruments to high accuracy, e.g. on a CMM [77].

A calibration artefact will also typically require positioning at different locations across the measurement volumes, hence, the features present need to be visually and geometrically apparent so that they may be utilised as control points during the calibration [76]. The choice of feature is dependent on several factors, including the size of the calibration artefact, the focal length of the camera lens(es), pixel size, stand-off distance between the SMS and the calibration artefact, the illumination conditions and the type of surface finish required.

The motion of the artefact can also introduce errors in the relative locations of the features. Acceleration of the artefact causes transient inertial forces and hence distortion of the structure. Likewise, ground- and air-borne vibration cause dynamic deflections that may potentially be significant, dependent on the resonant frequencies and level of damping of the structure. Probably the largest source of error in larger artefacts, however, is the displacement field accompanying a change in gravitational load distribution caused by rotation about a horizontal axis. Such errors therefore need to be considered in the geometrical design of an artefact.

3.2.2. Material considerations

A calibration artefact will be used in a variety of environmental conditions, therefore, it is essential that both the thermal and moisture (also referred to as hygral) expansion coefficients of the materials used are sufficiently low. ‘Sufficient’ in this context means that the dimensional changes of the artefact due to the maximum expected temperature and humidity change over the timescale between successive calibrations should be a small fraction (typically 1/10 or less) of the relative accuracy required of the optical measurement system. Low thermal conductivity together with high stiffness is also highly desirable. Keeping the overall weight as low as possible would allow for easier

handling by the operator, and reduce the gravitational deflections. Highly reflective or transparent surface finishes are inappropriate for use with an optical SMS. Whilst coatings and/or developer powder may be used to make such surfaces more easily measurable, care must be taken when doing this to prevent small changes in the dimensions of the artefact.

3.3. Ball-bar calibration artefacts

As stated in Section 3.1, ball-bar artefacts have been used previously to calibrate optical SMSs [19], [78]. A ball-bar simply consists of two spheres whose centres are separated by a known, fixed distance. Ogundana [19] demonstrated that a ball-bar calibration artefact, measured in many different poses, can be used to calibrate an optical SMS. A modified ball-bar was used in the work of Nguyen [78], where the two spheres, made from tungsten carbide, were separated by a known, fixed distance, using carbon fibre tubing, with the two spheres attached to the two ends of the tube (see Figure 3-1). The length scale for this artefact was set by the separation distance between the two sphere centres.

Spheres are attractive as artefact features, as they have the unique property that from whichever position they are viewed, unless obstructed, they reveal a uniformly curved surface with no discontinuity or edge. From these curved surfaces, it is then possible to identify and calculate the sphere centres, and hence the distances between sphere centres for calibration. One drawback of spheres is that the spatially-varying surface normal can results in strong variations in recorded intensity, which gives rise to low signal to noise ratio in the darker regions of the images and systematic errors in the regions of high intensity gradient. Such problems can be largely avoided if the spheres are prepared with a diffusely scattering surface finish.

3.4. Large volume calibration artefact

To achieve the objective of making the calibration process useable across multiple measurement volumes, it becomes necessary to design and manufacture a calibration artefact that addresses the defects in those used previously. The challenges presented by a larger overall measurement volume, formed by the combination of two adjacent SMSs,

require a calibration artefact that can place more reference features, at accurately known locations, and spread evenly across the two measurement volumes. In this way, each independent SMS has several reference features within its measurement volume. This would not completely eliminate the need for movement of the artefact around the measurement volume, but would reduce the required number of poses significantly compared to that for the ball-bar artefact, and provide greater coverage of the measurement volume in any single measurement scan.

The need for fewer poses arises from the fact that in a ball bar there are in effect only 6 measured quantities per pose (the Cartesian coordinates of the two sphere centres) whereas five unknowns are introduced per pose (the three translation parameters plus two Euler eangles). Simply doubling the number of spheres in the artefact, for example by arranging four spheres at the vertices of a tetrahedron, increases the surplus of knowns over unknowns from 1 to 7 ($= 4 \times 3 - 5$). Traceability for calibration would be provided through measurement characterisation of the artefact on a certified mechanical CMM (a higher level measurement standard). Hence, accurate positioning of the artefact in the measurement volume would not be necessary, since the length scale would be introduced by the known feature locations. The main requirement on the positioning system is that the artefact should remain in the same position for the duration of any one scan in the calibration process.

In this work, a new large volume calibration artefact is introduced, which utilises and expands on the ball-bar concepts highlighted in the previous section. The carbon fibre tube ball-bar is expanded to include more reference spheres in a networked geometry structure. The basic concept is to assemble the artefact from a basic building block consisting of a triangular element with three spheres and three connecting rods, on account of the structural rigidity of such a triangle. This contrasts with a square (4 spheres and 4 rods), for example, which has no rigidity in shear. Two vertical triangles parallel to one another but rotated through 180 degrees about their normals can be joined by 6 further rods that in turn create 6 further triangular faces. Figure 3-2 shows a CAD model representation of an extension of this example in which 5 vertical triangles are joined together by sets of 6 connecting rods. From the CAD model it is clear that

one potential issue is the large fraction of a given sphere's surface that may be covered by the rod ends, and which risks interference with the scanner's measurement of the sphere's surface. The end cap design was therefore considered in some detail, as will be discussed in Section 3.5.1.

In the design of this networked geometry, the main practical issues considered (which will be discussed further in this chapter) include: the total number of spheres required in the network; the size of these spheres; the arrangement and separation distance between the spheres; and the cross-sectional size, wall thickness and length of the carbon fibre tubing. Furthermore, care needs to be taken with the method for attaching the spheres to the tubing so that the artefact can be assembled and disassembled conveniently and quickly whilst maintaining sufficiently reproduceable sphere-sphere separations on successive artefact reassembly operations. On top of these practical issues, the artefact design considerations detailed in section 3.2. must also be taken into consideration.

The networked geometry or 'large volume' calibration artefact maintains the benefits of the ball-bar artefact in that it provides traceabitity for calibration, has the potential to be scalable in size, easily reconfigurable and deployable for use during the calibration process. However, by following this approach, several further issues arise, such as the deformation of the overall structure due to gravity and the dimensional changes this induces, as well as dimensional changes due to changes in temperature and humidity. The quality of the machining processes used for manufacturing the artefact also has an effect on its performance and needs to be controlled carefully.

The remainder of this chapter describes how all of these major practical issues were overcome. The structural analysis and materials testing that was done, in order to validate the integrity of the design, so that it could be used with a high level of confidence for calibration, are presented. The different components used in constructing the artefact, along with the subsequent thermal, hygral and CMM measurements carried out for its characterisation, and to provide traceability when calibrating the optical SMSs, are described.

3.4.1. Model for structural analysis

In defining the overall networked geometry for the large volume calibration artefact, there are many variables that are user defined: the total number of spheres required in the network; the size of these spheres; the arrangement and separation distance between sphere centres; and the cross-sectional size and wall thickness of the carbon fibre tubing that connects the spheres together to form the networked geometry structure. When defining these variables, care must be taken to ensure that the geometry of the structure is minimally rigid, in order for it to remain stable throughout the measurement process. This means that the number of carbon fibre tubes used for connecting the spheres must be no more nor less than is necessary to provide a rigid structure for the defined number of spheres. If there were too few connecting tubes between the spheres, then the structure would not be rigid, and the spheres would be free to move with respect to one another. If on the other hand there were too many connecting tubes then this would cause the structure to become over determined [79], [80].

The Maxwell-Laman theory [81]–[85] states that a 3-D structure (or graph as it is known in the theory) is minimally rigid if it satisfies two rules:

1. $E = 3N - 6$ (3-1)
2. every non-empty sub-structure (or graph) contains $3N - 6$ edges.

where E is the number of connecting tubes (or edges in a graph), and N is the number of spheres in the structure (or nodes in a graph).

In practice, a structure normally satisfies the Maxwell-Laman theory if it has enough connecting tubes to be minimally rigid and does not have any obvious over-determined sub-structures. Therefore, the structure of the networked geometry used for the calibration artefact must satisfy the Maxwell-Laman theory.

The number ‘6’ in Eqn. (3-1) is significant as it relates to the number of rigid body constraints that must be present in a structure for it to be minimally rigid. A commonly

used method for providing these six rigid body constraints is the '3-2-1' support approach. As the name implies, there are three supports in total for a structure, one support provides three constraints, a second support provides two, and a third support provides one.

The first support provides three rigid body constraints in x, y and z; with this support the structure is still free to rotate about this point. A second support then provides two rigid body constraints in the directions normal to a line joining the first and second supports. The structure at this point is now only free to rotate about an axis defined by a line joining the first and second supports. Hence, to stop this from occuring, a third support in the direction normal to the plane defined by the three supports, then provides the remaining rigid body constraint. The three supports used should be as evenly spread as possible across the structure, whilst providing all six rigid body constraints [79], [80].

In order to understand the effects of the gravitational forces present, and the deformation caused due to these forces once a structure satisfies the Maxwell-Laman theory, it becomes necessary to carryout a structural analysis. The method used in this work for performing the structural analysis is the stiffness matrix method, in which matrices containing material properties are set up to solve finite element method (FEM) problems. This is one of the most common methods of FEM, and is particularly suited to automated analysis of complex structures [86].

To define a closely representative structure for analysis in the FEM model, the large volume calibration artefact is modelled as a space truss. A space truss in this case is defined as a 3-D structure of straight members, with concurrent centre lines, connected at their ends by ball-and-socket joints. A space truss is subjected to forces that act only at the joints (also referred to as nodes) and where the members develop only axial forces [79], [80]. The ball-and-socket joints in this instance represent the spheres of the artefact, whilst the members would represent the carbon fibre tubes connecting the spheres in the networked structure. A ball-and-socket joint is an appropriate model here because, as will be seen, the rods are attached to the spheres with magnets that allow rotation of the rod axes about the sphere centre. The following mathematical model

describing the stiffness matrix method for analysing a space truss is based primarily on that presented by Kassimali [80], which follows the classical approach to matrix analysis of structures.

For a space truss, the forces and displacements at the joints are described with reference to a global Cartesian right-handed 3-D coordinate system, with three global coordinates (*X, Y, Z*) used to specify the locations of all the joints of the space truss. Since an unsupported (or 'free') joint of a space truss can translate in any direction in 3-D space, three displacements (in *X, Y, Z*) are needed to completely establish its deformed position. Therefore, every joint of a space truss has three degrees-of-freedom (DOF), and three structure coordinates have to be defined at each joint. Furthermore, the Maxwell-Laman theory has already highlighted that a 3-D structure requires six rigid body (or 'fixed') constraints for a structure to be minimally rigid. Therefore supports are required in order to maintain these constraints so that a static analysis is possible.

A local right-handed coordinate system (*x,y,z*) is established for each member of the space truss. The origin of the local coordinate system is located at one of the member ends, with the *x-axis* directed along the member's centroidal axis in its undeformed state (see Figure 3-3). When a space truss is subjected to external forces, each member, *m*, of the structure deforms, and axial forces are induced at the ends of each member (see Figure 3-4). As already mentioned above, three displacements – translations in the local coordinate system, are needed to fully locate the displaced position of each end of every member under load. Hence, each member has a total of six DOF, however, small displacements in the directions perpendicular to every members centroidal axis do not cause any forces in the member [80]. As a result, each member is considered to have two DOF, u_1 and u_2, in the local coordinate system, and two corresponding member end forces, Q_1 and Q_2. The local end displacement vector, **u**, for a member of a space truss is expressed as:

$$\mathbf{u} = \begin{bmatrix} u_1 \\ u_2 \end{bmatrix} \tag{3-2}$$

where u_1 and u_2 represent the displacements at each end of the current member, in the direction of the member's *x-axis* in the local coordinate system.

The relationship between the member end force vector, **Q**, and the end displacement vector, **u**, in the local coordinate system, is expressed as:

$$\mathbf{Q} = \mathbf{ku} \tag{3-3}$$

where **k** represents a two-by-two member stiffness matrix in the local coordinate system.

The local stiffness matrix for the members of space trusses is expressed as:

$$\mathbf{k} = \frac{EA}{L}\begin{bmatrix} 1 & -1 \\ -1 & 1 \end{bmatrix} \tag{3-4}$$

where E = the elastic modulus of the member material,
A = the cross sectional area of the member,
L = the original member length prior to deformation.

At this point, a transformation of the local member displacement and force vectors along with the local stiffness matrix must be done to bring them into the global coordinate system of the space truss. From Figure 3-5, the coordinates of node '1' of the member in the global coordinate system are (X_1, Y_1, Z_1) and the coordinates of node '2' of the member are (X_2, Y_2, Z_2). Also shown are the angles (θ_X, θ_Y, θ_Z) measured from the global coordinate axes to the local *x-axis* (as this is the local axis in which both member displacements and forces act along). Hence, the length, L, and the direction cosines ($\cos\theta_X$, $\cos\theta_Y$, $\cos\theta_Z$) of the member can be expressed in terms of the global coordinates of its ends by the following relationships:

$$L = \sqrt{(X_2 - X_1)^2 + (Y_2 - Y_1)^2 + (Z_2 - Z_1)^2} \tag{3-5}$$

$$\cos\theta_X = \frac{X_2 - X_1}{L} \tag{3-6}$$

$$\cos\theta_Y = \frac{Y_2 - Y_1}{L} \tag{3-7}$$

$$\cos\theta_Z = \frac{Z_2 - Z_1}{L} \tag{3-8}$$

Also shown in Figure 3-5 are the corresponding member end displacements, **v**, and end forces, **F**, in the global coordinate system. Thus, the transformation of member end forces and end displacements from a global to a local coordinate system is expressed as:

$$\begin{bmatrix} Q_1 \\ Q_2 \end{bmatrix} = \begin{bmatrix} \cos\theta_X & \cos\theta_Y & \cos\theta_Z & 0 & 0 & 0 \\ 0 & 0 & 0 & \cos\theta_X & \cos\theta_Y & \cos\theta_Z \end{bmatrix} \begin{bmatrix} F_1 \\ F_2 \\ F_3 \\ F_4 \\ F_5 \\ F_6 \end{bmatrix} \tag{3-9}$$

This equation can be symbolically expressed as **Q** = **TF**, where **T** is a 2 × 6 transformation matrix given by:

$$\mathbf{T} = \begin{bmatrix} \cos\theta_X & \cos\theta_Y & \cos\theta_Z & 0 & 0 & 0 \\ 0 & 0 & 0 & \cos\theta_X & \cos\theta_Y & \cos\theta_Z \end{bmatrix} \tag{3-10}$$

Since member end displacements, like end forces, are vectors defined in the same directions as the corresponding forces, the transformation matrix, **T**, can also be used to transform member end displacements from the global to the local coordinate system, and is expressed as **u** = **Tv**.

The transformation of member end forces from the local to the global coordinate system can be expressed in matrix form as:

$$\begin{bmatrix} F_1 \\ F_2 \\ F_3 \\ F_4 \\ F_5 \\ F_6 \end{bmatrix} = \begin{bmatrix} \cos\theta_X & 0 \\ \cos\theta_Y & 0 \\ \cos\theta_Z & 0 \\ 0 & \cos\theta_X \\ 0 & \cos\theta_Y \\ 0 & \cos\theta_Z \end{bmatrix} \begin{bmatrix} Q_1 \\ Q_2 \end{bmatrix} \tag{3-11}$$

This equation can be symbolically expressed as:

$$\mathbf{F} = \mathbf{T^{-1}Q} \tag{3-12}$$

The relationship between the global end forces, **F**, and the global end displacements, **v**, for the members of space trusses is expressed as:

$$\mathbf{F} = \mathbf{Kv} \tag{3-13}$$

The member global stiffness matrix, **K**, is given by the following equation:

$$\mathbf{K} = \mathbf{T}^T\mathbf{kT} \tag{3-14}$$

This in terms of the direction cosines of the member can be written as:

$$\mathbf{K} = \frac{EA}{L} \begin{bmatrix} \cos^2\theta_X & \cos\theta_X\cos\theta_Y & \cos\theta_X\cos\theta_Z & -\cos^2\theta_X & -\cos\theta_X\cos\theta_Y & -\cos\theta_X\cos\theta_Z \\ \cos\theta_X\cos\theta_Y & \cos^2\theta_Y & \cos\theta_Y\cos\theta_Z & -\cos\theta_X\cos\theta_Y & -\cos^2\theta_Y & -\cos\theta_Y\cos\theta_Z \\ \cos\theta_X\cos\theta_Z & \cos\theta_Y\cos\theta_Z & \cos^2\theta_Z & -\cos\theta_X\cos\theta_Z & -\cos\theta_Y\cos\theta_Z & -\cos^2\theta_Z \\ -\cos^2\theta_X & -\cos\theta_X\cos\theta_Y & -\cos\theta_X\cos\theta_Z & \cos^2\theta_X & \cos\theta_X\cos\theta_Y & \cos\theta_X\cos\theta_Z \\ -\cos\theta_X\cos\theta_Y & -\cos^2\theta_Y & -\cos\theta_Y\cos\theta_Z & \cos\theta_X\cos\theta_Y & \cos^2\theta_Y & \cos\theta_Y\cos\theta_Z \\ -\cos\theta_X\cos\theta_Z & -\cos\theta_Y\cos\theta_Z & -\cos^2\theta_Z & \cos\theta_X\cos\theta_Z & \cos\theta_Y\cos\theta_Z & \cos^2\theta_Z \end{bmatrix}.$$

The member global stiffness matrix, **K**, is calculated for each member of a space truss. The sum of all the member global stiffness matrices then forms a matrix, which can be referred to as the complete global structure stiffness matrix, **S**. The joint displacements, **d**, in global coordinates for the space truss are then calculated using the following equation:

$$\mathbf{F} = \mathbf{Sd} \tag{3-15}$$

Finally, the stress in any given member is:

$$\sigma = \frac{E}{L}\begin{bmatrix} -\cos\theta_X & -\cos\theta_Y & -\cos\theta_Z & \cos\theta_X & \cos\theta_Y & \cos\theta_Z \end{bmatrix}\begin{bmatrix} F_1 \\ F_2 \\ F_3 \\ F_4 \\ F_5 \\ F_6 \end{bmatrix} \tag{3-16}$$

3.4.2. Structural analysis

The model for carrying out the structural analysis using the stiffness matrix method for the large volume calibration artefact has already been described in section 3.4.1. A MATLAB script was used to implement the FEM structural analysis. Mechanical properties of candidate materials from which the artefact could be constructed were then used as input parameters into the analysis. The outputs from the analysis are the displacement vectors of the nodes, and the axial forces acting on the connecting members from the gravitational forces acting on the spheres. As the ultimate aim was to be able to construct a well-characterised artefact using CMM measurements on the individual rods alone, the gravitational deflections are clearly important. Provided the deflections are below the level of 1/10 of the ultimate required measurement accuracy of the system, they can be neglected. Deflections above this level could still be viable if

a correction to the artefact geometry to take account of the gravitational forces can be made with confidence.

Several different geometries and material types were modelled. The final selected combination was based on T300 high stength carbon fibre tubes (fibres unidirectional along the length of the tubes – see Table 3-1 for material properties) with a nominal length of 500 mm, nominal outer diameter of 21.8 mm and wall thickness of 1.4 mm. The spheres were made from chrome steel with a nominal diameter of 50 mm (similar to the size of spheres used on the previous ball-bar artefact). The nominal separation distance between sphere centres was set to 600 mm in order to ensure full-field coverage of the measurement volume of an optical SMS. The relevant mechanical properties of all the materials used are shown in Table 3-1.

The results for nodal displacements and the axial forces in connecting members are shown in Table 3-2 and Table 3-3. The node numbers are defined in Figure 3-10. In this model, node five was constrained in X, Y, and Z, node one in Y and Z, and node 14 in Z alone. The output indicates that the maximum tensile force in any connecting member is 35.2 N, while the maximum nodal displacement along any of the axes is 3.8 µm and the maximum displacement magnitude is 4.5 µm. The total measurement volume that can be calibrated using the proposed artefact is $3 \times 1 \times 1$ m^3, assuming a maximum movement of ±0.25 m along each axis. The diagonal of this volume is 3.3 m, and the maximum displacement magnitude therefore represents an uncertainty at the level of 1 part in 700 000 of the diagonal. The gravitational deflections can thus be neglected if the target accuracy is 0.7 in 10^5 (or worse) of the measurement volume diagonal.

The nature of the forces acting on the structure i.e. whether a force is acting in tension or compression, can be recognised from the analysis through the sign convention. If a force is positive, it is in tension, whereas if it is negative, it is in compression. Compressive forces assist in keeping the structure together, whilst tensile forces act to pull the structure apart.

3.5. Calibration artefact manufacture

The large volume calibration artefact was manufactured and assembled in three stages; stage one of the artefact build consisted of six spheres and 12 T300 carbon fibre tubes. The spheres were connected to the carbon fibre tubes with end caps made of mild steel (see Figure 3-6), containing magnets inside them, in an octahedral structure formation (as shown in Figure 3-7). The design of the end caps and the magnets that were used will be discussed further in section 3.5.2.

The second stage of development extended the artefact to include a further three spheres and nine carbon fibre tubes in a double octahedral formation (as shown in Figure 3-8). This geometry was used primarily for validating the positions of the manipulator supports for the artefact. A manipulator was designed specifically to support and move the artefact around the measurement volumes (the manipulator design will be discussed further in Chapter 4).

The third and final stage extended the double octahedral structure to an extended octahedral formation, consisting of 15 spheres and 39 carbon fibre tubes of equal nominal length in total (see Figure 3-9). It was this final formation of the artefact supported by the specifically designed manipulator, that was later used for calibration of the multi-sensor setup (described in Chapter 6). All the spheres, magnets and carbon fibre tubing used in constructing this artefact were bought off-the-shelf. Only the end caps containing the magnets inside them were custom manufactured.

3.5.1. End cap design and manufacture

The end cap design (in terms of the size and shape) to connect the carbon fibre tubing to the sphere's was influenced by the type of magnet necessary. Selecting the appropriate magnet was dependent on the outcome of the structural analysis performed modelling the large volume calibration artefact, as described in Section 3.4.2. Clearly the magnetic force required would have to be greater than the maximum tensile force present in the artefact. However, the magnet diameter must also be sufficiently small that the resulting end cap does not optically obscure the surface of the sphere to which the end cap is attached. The magnet considered the most appropriate under these conditions was the

high strength neodymium rod magnet (Supermagnete S-12-60-N), with a diameter of 12 mm, nominal length of 60 mm and average weight of 52 g [87]. The magnetic strength rating of the magnet quoted by the manufacturer was 62.8 N, compared to the predicted maximum tensile force from the analysis of 35.2 N, thus providing a failure safety factor of 1.8.

When designing the end cap to contain the magnet, an important consideration was limiting the obstruction of the view of the sphere's surface by the optical SMS whilst also keeping the weight to a minimum. Black acetal polymer tubes were also inserted into the bores of the end caps, these were used for guiding the magnets into the end caps safely and securely during assembly.

3.5.2. End cap testing

In order to ensure that the end caps met the design intent and provided the necessary magnetic strength, despite the presence of the small air gap between magnet and sphere surface, a prototype end cap was manufactured for testing. Pull-off tests were carried out on a tensile testing machine (Lloyd Instruments – LRX) in which the end cap was held fixed into position at the bottom end of the machine in the vertical position, using the machine's vice. A test sphere was carefully placed on top of the end cap, with the magnetic force 'locking' the two surfaces together. A separate clamp was used to grip the sphere from the top end of the machine, so that the machine could grip and pull the sphere away from the end cap. This test was repeated ten times in total, so that the repeatability of the strength could be established. The results from the tests are given in Table 3-4; a typical force-time curve is also shown in Figure 3-11. The results confirmed that the average pull-off force recorded was 62.9 N ± 0.5 N, which was a very close match to the manufacturer's stated pull-off force of 62.8 N [87].

3.6. Thermal and hygral effects

The main material used for the connecting rods in the large volume calibration artefact (i.e. carbon fibre) was selected. However, the connecting rods are a composite device consisting of carbon fibre and steel joined together by adhesive; the carbon fibre tube surfaces were also lacquered on the outside thus affecting the rate at which moisture

enters the tube. The overall performance of the tubes and more importantly the adhered rods therefore still needed verifying through experimentation, so that the effects from typical environmental conditions for calibration can be known and quantified. In this section, the results of experiments to evaluate the physical effects from changes in temperature and moisture levels are described.

3.6.1. Thermal effects

Thermal expansion can be defined as the tendency of matter to change physically in response to a change in temperature [88]. Generally, when a material is heated, its constituent atoms become more active and maintain a greater average displacement, thus they expand in length and volume [88], [89]. However, some materials experience the opposite, in that they contract in size with increasing temperature [90], [91]. The fractional degree of expansion or contraction divided by the change in temperature is called the material's coefficient of thermal expansion (CTE) [88], [89].

In order to gauge these thermal effect experimentally, a single length of carbon fibre tubing, with the end cap connections and one sphere attached to each end was housed within a specifically designed chamber (see Figure 3-12). The rod was supported inside the chamber with only 10 mm of each end cap exposed to the external environment. This chamber was then heated in an oven at 50°C over a period of one week. The chamber was carefully removed from the oven and setup on the Metris LK Ultra mechanical CMM, (as shown in Figure 3-12). The sphere shown on the right of the image was probed at five different locations on the surface to establish its sphere centre position, and the same process was repeated on the second sphere, together these two inspections amounted to one completed measurement cycle. The CMM was used in this way to measure the two spheres over 45 continuous cycles, with each measurement cycle taking ~ 75 seconds to complete.

Whilst these measurements were taking place, the chamber was cooling naturally towards the room temperature of 20.3° C. A thermometer (Hanna Instruments HI-9040) was used to monitor the temperature inside the chamber throughout the measurement period, and recorded after every five cycles. Table 3-5 summarises the results. It can be

seen that an overall length reduction of 20 µm was observed from a temperature reduction of 17.6º C, a rate of 1.1 µm per degree C. The sphere-sphere separation of 593 mm means that the effective CTE is 1.9×10^{-6} º C^{-1}. In order to achieve the desired 1 part in 10^6, the temperature of the environment should thus be controlled to around 0.5º C.

For larger temperature deviations it may be advisable to compensate the known sphere-sphere separation (as measured in a metrology lab at standard temperature) during the calibration process. It is also worth pointing out that the overall CTE of the bar is a weighted average of the carbon fibre tubes (which have negative CTE) and steel end caps and steel spheres (which have a positive CTE of much larger magnitude). By adjusting the relative lengths of the two materials it should in principle be feasible to come up with an athermal design, i.e. one with an overall CTE of zero.

3.6.2. Hygral effects

The carbon fibre tubes used in manufacturing the large volume calibration artefact can be classified in the family of materials known as carbon fibre reinforced polymer composites [92], [93]. Materials of this type differ from other materials such as metals in that low molecular weight substances such as water can easily be absorbed by them, even at room temperature. This water (or moisture) absorption can affect the material's physical structure and molecular composition [94], [95]. This phenomenon only occurs in the epoxy matrices as water cannot penetrate the fibres, and is known as the hygroscopic behaviour of the material [95]. As the glass transition temperature of the epoxy matrices is much higher than room temperature, the moisture absortion will tend to follow the mechanism described by Fick's second law of diffusion [95].

In order to investigate the hygroscopic behaviour, it is necessary to observe the physical effects of moisture absorption in the material and establish an analytical model for the observed physical effects. As well as observing the moisture absorption, it is also necessary to observe changes in the physical dimension of the material as a result of the absorption. The two variables together can then be used to calculate the coefficient of moisture expansion (CME). The CME is defined as a change in length per unit length

per weight percent of water absorbed at constant temperature and pressure [96]. The coefficient of moisture expansion is calculated using the following equation [97]:

$$CME = \frac{\Delta l / l_0}{\left(\Delta M / M_0\right)[\%]} \tag{3-17}$$

where l_0 and M_0 are the initial length and mass respectively of the material,
Δl and ΔM are the time dependent length and mass change respectively.

The moisture level in air is quantified by the relative humidity in air. For any given air temperature, the air has a capacity to hold moisture, usually referred to as water vapour [98]. Relative humidity is the ratio between the actual amount of water vapour present and the capacity that the air has at a particular moment in time. The amount of water vapour in air at any given time is usually less than that required to saturate the air. Hence, relative humidity is normally expressed as a percentage and can be calculated by the following formula:

$$Relative\ Humidity\ (\%) = \frac{actual\ water\ vapour\ density}{saturation\ water\ vapour\ density} \times 100 \tag{3-18}$$

The hygroscopic behaviour of a material can be characterised by two quantities: the equilibrium (or maximum) water mass content absorbed by the material, M_∞, which is dependent on the relative humidity of the surrounding atmosphere; and a parameter known as the diffusion coefficient, D [94], [95], [99], [100]. The diffusion coefficient quantifies the rate at which moisture is absorbed by the material per unit area. The equilibrium or maximum moisture mass content, M_∞, as a percentage of the dry mass is obtained from the following equation:

$$M_{\infty}(\%) = \frac{Maximum\ mass\ of\ wet\ specimen - Mass\ of\ dry\ specimen}{Mass\ of\ dry\ specimen} \times 100 \qquad (3\text{-}19)$$

For a sample which has not reached equilibrium, the moisture mass content, M, as a percentage of the dry mass, and which lies between the dry mass, M_0, and the maximum moisture mass content, M_{∞}, can be obtained from the following equation:

$$M = \frac{Mass\ of\ wet\ specimen - Mass\ of\ dry\ specimen}{Mass\ of\ dry\ specimen} \times 100 \qquad (3\text{-}20)$$

The diffusion coefficient, D, is described by a differential mass balance, usually known as Fick's second law of diffusion, which in a 1-D model may be written as:

$$D\frac{\partial^2 c}{\partial z^2} = \frac{\partial c}{\partial t} \qquad (3\text{-}21)$$

where D is the diffusion coefficient, z the coordinate along the direction of the sample's thickness, h, and c is the moisture concentration as a function of time, t.

In the case of the carbon fibre tubes used in the large volume artefact, the wall thickness is much less than the tube diameter and therefore a 1-D analysis is a good approximation. The following expression is commonly used as the solution of the partial differential equation (Eqn. (3-21)) [95]:

$$\frac{M - M_0}{M_{\infty} - M_0} = \left[1 - \frac{8}{\pi^2}\sum_{n=0}^{\infty}\frac{1}{(2n+1)^2}exp\left(-\frac{\pi^2(2n+1)^2}{h^2}Dt\right)\right] \qquad (3\text{-}22)$$

When $M \leq 0.5\, M_\infty$, Eqn. (3-22) can be well approximated by [95]:

$$\frac{M}{M_\infty} = \frac{4}{\sqrt{\pi}}\left(\frac{Dt}{h^2}\right)^{1/2} \tag{3-23}$$

Thus if M/M_∞ is plotted against the square root of time, $\sqrt{t}$, the initial linear part of the curve can be used to obtain the diffusion coefficient as follows:

$$D = \frac{\pi}{16} h^2 \left[\frac{M/M_\infty}{\sqrt{t}}\right]^2 \tag{3-24}$$

Two separate sets of experiments were carried out: the first set to determine the diffusion coefficient, *D*, and the second set (combined with the first set) to determine the coefficient of moisture expansion (CME). The first set of experiments involved acquiring data on the moisture mass uptake in samples of carbon fibre tubing at different moisture levels, which allows the model constants M_∞ and *D* to be determined. It should be noted that this will also take into account moisture absorption by the adhesive used in the assembly of the carbon fibre tubes, thus intentionally replicating the artefact structure and not just the carbon fibre itself. The second set of experiments identified physical changes in the geometry of a carbon fibre support tube ball-bar, while replicating the tube as it would be on the calibration artefact at varying levels of humidity.

The first set of experiments required maintenance of a given atmospheric humidity level over a long period of time (up to six months). Typically, in the United Kingdom, the relative humidy level ranges between 20% and 80% throughout the year [101]. Hence, two humidity levels were chosen for the first set of experiments, 25% and 75% respectively, thus testing towards the extreme ends of the expected range.

To maintain the two humidity levels, two closed chambers were set up, each containing a saturated salt solution, potassium acetate and sodium chloride respectively (Figure 3-13 shows one of the two chambers used). Saturated salt solutions have the distinct property that a stable environment is maintained within the closed capsules [102]–[105]. Different chemical salts provide different relative humidity levels; in practice, the humidity generated by a given salt may differ by several (%) from its tabulated handbook value, due to influences such as slow equilibration, temperature variations, impurities and incomplete saturation [106].

Experiments were done on tubes that were open to the internal atmosphere of the environmental chamber, as well as tubes that had the ends sealed so that moisture could only enter through the outer tube wall. The latter experiments simulated better the real-life situation as the end caps on the connecting rods prevent moisture absorption through the inner tube walls, and are therefore the ones whose results are reported here. The presence of an outer lacquer layer on the tubes can be expected to reduce the rate of moisture uptake (and hence the value of *D*) compared to unprotected carbon fibre.

Data was captured for the moisture mass uptake of carbon fibre tube samples kept at 25% RH and 75% RH from a dry state. A dry state was achieved by heating the samples at 40° C in an oven for a week prior to starting the moisture mass uptake experiments. Data was used to plot M/M_∞ against the square root of time, $\sqrt{t}$, as shown in Figure 3-14 and Figure 3-15. The samples were then reversed, in that the sample that was originally kept at 25% RH was then put into the chamber at 75% RH, and the sample originally kept at 75% RH was put into the chamber at 25% RH. The data plots are shown in Figure 3-16 and Figure 3-17.

As expected the moisture content of the carbon fibre samples from a dry state increases with time because of the increased environmental humidity, before levelling off towards the equilibrium moisture mass. The kinetics of diffusion are driven by the absorbed moisture mass gradient, which is high during the intial periods, before reducing as the sample moisture tends to the equilibrium moisture mass. This trend was also observed for the sample taken from 25% RH to 75% RH, as expected, as there is increased

environmental humidity. For the sample taken from 75% RH to 25% RH there is a reduction of moisture content as the humidity level has dropped.

It can be observed from the four plots that the moisture uptake behaviour exhibits a linear relationship in the initial stages of absorption, when $M/M_{\infty} \leq 0.5$. The diffusion coefficient, *D*, for all four plots can then be computed using Eqn. (3-24): $D = 1.1 \times 10^{-13} m^2 s^{-1}$ for the sample at 25% RH, $D = 1.8 \times 10^{-13} m^2 s^{-1}$ for the sample at 75% RH, $D = 6.5 \times 10^{-14} m^2 s^{-1}$ for the sample taken from 25% RH to 75% RH, and $D = 9.2 \times 10^{-14} m^2 s^{-1}$ for the sample taken from 75% RH to 25% RH. The latter two values are lower than those from the dry state and are probably more representative of the values to be expected for the artefact in normal use. The RH levels of all chambers was regularly monitored using a Vaisala HMI 31 humidity and temperature indicator with a HMP 35 probe; across all the humidity chambers used, the RH levels never deviated by more than ±0.5 %.

The second set of experiments to identify dimensional changes in the carbon fibre tubing were carried out using a manufactured humidity chamber to house a carbon fibre support tube ball-bar at 75% RH and 20° C, while periodically measuring the length of this tube in the chamber on the Metris LK Ultra mechanical CMM (as seen in Figure 3-12). The chamber used here was the same as the one used to verify the thermal effects earlier (section 3.6.1). The sample was prepared at 25% RH before insertion into the chamber. The environment of 75% RH was established once again through the use of a potassium acetate salt solution within the chamber. Three repeat measurements were taken of the support tube ball-bar every two weeks, for a period of approximately five months in total.

The results from these measurements are shown in Table 3-6. The length changes observed show that there was very little length change; the differences experienced were of the order 0.3 µm. However, at such small levels, it cannot be certain that this was the actual length change which occurred, as the uncertainty of the CMM (one part in a 500 000 of the measurement dimension) is greater than the 0.3 µm observed length

change. However this figure can still be used for the purposes of calculating an approximate CME value using Eqn. (3-17).

The data used comes from the mass uptake measurements for the sample kept at 75% RH from the dry state, and the length changes observed over a period of approximately five months from the support tube ball-bar, also kept at 75% RH. Inputting these figures into Eqn. (3-17) gives a CME $= 1 \times 10^{-5}/\%$; the order of magnitude of this value is consistent with the CME of carbon fibre observed in other works [95], [107], [108]. The low value can be attributed to the fact that the fibres are oriented along the axis of the tube. Any tendency of the matrix material to expand through moisture absorption is thus resisted by the high stiffness of the fibres. Axial or circumferential CME, which involves swelling in a direction normal to the fibres, is likely to be much higher than the axial CME but is not relevant here.

3.7. Calibration artefact characterisation

3.7.1. Methodology

Form measurements for characterising the physical dimensions of the different structural forms of the calibration artefact were performed using mechanical coordinate measuring machines (CMM). For each form of calibration artefact (octahedral and large volume), measurements were carried out in two parts: the first part involved characterising all of the supporting length tube ball-bars individually (as shown in Figure 3-6), while the second part of the measurement characterised the whole artefact structure on one of two mechanical CMMs used (Figure 3-7 and Figure 3-9). The CMM that was used for the second part of each measurement was dependent on the form of the artefact structure and its size. For the full artefact, whose maximum dimensions were $2 \times 0.6 \times 0.5$ m^3, it was necessary to sub-contract the work to a metrology company that possessed a CMM with a sufficiently large measurement volume.

Each support tube was numbered to identify it and its position within the artefact's geometry, and the two corresponding ends of each bar were marked 'A' and 'B' respectively, to define the orientation. Likewise, the spheres used were also numbered (as shown in Figure 3-10), to ensure they were positioned in the same location within

the artefact geometry every time it was assembled. The connectivity of the spheres to their respective supporting length tubes are referred to using the notation, 'A-B', in which the two letters correspond to the sphere numbers of the spheres attached to the respective ends 'A' and 'B'. For example, it may be written that support tube number seven has the connectivity '1-2', which means that, at the end marked 'A', sphere number one is attached, whilst at the end marked 'B', sphere number two is attached (see Figure 3-6).

The measurements to capture the separation distances between sphere centres on all of the individual support tube ball-bars (see Figure 3-6) were performed on the Metris LK Ultra CMM within the metrology laboratory of the Wolfson School of Mechanical and Manufacturing Engineering, Loughborough University, and involved both manual and automated stages. For each support tube ball-bar, automated probing of each of the two sphere surfaces, at five separate locations, was done to determine the diameter and circularity of the spheres. The position of the 3-D coordinates of the sphere centres in the local coordinate system was also recorded, and allowed the separation distance between sphere centres to be established. Three repeat measurements were taken of each support tube ball-bar in total, with the user prompted to remove the spheres from the support tube and re-attach between each measurement. In this way, an analysis of the repeatability could be done, as this method simulated typical usage.

In total, two phases of individual support tube ball-bar measurements were performed. Initially, 12 individual support tube ball-bars were measured as part of the initial octahedral artefact. During the second phase of measurement, all 39 individual support tube ball-bars were measured as part of the large volume calibration artefact, using the same procedure as the previous two phases. After measurement of the individual support tube ball-bars; the octahedral artefact was also characterised on a Metris LK Ultra CMM. The characterisation was done in the same manner as the individual support tube ball-bars, but measured as a complete structure (Figure 3-7). A second or repeat measurement of this artefact was also carried out, after a period of approximately five months, in order to determine dimensional stability of the artefact.

Finally, the large volume calibration artefact was characterised on a large volume Hexagon Metrology Global CMM (Figure 3-9) at Status Metrology Solutions Ltd, Nottingham. It was setup on a platform, which was designed and manufactured to hold it in position during measurement (the design and manufacture of this platform will be discussed further in chapter four). An automated program was used to probe every sphere surface at nine different locations. This enabled the diameter and circularity for every sphere to be established, as well as the position of the 3-D coordinates of the sphere centres. Two repeat measurements were taken of the whole artefact, with the artefact re-assembled between measurements to allow repeatability to be assessed.

3.7.2. Results

In total five separate sets of measurements to define artefact geometry were recorded using the procedure described above. One set of measurements were carried out on the 12 individual support tube ball-bars (Table 3-7), another two were performed on the octahedral structure artefact (Table 3-9 and Table 3-10), along with the measurement of the spheres' parameters (Table 3-8). The fourth measurement set characterised the large volume calibration artefact, both the individual support tube ball-bars and the complete structure respectively (Table 3-11 and Table 3-12); along with the measurement of the sphere's (Table 3-14).

The 12 individual support tube ball-bars were measured on the Metris LK Ultra CMM (see Figure 3-6), using a Renishaw TP 20 probe, with a 20 mm long steel stylus and 2 mm diameter ruby ball, with room temperature between 19.5° C – 20.5° C. For all 12 ball-bars, the measurement uncertainty of the separation between sphere centres was ±5 µm. The accuracy of the measurement achieved was thus of the order 1 part in 120 000. Similarly, the two measurements carried out on the octahedral structure utilised the same equipment, and room temperature between 19.5° C – 20.5° C. Measured as a structure (see Figure 3-7), changes in length compared with the individual ball-bars were to be expected, due to the gravitational effects, and are indeed observed.

For the first measurement of the structure, the measurement uncertainty was ±5 µm. For the second measurement of the structure, measured approximately five months

afterwards, the average measurement uncertainty was ±5 µm. The root mean square (RMS) error between the first and second measurement was 16 µm, excluding ball-bar 13 from this evaluation as it had to be replaced due to damage in the intermittent period between measurements. The repeatability of each measurement was of the order 1 part in 120 000, while the reproducible accuracy was better than 1 part in 35 000.

The 39 individual support tube ball-bars of the large volume calibration artefact were measured on the Metris LK Ultra CMM (see Figure 3-6), using a Renishaw SP 25 probe, with a 20 mm long steel stylus and 2 mm diameter ruby ball, with room temperature between 19.5° C – 20.5° C. For all 39 ball-bars, the measurement uncertainty was ±5 µm. The accuracy of the measurement achieved was of the order 1 part in 120 000. Characterisation of the large volume calibration artefact as a complete structure had to be performed on a different CMM, due to the extra measurement volume required to capture the complete structure in one measurement set. The artefact was instead measured on a Hexagon Metrology Global CMM (Figure 3-9), using a Renishaw TP 20 probe, with a 50 mm long carbon fibre stylus and 6 mm diameter ruby ball, with room temperature between 19.5° C – 21.5° C.

The measurement uncertainty for the large volume calibration artefact was ±10 µm. The accuracy of the measurement achieved was of the order 1 part in 60 000. As the measurement accuracy of the optical SMS is of the order 1 part in 20 000, the large volume calibration artefact has been characterised to an accuracy three times better than this, using higher level measurement standards (i.e. mechanical CMMs with UKAS accreditation).

3.8. Summary

Previous work has demonstrated that the development of a well-characterised calibration artefact is fundamental to the successful operation of an optical SMS. The challenges presented by the creation of a larger overall measurement volume from the setup of two or more adjacent SMSs required the development of a new large volume calibration artefact. This artefact was manufactured using mainly off-the-shelf components to replace the previously used ball-bar or planar ellipse artefact. The major

advantage of using the larger calibration artefact over the other artefacts is that the coordinate systems of the multiple measurement volumes are linked to high accuracy through the well-characterised system of bars and spheres. It also retains the benefits of the ball-bar artefact, in that it provides traceability for calibration through higher level measurement standards, and it is easily reconfigurable and deployable for in-the-field calibration.

To ensure the large volume calibration artefact was suitable for its intended purpose, a structural analysis was performed so that the gravitational forces in the support rods and resulting displacements of the spheres could be modelled. This demonstrated that a space-filling structure, suitable for characterising a $3 \times 1 \times 1$ m^3 measurement volume, could be constructed from standard carbon fibre tubing and steel reference spheres with gravitational deflections of the order of 1 part in 10^6 of the measurement volume diagonal.

The component materials were thoroughly tested for their thermal and hygroscopic behaviours. An inherently simple and robust method was used to quantify the thermal effects, in which a support tube ball-bar enclosed in a chamber was heated and then measured as it cooled. The observed changes in length between sphere centres was then recorded, from which the magnitude of the thermal effects could be defined, and subsequently compensated for during the calibration process if necessary. The composite CTE for the structure was found to be 1.9×10^{-6} ° C^{-1}, i.e. about 15% of the value for an equivalent artefact constructed from steel or aluminium.

An experimental study was carried out to observe the moisture absorption in carbon fibre tube samples at two different levels of relative humidity. The mass uptake in moisture was observed, from which the diffusion coefficients were calculated using Fick's second law of diffusion. In addition, length changes in a connecting rod associated with a step change in the relative humidity of the surrounding air were measured directly over an extended time period. The measured change was smaller than the uncertainty of the mechanical CMM used to observe it. The resulting order of magnitude value for CME value was found to be comparable with those from other

studies, and can be assumed to have negligible dimensional effect on the artefact under the conditions it will normally be operated at.

Full measurement characterisation was accomplished on the large volume calibration artefact, using two mechanical CMMs. The different stages of artefact build prior to this artefact were also characterised, along with smaller component of each of the structures (i.e. the support tube ball-bars). For the complete structure, the measurement uncertainty achieved was ±10 µm, hence a measurement accuracy of 1 part in 60 000. As the measurement accuracy of the optical SMS is of the order 1 part in 20 000, the large volume calibration artefact has been fully characterised to an accuracy three times better than this, using higher level measurement standards.

3.9. Tables

Material	**Elastic Modulus E (GPa)**	**Density ρ (kg m^{-3})**	**CTE ($°C^{-1}$)**
Carbon Fibre T300 - High Strength	160	1800	-0.38
Mild Steel	205	7800	12.8
Chrome Steel	200	7830	11.4

Table 3-1: The relevant mechanical properties of the materials used to manufacture the large volume calibration artefact.

Structural Analysis of Large Volume Calibration Artefact			
Node Number	Displacement (μm)		
	x	y	z
1	0.8	0.0	0.0
2	3.1	0.2	1.6
3	1.3	0.4	2.4
4	1.9	0.2	0.2
5	0.0	0.0	0.0
6	2.2	0.6	2.2
7	0.2	0.0	0.9
8	2.4	0.8	2.3
9	0.5	0.4	3.2
10	1.6	0.0	0.9
11	3.8	0.4	2.3
12	1.8	0.4	3.2
13	2.6	0.2	0.2
14	0.7	0.4	0.0
15	2.9	0.2	2.2

Table 3-2: FEA model output of the nodal displacements in each axes of 3-D space due to gravity.

Structural Analysis of Large Volume Calibration Artefact					
Node Connection	Force (N)	Node Connection	Force (N)	Node Connection	Force (N)
1-2	-17.7	3-14	-26.5	8-9	-8.8
1-3	35.4	3-15	19.9	10-11	-8.8
1-4	19.9	4-5	-55.2	10-12	17.7
1-5	-26.5	4-6	24.3	10-13	26.5
1-13	19.9	4-7	26.5	10-14	-26.5
1-14	-26.5	4-8	0.0	11-12	-8.8
2-3	-17.7	5-6	-55.2	11-13	0.0
2-4	6.6	5-7	-26.5	11-15	0.0
2-6	6.6	5-9	-26.5	12-14	-26.5
2-13	6.6	6-8	0.0	12-15	26.5
2-15	6.6	6-9	26.5	13-14	-55.2
3-5	-26.5	7-8	-8.8	13-15	24.3
3-6	19.9	7-9	17.7	14-15	-55.2

Table 3-3: FEA model output of the forces acting in each member connection between nodes due to gravity.

End Cap Pull-Off Tests	
Measurement Number	**Maximum Pull-Off Force (N)**
1	65.4
2	62.5
3	61.5
4	64.2
5	63.5
6	62.7
7	64.2
8	60.3
9	60.5
10	64.0
Mean (N)	**62.9**
Mean standard deviation (N)	**0.5**

Table 3-4: Results from the end cap pull-off test – repeated ten times.

Dimensional Change due to Thermal Effects				
Number of Cycles	**Approximate Time (s)**	**Temperature of Chamber (ºC)**	**Separation between Sphere Centres (mm)**	**Change in Length (mm)**
1	75	40.3	593.408	0.000
5	450	33.6	593.403	-0.005
10	825	30.6	593.399	-0.009
15	1200	28.5	593.396	-0.012
20	1575	26.4	593.394	-0.014
25	1950	25.6	593.392	-0.016
30	2325	24.7	593.391	-0.017
45	3450	22.7	593.389	-0.020

Table 3-5: Changes in the separation distance between sphere centres of a single support tube ball-bar from the effects of thermal expansion – CMM measurements.

CMM Measurements of Carbon Fibre Support Tube in Humidity Chamber				
Time (Hours)	Separation between Sphere Centres (mm)			Mean (mm)
	1	2	3	
0	595.8811	595.8806	595.8807	595.8808
350	595.8811	595.8812	595.8810	595.8811
700	595.8809	595.8812	595.8809	595.8810
1050	595.8807	595.8821	595.8809	595.8812
1400	595.8810	595.8811	595.8811	595.8811
1750	595.8810	595.8808	595.8806	595.8808
2100	595.8810	595.8808	595.8808	595.8809
2450	595.8811	595.8808	595.8808	595.8809
2800	595.8807	595.8812	595.8808	595.8809
3150	595.8810	595.8809	595.8809	595.8809

Table 3-6: Changes in the separation distance between sphere centres of a single support tube ball-bar kept at 75% RH following a change from 25% RH – CMM measurements with room temperature between 19.5° C – 20.5° C.

CMM Measurements of Individual Support Tubes of Calibration Artefact						
Support Tube	Sphere Connectivity	Separation between Sphere Centres (mm)			Mean (mm)	Mean Standard Deviation (mm)
		1	2	3		
7	1-2	599.962	599.963	599.962	599.962	0.000
8	1-3	599.847	599.847	599.846	599.847	0.000
9	2-3	592.994	592.994	592.995	592.995	0.000
10	1-5	599.943	599.943	599.943	599.943	0.000
11	3-5	599.947	599.944	599.944	599.945	0.001
12	2-4	599.889	599.889	599.889	599.889	0.000
13	2-6	600.020	600.015	600.012	600.016	0.002
14	4-6	599.937	599.936	599.936	599.936	0.000
15	4-5	600.001	599.997	599.999	599.999	0.001
16	6-5	599.946	599.947	599.940	599.944	0.002
17	1-4	599.933	599.929	599.930	599.930	0.001
18	3-6	599.899	599.897	599.895	599.897	0.001

Table 3-7: CMM measurement results of the indivdual support tube ball-bars that form the octahedral calibration artefact.

CMM Measurement of Spheres					
Sphere Number	Diameter (mm)				Mean Standard Deviation (mm)
	1	2	3	Mean	
1	50.000	50.000	49.999	50.000	0.0003
2	50.001	50.000	50.001	50.001	0.0004
3	50.001	50.001	50.002	50.001	0.0000
4	50.000	50.000	49.999	50.000	0.0003
5	50.000	50.000	50.000	50.000	0.0002
6	50.003	50.003	50.003	50.003	0.0000
Sphere Number	Circularity (mm)				Mean Standard Deviation (mm)
	1	2	3	Mean	
1	0.002	0.002	0.002	0.002	0.0002
2	0.002	0.003	0.002	0.002	0.0004
3	0.002	0.002	0.003	0.002	0.0002
4	0.001	0.003	0.002	0.002	0.0011
5	0.002	0.002	0.002	0.002	0.0002
6	0.002	0.002	0.002	0.002	0.0003

Table 3-8: CMM measurements of the sphere diameters and their corresponding circularity values – these spheres were part of the octahedral calibration artefact.

CMM Measurements of Octohedral Calibration Artefact						
Support Tube	Sphere Connectivity	Separation between Sphere Centres (mm)			Mean (mm)	Mean Standard Deviation (mm)
		1	2	3		
7	1-2	599.961	599.960	599.987	599.969	0.009
8	1-3	599.839	599.839	599.841	599.839	0.001
9	2-3	592.991	592.991	592.992	592.991	0.000
10	1-5	599.937	599.936	599.937	599.936	0.000
11	3-5	599.939	599.937	599.941	599.939	0.001
12	2-4	599.888	599.885	599.887	599.887	0.001
13	2-6	599.991	599.988	600.006	599.995	0.006
14	4-6	599.917	599.920	599.923	599.920	0.002
15	4-5	599.982	599.983	599.988	599.984	0.002
16	6-5	599.921	599.916	599.933	599.923	0.005
17	1-4	599.917	599.913	599.919	599.917	0.002
18	3-6	599.879	599.877	599.885	599.880	0.002

Table 3-9: CMM measurement results of the octahedral structure formation calibration artefact.

CMM Measurements of Octohedral Calibration Artefact						
Support Tube	Sphere Connectivity	Separation between Sphere Centres (mm)			Mean (mm)	Mean Standard Deviation (mm)
		1	2	3		
7	1-2	599.960	599.957	599.956	599.958	0.001
8	1-3	599.831	599.840	599.837	599.836	0.003
9	2-3	593.004	593.001	592.999	593.001	0.002
10	1-5	599.925	599.937	599.938	599.934	0.004
11	3-5	599.936	599.932	599.931	599.933	0.001
12	2-4	599.866	599.885	599.885	599.879	0.007
13	2-6	599.713	599.714	599.712	599.713	0.001
14	4-6	599.958	599.957	599.960	599.958	0.001
15	4-5	599.980	599.977	599.975	599.977	0.001
16	6-5	599.929	599.893	599.892	599.905	0.012
17	1-4	599.908	599.907	599.904	599.906	0.001
18	3-6	599.868	599.859	599.858	599.862	0.003

Table 3-10: CMM measurement results of the octahedral structure formation calibration artefact – measured a period of time after the initial measurements.

CMM Measurements of Individual Support Tubes						
Support Tube	Sphere Connectivity	Separation between Sphere Centres (mm)			Mean (mm)	Mean Standard Deviation (mm)
		1	2	3		
7	1-2	599.888	599.889	599.889	599.889	0.0002
8	1-3	596.138	596.133	596.131	596.134	0.0021
9	2-3	599.892	599.894	599.894	599.893	0.0005
10	1-5	597.708	597.708	597.708	597.708	0.0002
11	3-5	594.039	594.039	594.040	594.040	0.0003
12	2-4	594.459	594.459	594.459	594.459	0.0002
13	2-6	596.719	596.720	596.719	596.719	0.0003
14	4-6	599.954	599.954	599.954	599.954	0.0001
15	4-5	599.918	599.918	599.918	599.918	0.0000
16	6-5	599.823	599.822	599.822	599.822	0.0001
17	1-4	599.899	599.898	599.899	599.899	0.0001
18	3-6	599.920	599.920	599.920	599.920	0.0002
19	5-9	599.293	599.292	599.293	599.293	0.0001
20	5-7	599.186	599.181	599.182	599.183	0.0015
21	7-9	599.971	599.969	599.971	599.970	0.0005
22	7-8	598.051	598.051	598.053	598.051	0.0006
23	8-9	599.768	599.767	599.768	599.768	0.0003
24	4-8	599.988	599.989	599.988	599.988	0.0004
25	6-8	599.834	599.834	599.833	599.833	0.0005
26	4-7	599.967	599.968	599.970	599.968	0.0008
27	6-9	599.562	599.560	599.561	599.561	0.0006
28	10-14	599.904	599.904	599.903	599.904	0.0002
29	12-14	600.005	600.005	600.004	600.004	0.0003
30	10-11	600.023	600.025	600.024	600.024	0.0003
31	12-11	599.997	599.997	599.996	599.997	0.0004
32	10-12	595.142	595.143	595.142	595.142	0.0003
33	11-13	600.605	600.604	600.604	600.604	0.0002
34	11-15	599.750	599.753	599.749	599.751	0.0011
35	10-13	599.991	599.991	599.991	599.991	0.0001
36	12-15	600.828	600.837	600.831	600.832	0.0027
37	14-3	599.924	599.925	599.922	599.924	0.0007
38	14-1	599.887	599.887	599.886	599.887	0.0004
39	13-14	599.988	599.990	599.989	599.989	0.0005
40	15-14	599.972	599.969	599.967	599.969	0.0016
41	13-15	593.854	593.854	593.851	593.853	0.0009
42	13-2	597.863	597.863	597.863	597.863	0.0002
43	15-2	600.003	600.002	600.003	600.003	0.0001
44	13-1	599.988	599.986	599.984	599.986	0.0012
45	15-3	600.025	600.023	600.025	600.024	0.0007

Table 3-11: CMM measurement results of the indivdual support tube ball-bars that form the large volume calibration artefact.

CMM Measurements of Large Volume Calibration Artefact					
Support Tube	Sphere Connectivity	Separation between Sphere Centres (mm)		Mean (mm)	Mean Standard Deviation (mm)
		1	2		
7	1-2	599.885	599.886	599.885	0.0002
8	1-3	596.125	596.097	596.111	0.0137
9	2-3	599.874	599.857	599.865	0.0087
10	1-5	597.697	597.697	597.697	0.0000
11	3-5	594.018	593.987	594.003	0.0156
12	2-4	594.446	594.446	594.446	0.0003
13	2-6	596.899	596.687	596.793	0.1064
14	4-6	599.947	599.944	599.945	0.0016
15	4-5	599.914	599.915	599.914	0.0005
16	6-5	599.828	599.829	599.828	0.0004
17	1-4	599.911	599.968	599.940	0.0285
18	3-6	599.905	599.879	599.892	0.0127
19	5-9	599.296	599.297	599.296	0.0009
20	5-7	599.181	599.177	599.179	0.0020
21	7-9	599.950	599.954	599.952	0.0021
22	7-8	598.037	598.039	598.038	0.0010
23	8-9	599.744	599.750	599.747	0.0028
24	4-8	599.988	599.990	599.989	0.0009
25	6-8	599.846	599.833	599.839	0.0064
26	4-7	599.946	599.945	599.945	0.0004
27	6-9	599.550	599.549	599.550	0.0004
28	10-14	599.890	599.894	599.892	0.0016
29	12-14	599.995	599.993	599.994	0.0008
30	10-11	600.021	600.022	600.022	0.0004
31	12-11	599.975	599.977	599.976	0.0011
32	10-12	595.147	595.154	595.151	0.0036
33	11-13	600.581	600.581	600.581	0.0003
34	11-15	599.715	599.716	599.715	0.0009
35	10-13	600.000	600.002	600.001	0.0009
36	12-15	600.866	600.885	600.875	0.0099
37	14-3	599.931	599.939	599.935	0.0040
38	14-1	599.890	599.887	599.889	0.0012
39	13-14	599.981	599.982	599.981	0.0006
40	15-14	599.958	599.957	599.957	0.0006
41	13-15	593.842	593.844	593.843	0.0009
42	13-2	597.862	597.862	597.862	0.0001
43	15-2	600.000	599.997	599.998	0.0016
44	13-1	599.967	599.965	599.966	0.0006
45	15-3	600.022	600.043	600.033	0.0106

Table 3-12: CMM measurement results of the large volume calibration artefact structure formation.

3-D Coordinates of the Spheres from CMM Measurements						
Sphere Number	Measurement 1			Measurement 2		
	x	y	z	x	y	z
1	0.000	977.246	0.000	0.000	977.325	0.000
2	-298.716	972.905	520.204	-298.899	972.832	520.098
3	-596.121	975.344	-0.750	-596.093	975.341	-0.956
4	0.000	488.644	348.083	0.000	488.648	348.076
5	-299.969	489.532	-171.450	-299.860	489.569	-171.521
6	-599.945	487.223	347.975	-599.942	487.305	347.844
7	0.000	0.000	0.000	0.000	0.000	0.000
8	-298.983	-3.035	517.927	-299.095	-2.984	517.865
9	-599.949	-0.422	-0.827	-599.953	-0.339	-0.958
10	-3.190	1957.326	7.702	-3.264	1957.397	7.930
11	-303.324	1954.204	527.255	-303.592	1954.133	527.371
12	-598.330	1956.815	4.824	-598.410	1956.848	4.832
13	-4.160	1464.537	349.986	-4.323	1464.529	350.103
14	-299.371	1467.701	-172.333	-299.355	1467.792	-172.318
15	-597.998	1463.597	348.008	-598.162	1463.537	347.917

Table 3-13: CMM measurement results showing the 3-D coordinates of the sphere centres on the large volume calibration artefact – machine coordinates in which sphere number seven is set as the orgin by the automated program.

Sphere Number	Diameter (mm)			Mean Standard Deviation (mm)
	1	2	Average	
1	49.994	50.001	49.998	0.0035
2	50.003	50.004	50.004	0.0005
3	50.010	50.005	50.008	0.0025
4	49.998	49.998	49.998	0.0000
5	50.002	50.007	50.005	0.0025
6	49.999	50.006	50.003	0.0035
7	49.994	49.991	49.993	0.0015
8	49.988	49.989	49.989	0.0005
9	49.997	49.991	49.994	0.0030
10	50.000	50.001	50.001	0.0005
11	50.006	50.000	50.003	0.0030
12	50.004	50.002	50.003	0.0010
13	50.014	50.012	50.013	0.0010
14	50.003	50.003	50.003	0.0000
15	50.004	50.006	50.005	0.0010
Sphere Number	**Circularity (mm)**			**Mean Standard Deviation (mm)**
	1	**2**	**Average**	
1	0.006	0.003	0.005	0.0015
2	0.004	0.003	0.004	0.0005
3	0.017	0.008	0.013	0.0045
4	0.004	0.003	0.004	0.0005
5	0.003	0.006	0.005	0.0015
6	0.004	0.009	0.007	0.0025
7	0.006	0.003	0.005	0.0015
8	0.006	0.007	0.007	0.0005
9	0.007	0.005	0.006	0.0010
10	0.002	0.003	0.003	0.0005
11	0.008	0.003	0.006	0.0025
12	0.008	0.008	0.008	0.0000
13	0.005	0.005	0.005	0.0000
14	0.002	0.002	0.002	0.0000
15	0.007	0.006	0.007	0.0005

Table 3-14: CMM measurements of the sphere diameters and their corresponding circularity values – these spheres were part of the large volume calibration artefact.

3.10. Figures

Figure 3-1: Phase Vision Ltd – Ball-bar calibration artefact.

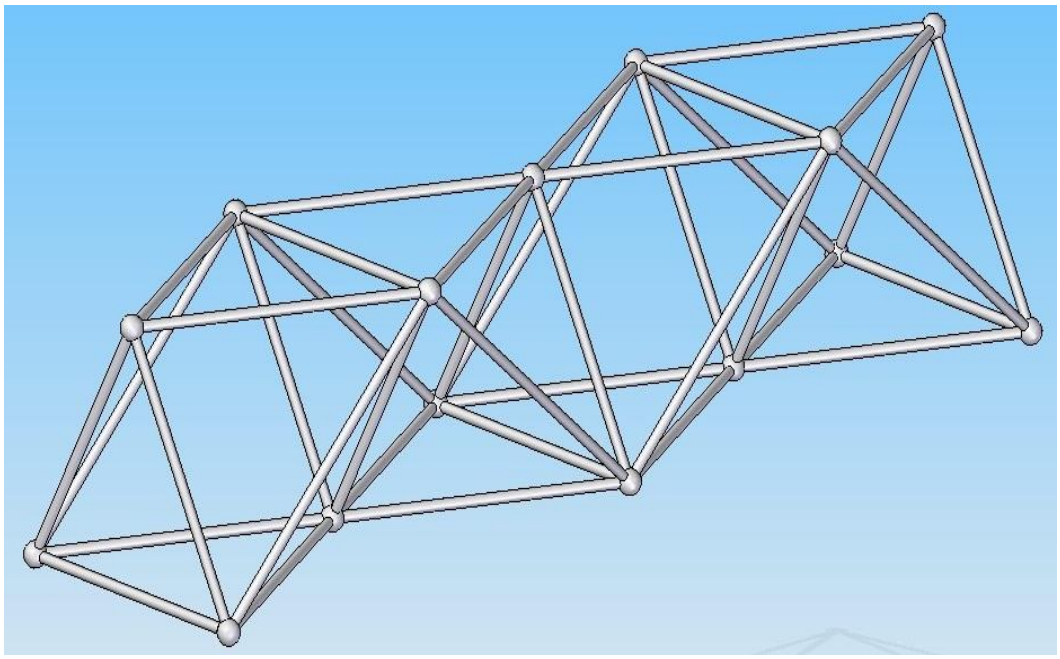

Figure 3-2: CAD model example of a networked geometry artefact.

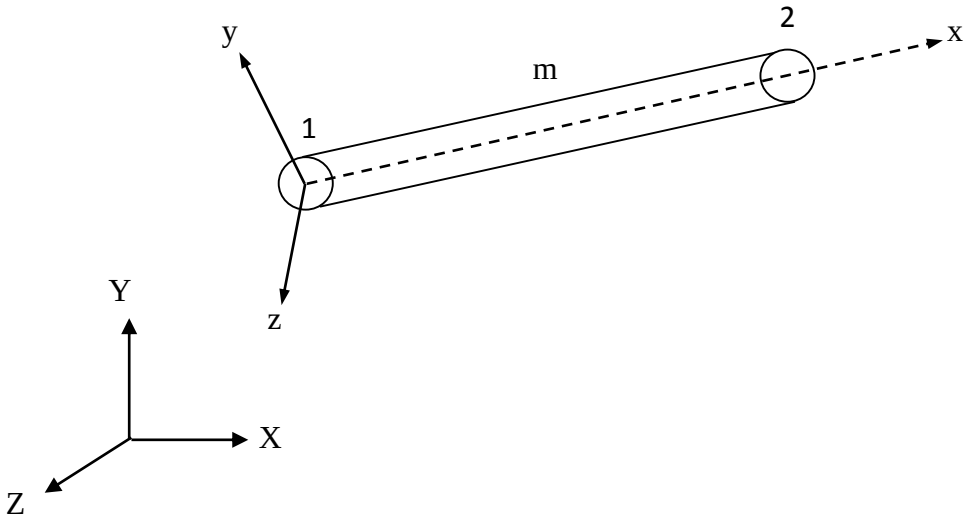

Figure 3-3: Local coordinate system for members, *m*, of a space truss [80].

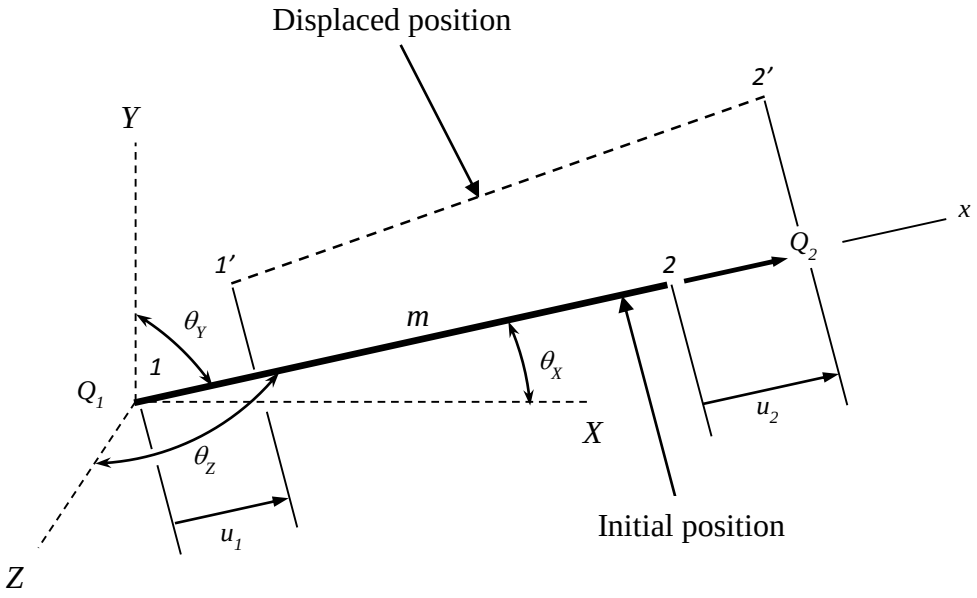

Figure 3-4: Member forces and displacements in the local coordinate system [80].

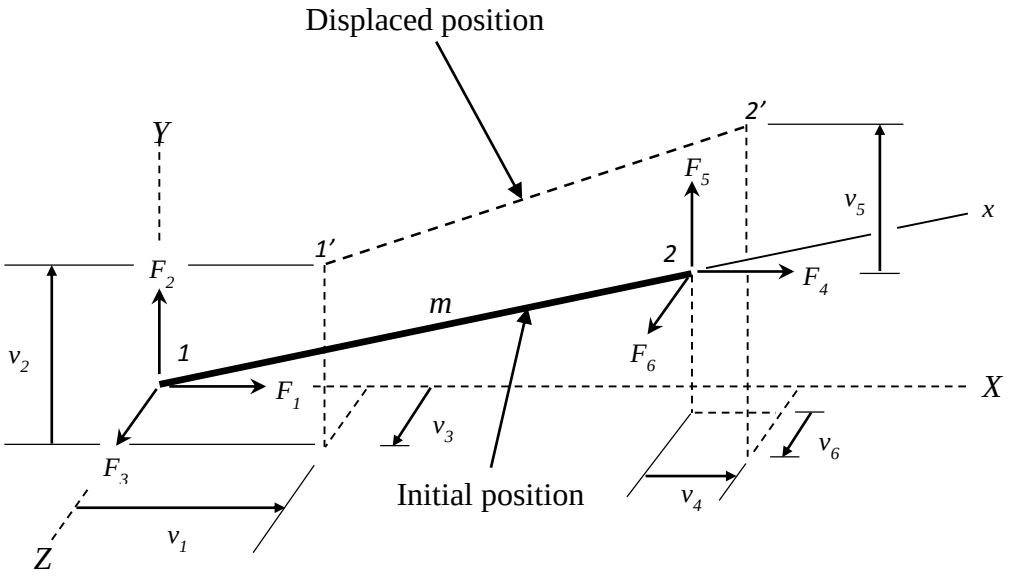

Figure 3-5: Member end forces and end displacements in the global coordinate system.

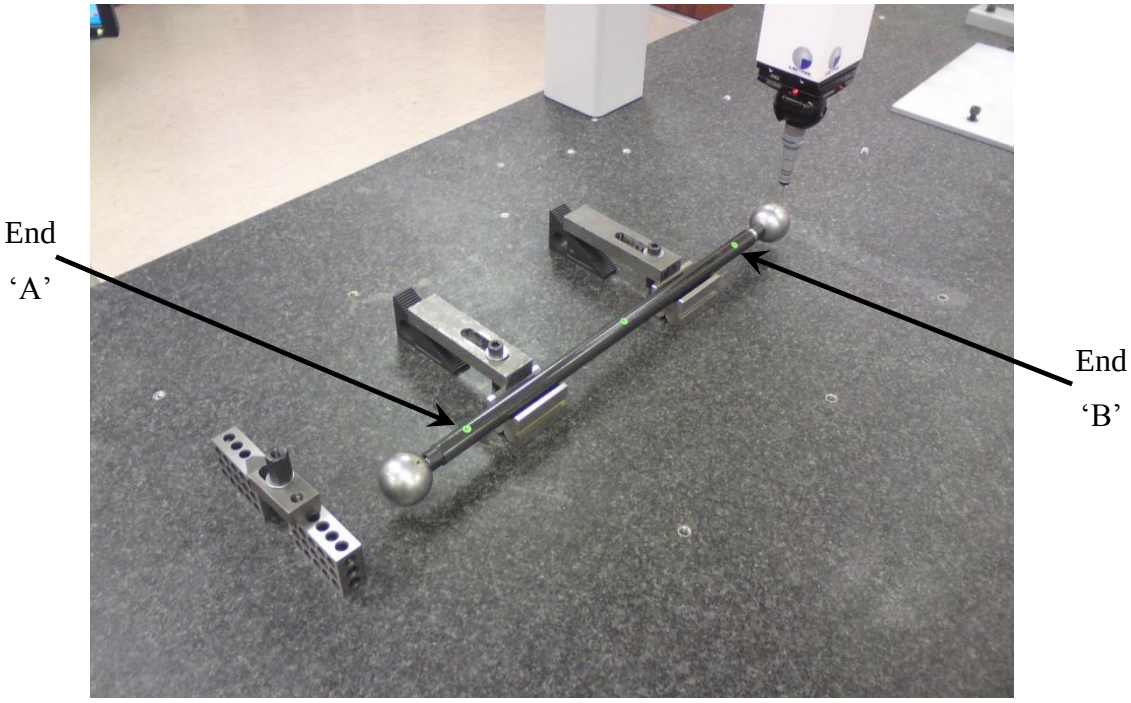

Figure 3-6: CMM characterisation of an individual support tube ball-bar with the spheres attached via end caps – using green markers to identify the correct end for each numbered sphere.

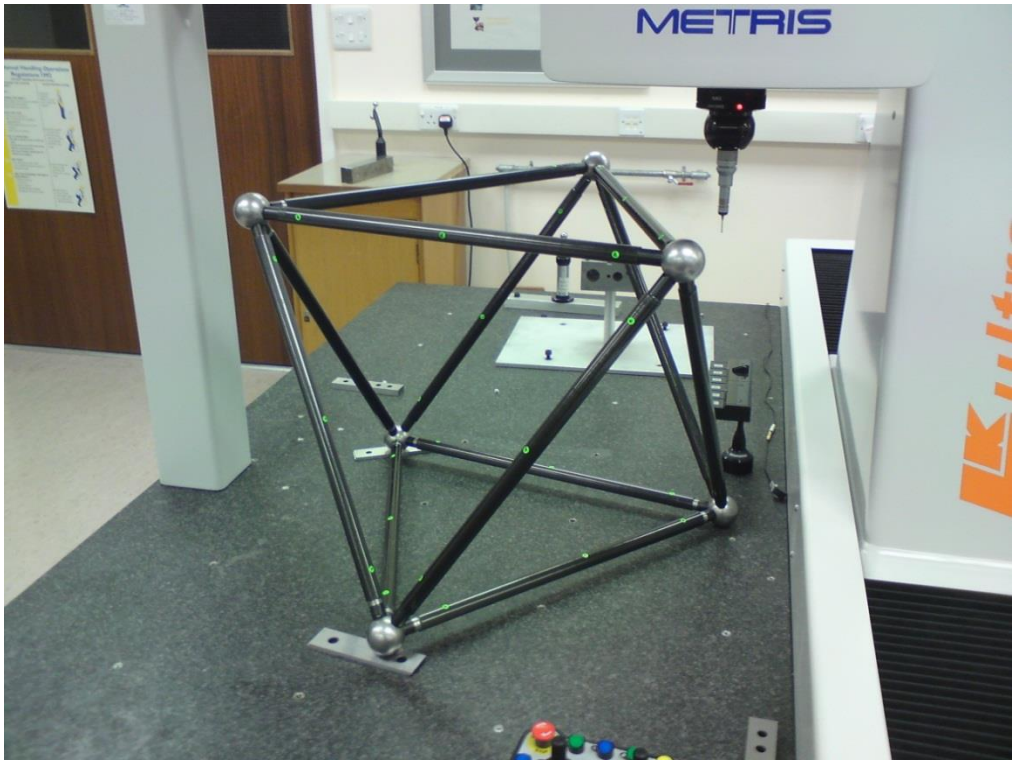

Figure 3-7: CMM characterisation of the octahedral calibration artefact.

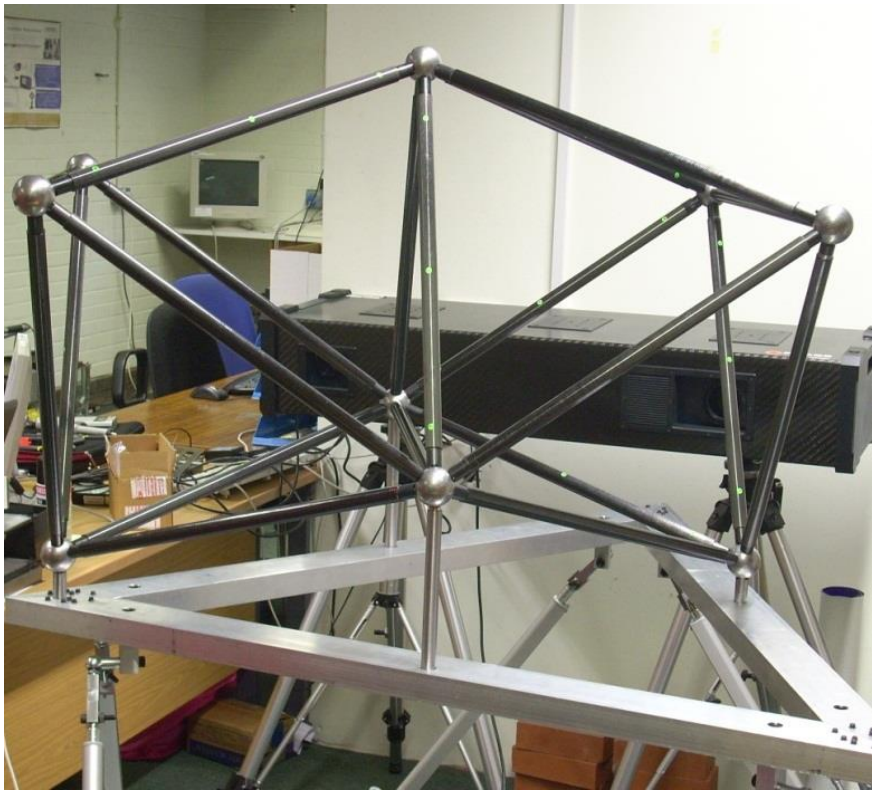

Figure 3-8: Double octahedral calibration artefact – supported by the manipulator.

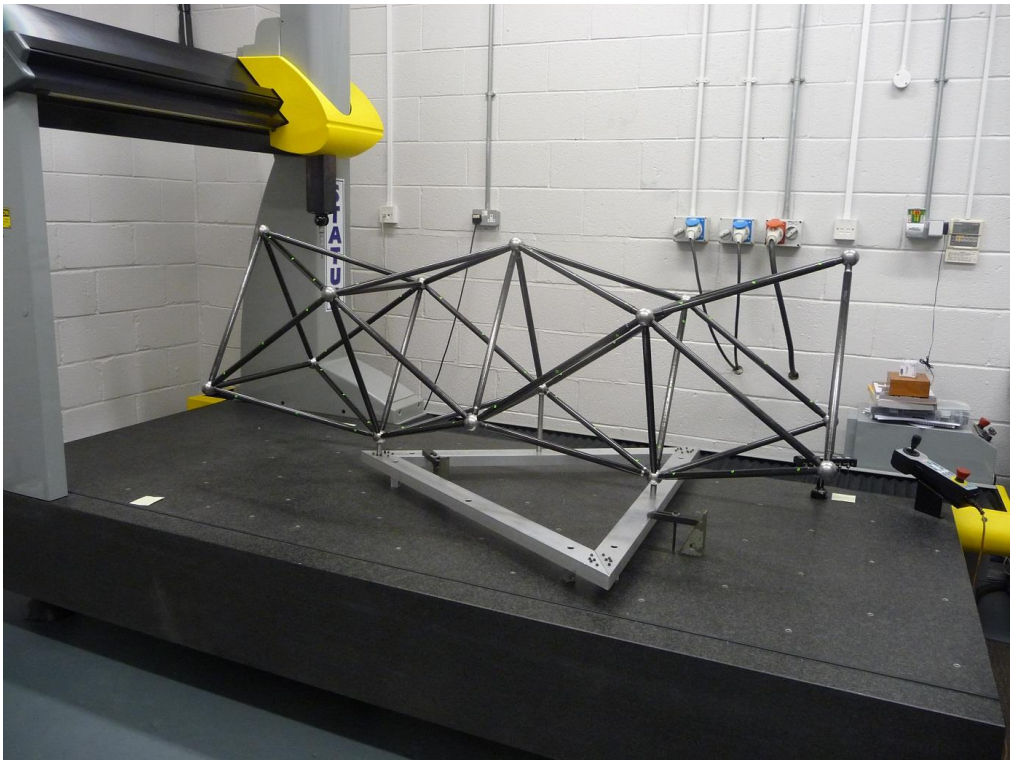

Figure 3-9: CMM characterisation of the large volume calibration artefact.

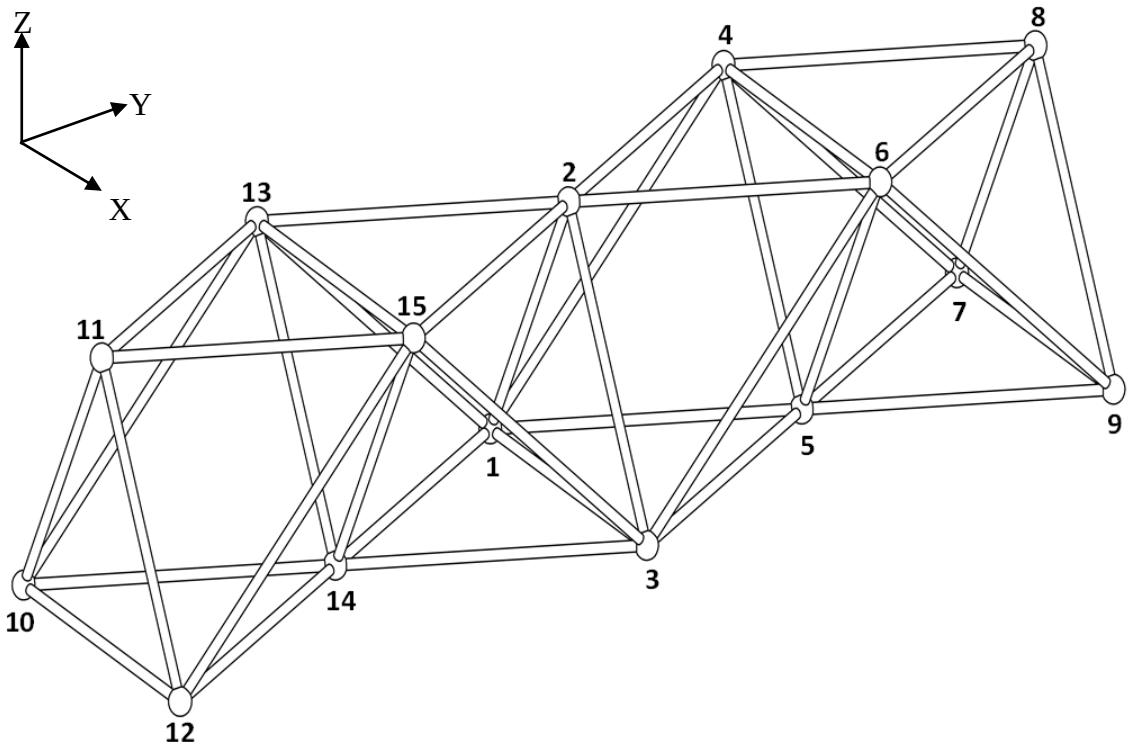

Figure 3-10: Nodal positions used in the structural analysis for modelling the large volume calibration artefact – node '10' was used as the origin (0,0,0) to define the 3-D coordinates for all the other nodes.

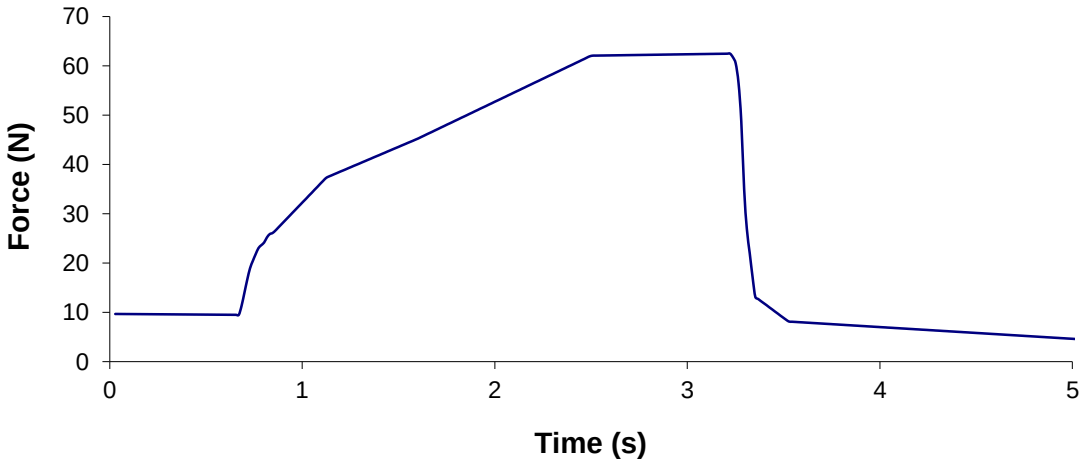

Figure 3-11: Typical force-time curve when testing the pull-off force of the end cap.

Figure 3-12: CMM measurements of the dimensional changes from thermal and hygral effects.

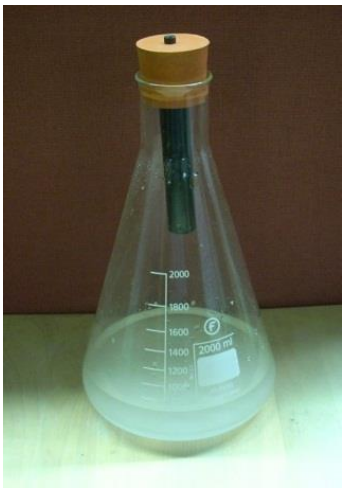

Figure 3-13: Humidity chamber used to test samples of carbon fibre at 25% and 75% RH.

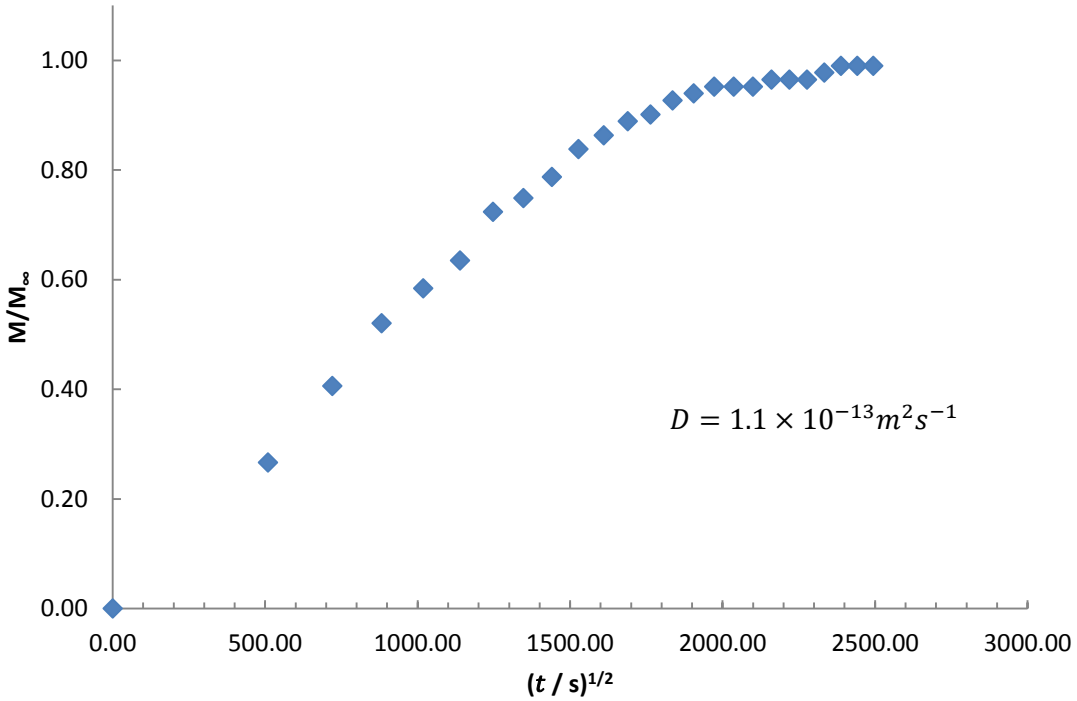

Figure 3-14: Moisture mass uptake vs. square root of time for the sample maintained at 25% RH after removal from the oven.

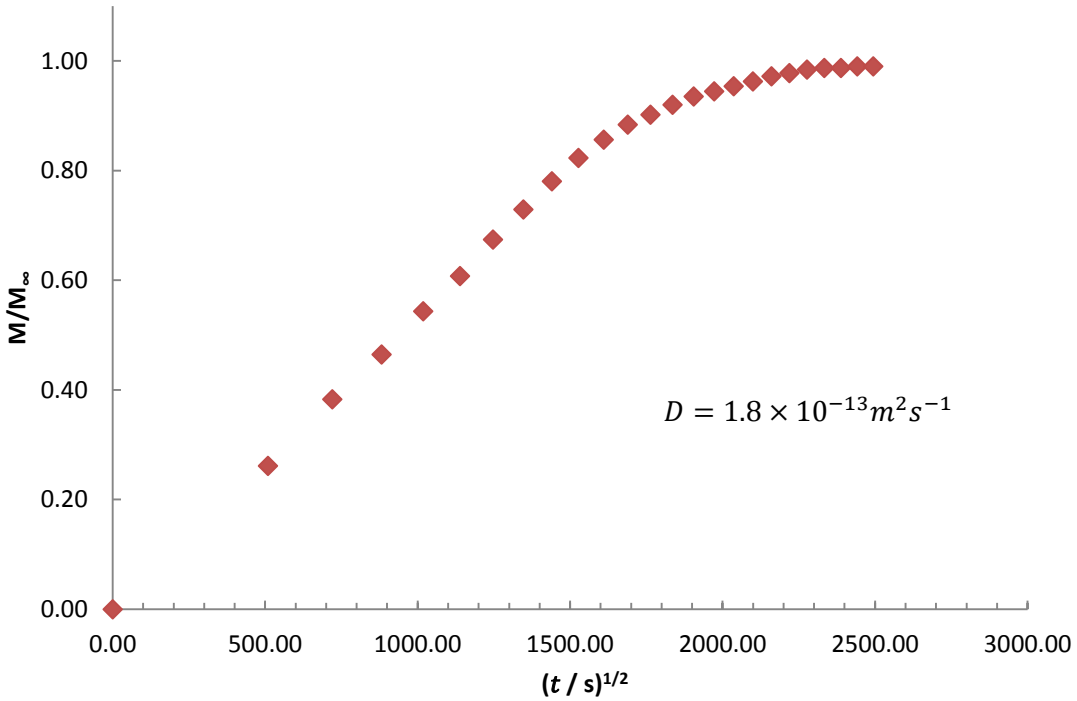

Figure 3-15: Moisture mass uptake vs. square root of time for the sample maintained at 75% RH after removal from the oven.

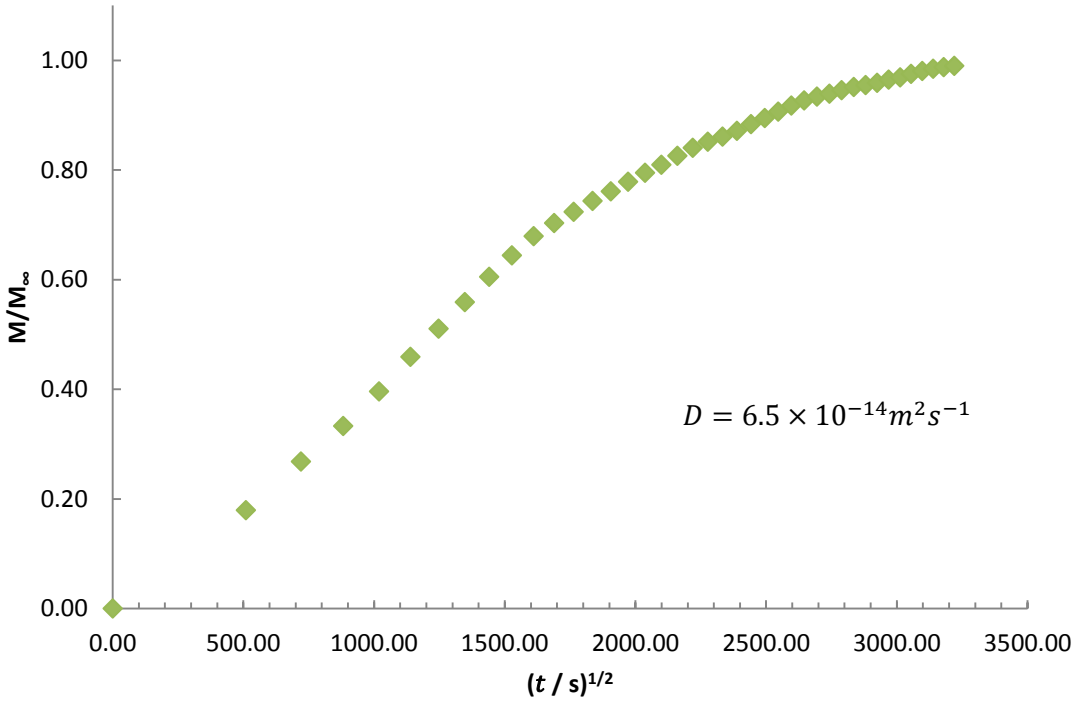

Figure 3-16: Moisture mass uptake vs. square root of time for the sample maintained at 75% RH after preparation at 25% RH.

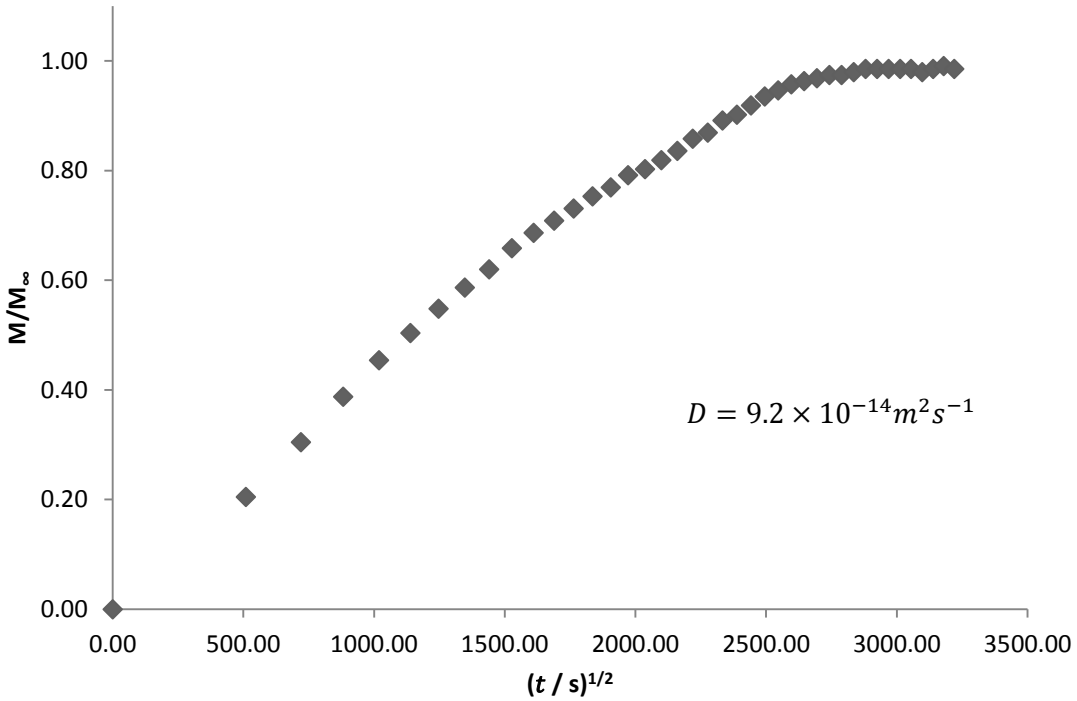

Figure 3-17: Moisture desorption vs. square root of time for the sample maintained at 25% RH after preparation at 75% RH.

Chapter 4

Positioning of calibration artefact across the measurement volumes

4.1. Introduction

The calibration artefact generally needs to be moved several times during a single calibration because a single pose does not sample a large enough fraction of the measurement volume. The bundle adjustment becomes much more robust, and more accurate calibration parameters obtained, if multiple poses are included in the analysis. In previous work, the manipulator used by Ogundana [19] for positioning a ball-bar artefact during calibration measurements was a manually operated clamp attached to a tripod (see Figure 3-1). Due to this setup a significant amount of operator input was necessary when positioning the artefact between poses, and since a dozen or more poses were required for calibration, carrying out the calibration measurements was also highly time consuming. Furthermore, the manual positioning was not very repeatable and therefore it was difficult to establish a well-characterised calibration procedure.

This manipulator was improved upon by Nguyen [78], through the use of a computer controlled pan-tilt stage with two rotational degrees of freedom (DOF) attached to a tripod (see Figure 4-1). This pan-tilt stage helped reduce the amount of time it took to capture all of the calibration measurements, as it allowed the operator to compute and automate the optimal positions of the ball-bar artefact for best coverage of the measurement volume. However, due to the extended nature of the large volume calibration artefact introduced in the previous chapter (maximum dimensions were $2 \times 0.6 \times 0.5$ m^3), the pan-tilt stage is not sufficiently robust to hold and move the larger artefact. Therefore, an alternative manipulator for positioning the large volume artefact was required. The target motion range for this manipulator was ±0.25 m along each axis, thus allowing a measurement volume of close to $3 \times 1 \times 1$ m^3 to be calibrated.

In this work the pan-tilt stage was replaced by designing and manufacturing a Stewart platform manipulator that had six DOF (shown in Figure 4-2). Movement of the manipulator's six independent, electrically driven linear actuators (also referred to as 'legs') was controlled via a computer, and the parallel structure of the base (stationary) and top (movable) platforms allowed for a very simple mechanical design and construction [109]. The ability to control via a computer, the lengths of the independent actuators, enabled positioning of the artefact in the desired locations across the multiple measurement volumes. This positioning was carried out by executing commands of the predetermined locations saved on disk, as well as providing real time control to override these predetermined positions if necessary during the shape data acquisition for calibration.

The absolute positional accuracy of the manipulator is not important as the lengthscale used in the calibration is provided by the relative posititions of the spheres, not on the motion of the artefact from one pose to the next. However, it is necessary that the artefact remains in a fixed location once a scan has been initiated. The artefact must therefore not be allowed to drift by more than approximately 1/10 of the target accuracy of the combined measurement volume (i.e., ca. 5 μm for a $3 \times 1 \times 1$ m^3 volume with target accuracy of 1 part in 20,000 of the measurement volume diagonal) during a single scan. The stability of the manipulator was therefore tested: this was done by taking measurements using an optical SMS (SMS1200 DBE) of an octahedral artefact, and monitoring the drift of the spheres over short time periods following an arbitrary translation of the artefact.

The main objectives of this work were therefore:

- To design and manufacture a Stewart platform manipulator, capable of performing a rigid body translation of the large volume calibration artefact over a range of ±0.25 m along all three axes.

- To assess experimentally the short term stability of the positioning.

4.2. Stewart platform manipulator

The Stewart platform manipulator (also referred to as a 'hexapod') is a fully parallel kinematic linkage system that is widely used in manufacturing, inspection and research applications where more than three DOF are required [110], [111]. Although for the current applications it was intended simply to translate the artefact along all three axes, the ability to introduce controlled tilt of the artefact could potentially be useful in improving the estimates of certain calibration parameters. The Stewart platform manipulator's parallel platforms and closed kinematic chain and linkage structure allows for a simple mechanical design and construction [111]. They can be made using relatively inexpensive commercially available technology, while still providing excellent rigidity and force-to-weight ratio. Positioning errors are also distributed evenly across the linkages [111].

Stewart platform manipulators are generally classified by their leg configuration. A two number notation is usually used [112]. The first number indicates the number of nodes (or joints) at the manipulator's connection to the ground frame of reference. The second number indicates the number of nodes at the movable platform. The most common structure in use today is a 6-3 Stewart platform [112]. It has six 'legs', with six nodes fixed to the ground or base platform, and three nodes on the moving platform [112]. Although the designed manipulator for this work was technically a 6-6 Stewart platform, a 6-3 configuration could be used for modelling the movement. As the manipulator was only intended for use in translation and absolute positional accuracy was not required: the approximation of the converged node positions of the three pairs of joints could be modelled as three point locations on the top platform (rather than six at the joints).

4.3. Inverse kinematics

The kinematic linkage system of the Stewart platform manipulator provides it with mechanical stiffness, and a structure that appears simple and refined to the eye, but presents a difficult problem for forward kinematics analysis [113]. However, if the manipulator's structure is simplified by modelling the geometry parametrically, inverse kinematics can then be used. This provides a much simpler solution to the problem of

locating the position of the movable platform in relation to the manipulator 'legs', i.e. to calculating the required length of the individual legs.

The following model based on that presented by Liu, Lewis and Fitzgerald [113], provides the inverse kinematics solution for the six-DOF Stewart platform manipulator (schematic shown in Figure 4-3). The inverse kinematics is the mapping from X_{p-o} (i.e. the position and orientation about X), to L_i (the respective 'leg' lengths, with i = 1,2,…,6). In other words, given the position and orientation of the top (moveable) platform in relation to the base platform, it will calculate the corresponding leg lengths. The base platform (parametric geometry shown in Figure 4-4), labelled '*Base*', is a semi-regular hexagon. The upper movable platform (parametric geometry shown in Figure 4-5), referred to as the '*Top*', is an equilateral triangle. The legs are connected to the vertices of the '*Base*' and '*Top*' with two and three DOF universal joints respectively, which gives the whole system six DOF.

A coordinate system for an inertial frame (*X, Y, Z*) is fixed at the centre of the '*Base*' with the *Z-axis* pointing vertically upwards, and another moving coordinate system (*x, y, z*) is fixed at the centre-of-gravity of the '*Top*' with the *z-axis* normal to the platform, pointing outwards. These two coordinate systems shall from now be referred to as the BASE frame and the TOP frame respectively.

The leg lengths are denoted by $L_1, L_2, \ldots, L_6$. The position vector of the TOP frame with respect to the BASE frame is denoted by $[p_x,\ p_y,\ p_z]^T$. (α, β, γ) represent the rotation angles defined by rotating the TOP frame first about the *X-axis* by α degrees, then about the *Y-axis* by β degrees, and finally about the *Z-axis* by γ degrees (see Figure 4-6). It should be noted that right-handed coordinate and angle systems are used. The α and β angles are used to define an '*approach vector*' of the upper platform. The γ angle is then used to define roll angle about the approach vector, thus the position and orientation of the upper platform is given by: $\mathbf{X}_{p-o} = [p_x,\ p_y,\ p_z,\ \alpha,\ \beta,\ \gamma]^T$.

It has already been established that one end of each leg is connected to one of the six vertices of the '*Base*'. The coordinates of these corners with respect to the BASE frame

are known and fixed (see Figure 4-4). These coordinates can be calculated from the following formulas:

$$
\begin{aligned}
&X_{B1} = \frac{\sqrt{3}}{6}(2b + d), && Y_{B1} = \frac{1}{2}d, && Z_{B1} = 0,\\
&X_{B2} = -\frac{\sqrt{3}}{6}(b - d), && Y_{B2} = \frac{1}{2}(b + d), && Z_{B2} = 0,\\
&X_{B3} = -\frac{\sqrt{3}}{6}(b + 2d), && Y_{B3} = \frac{1}{2}b, && Z_{B3} = 0,\\
&X_{B4} = -\frac{\sqrt{3}}{6}(b + 2d), && Y_{B4} = -\frac{1}{2}b, && Z_{B4} = 0,\\
&X_{B5} = -\frac{\sqrt{3}}{6}(b - d), && Y_{B5} = -\frac{1}{2}(b + d), && Z_{B5} = 0,\\
&X_{B6} = \frac{\sqrt{3}}{6}(2b + d), && Y_{B6} = -\frac{1}{2}d, && Z_{B6} = 0,
\end{aligned}
\tag{4-1}
$$

where *b* and *d* are defined in Figure 4-4. The top ends of the legs are connected to the three vertices of the upper platform, whose coordinates are fixed in terms of the TOP frame, and can be calculated from the following formulae (see Figure 4-5):

$$
\begin{aligned}
&x_{T1} = \frac{\sqrt{3}}{6}a, && y_{T1} = \frac{1}{2}a, && z_{T1} = 0,\\
&x_{T2} = -\frac{\sqrt{3}}{3}a, && y_{T2} = 0, && z_{T2} = 0,
\end{aligned}
\tag{4-2}
$$

$$x_{T3} = \frac{\sqrt{3}}{6}a, \qquad y_{T3} = -\frac{1}{2}a, \qquad z_{T3} = 0,$$

The homogeneous transformation from the TOP to the BASE frames is described by the transformation matrix, $\mathbf{T}_{\mathrm{BASE}}^{\mathrm{TOP}}$:

$$\mathbf{T}_{\mathrm{BASE}}^{\mathrm{TOP}} = \begin{bmatrix} \cos\beta\cos\gamma + \sin\alpha\sin\beta\sin\gamma & -\cos\beta\sin\gamma + \sin\alpha\sin\beta\cos\gamma & \cos\alpha\sin\beta & p_x \\ \cos\alpha\sin\gamma & \cos\alpha\cos\gamma & -\sin\alpha & p_y \\ -\sin\beta\cos\gamma + \sin\alpha\cos\beta\sin\gamma & \sin\beta\sin\gamma + \sin\alpha\cos\beta\cos\gamma & \cos\alpha\cos\beta & p_z \\ 0 & 0 & 0 & 1 \end{bmatrix} \tag{4-3}$$

$\mathbf{T}_{\mathrm{BASE}}^{\mathrm{TOP}}$ is a function of the position and orientation of the upper platform. If the trajectory of $\mathbf{X}_{p-o}$ is given, the coordinates of the upper platforms vertices in terms of the BASE frame can be calculated using:

$$\begin{bmatrix} X_{Tj} \\ Y_{Tj} \\ Z_{Tj} \\ 1 \end{bmatrix} = \mathbf{T}_{\mathrm{BASE}}^{\mathrm{TOP}}(p_x, p_y, p_z, \alpha, \beta, \gamma) \begin{bmatrix} x_{Tj} \\ y_{Tj} \\ z_{Tj} \\ 1 \end{bmatrix} \quad j = 1, 2, 3 \tag{4-4}$$

or

$$X_{T1} = p_x + \frac{a}{\sqrt{3}}\left[\sin\alpha\sin\beta\sin\left(\gamma + 60^\circ\right) + \cos\beta\cos\left(\gamma + 60^\circ\right)\right] \tag{4-5}$$

$$Y_{T1} = p_y + \frac{a}{\sqrt{3}}\cos\alpha\sin\left(\gamma + 60^\circ\right) \tag{4-6}$$

$$Z_{T1} = p_z + \frac{a}{\sqrt{3}}\left[\sin\alpha\cos\beta\sin\left(\gamma + 60^\circ\right) - \sin\beta\cos\left(\gamma + 60^\circ\right)\right] \tag{4-7}$$

$$X_{T2} = p_x - \frac{a}{\sqrt{3}}\left[\sin\alpha \sin\beta \sin\gamma + \cos\beta \cos\gamma\right] \tag{4-8}$$

$$Y_{T2} = p_y - \frac{a}{\sqrt{3}} \cos\alpha \sin\gamma \tag{4-9}$$

$$Z_{T2} = p_z - \frac{a}{\sqrt{3}}\left[\sin\alpha \sin\beta \sin\gamma - \sin\beta \cos\gamma\right] \tag{4-10}$$

$$X_{T3} = p_x + \frac{a}{\sqrt{3}}\left[\sin\alpha \sin\beta \sin\left(\gamma - 60^\circ\right) + \cos\beta \cos\left(\gamma - 60^\circ\right)\right] \tag{4-11}$$

$$Y_{T3} = p_y + \frac{a}{\sqrt{3}} \cos\alpha \sin\left(\gamma - 60^\circ\right) \tag{4-12}$$

$$Z_{T3} = p_z + \frac{a}{\sqrt{3}}\left[\sin\alpha \cos\beta \sin\left(\gamma - 60^\circ\right) - \sin\beta \cos\left(\gamma - 60^\circ\right)\right] \tag{4-13}$$

Since the coordinates of the vertices of both the '*Base*' and '*Top*' are given in terms of the same reference frame (in this case the BASE frame), the leg lengths, L_i, can be determined using:

$$L_i = |(X_{Bi}, Y_{Bi}, Z_{Bi}) - (X_{Ti}, Y_{Ti}, Z_{Ti})|; \tag{4-14}$$

Thus,

$$L_1 = \sqrt{\left(X_{T1} - \frac{d}{2\sqrt{3}} - \frac{db}{\sqrt{3}}\right)^2 + \left(Y_{T1} - \frac{d}{2}\right)^2 + Z_{T1}^2} \tag{4-15}$$

$$L_2 = \sqrt{\left(X_{T1} - \frac{d}{2\sqrt{3}} + \frac{b}{2\sqrt{3}}\right)^2 + \left(Y_{T1} - \frac{d}{2} - \frac{b}{2}\right)^2 + Z_{T1}^2} \tag{4-16}$$

$$L_3 = \sqrt{\left(X_{T2} + \frac{d}{\sqrt{3}} + \frac{b}{2\sqrt{3}} \right)^2 + \left(Y_{T2} - \frac{b}{2} \right)^2 + Z_{T2}^2} \tag{4-17}$$

$$L_4 = \sqrt{\left(X_{T2} + \frac{d}{\sqrt{3}} + \frac{b}{2\sqrt{3}} \right)^2 + \left(Y_{T2} + \frac{b}{2} \right)^2 + Z_{T2}^2} \tag{4-18}$$

$$L_5 = \sqrt{\left(X_{T3} - \frac{d}{2\sqrt{3}} + \frac{b}{2\sqrt{3}} \right)^2 + \left(Y_{T3} + \frac{b}{2} + \frac{d}{2} \right)^2 + Z_{T3}^2} \tag{4-19}$$

$$L_6 = \sqrt{\left(X_{T3} - \frac{d}{2\sqrt{3}} - \frac{b}{\sqrt{3}} \right)^2 + \left(Y_{T3} + \frac{d}{2} \right)^2 + Z_{T3}^2} \tag{4-20}$$

The last six equations (above) provide the lengths of all six individual legs, and complete the inverse kinematics solution of the Stewart platform.

4.4. Manipulator design and manufacture

The design of the Stewart platform manipulator had to take into consideration the geometry of the large volume calibration artefact it would support and position across the measurement volumes of the two adjacent optical SMSs, as well as the desired maximum translation along each axis (±0.25 m). This in essence dictated the dimensions of the variables *a*, *b* and *d* of the parametric geometry of the base and upper platforms respectively (see Figure 4-4 and Figure 4-5). In addition to defining the dimensions of the base and upper platforms, it was also essential to design and manufacture appropriate supports for the artefact in accordance with the '3-2-1' support approach (as described in section 3.4.1.), to ensure the artefact was minimally rigid when supported by the manipulator. A method for maintaining the position of the manipulator relative to the ground was also necessary, to ensure overall stability of both the manipulator, and the artefact when setup on the manipulator.

Both the base and upper platforms were manufactured from aluminium rectangular section (as seen in Figure 4-2). The shape of the base platform was an equilateral triangle bolted together at the vertices using standard M4 cap-head bolts. The bolts were screwed into removable plates that had machined threaded holes to tighten the bolts into. When the adjoining sections were fully bolted together, the plates were hidden within the internal geometry of the platform. Similarly, the upper platform was also an equilateral triangle bolted down in the same manner. For the base platform, the dimension of the corresponding variables, *b* and *d*, were 1100 mm and 450 mm respectively. Conversely, for the upper platform, the dimension of the corresponding variable, *a*, was 1100 mm.

The base and upper platforms were connected in parallel to each other, and the ground, by six linear actuators (Hiwin LAS3-1-500-24 GE). The load capacity of each actuator was 1000 N; the load capacity of the six actuators together was therefore 6 kN which was ample for the artefact mass of 50 kg. Each linear actuator had one ball-and-socket joint (RS Components 689-417) attached at each end. It was these ball-and-socket joints that linked the linear actuators to both the base and upper platforms. The stroke length of each linear actuator was 500 mm, which was driven by a 24 V DC motor. The symmetrical nature of the connectivity of the linear actuators to both the base and upper platforms, and carefully controlled machining tolerances of the parts, ensured that the upper platform remained level with both the base platform and the ground (this was regularly monitored with a spirit level). The manipulator was supported by the ground using three castors (with brakes) at the three vertices of the base platform.

The supports, designed and manufactured as part of the manipulator (see Figure 4-2), were designed so that the artefact, when setup on the manipulator, would be minimally rigid, in accordance with the '3-2-1' support approach method (as described in section 3.4.1.). The first support (shown in Figure 4-7), was manufactured to provide the artefact with three rigid body constraints in translation. The second manufactured support (shown in Figure 4-8), provided two of the rigid body constraints in translation, this support was manufactured to be longer than the others so that the artefact geometry

would remain horizontal along its length. The axis of the groove was orientated parallel to the line joining the centres of the first and second supports. A third manufactured support (shown in Figure 4-9), provided the remaining rigid body constraint, in the direction normal to the plane defined by the three supports. The three manufactured supports were spread as evenly across the geometry of the top platform of the manipulator as possible, within the constraints dictated by the overall geometry of the artefact (i.e., the positions of the supported spheres).

4.5. Testing of manipulator

4.5.1. Hardware and software

For the manipulator to be fully functional, it required extra hardware to allow the user to control the actuator stroke lengths. To provide the user with this control, a control box that connected all six actuators was designed and built by the School's electronics workshop staff, so that positional commands could be sent directly to the motors from a PC, via the control box. A low cost motor-drive board (Arduino Chip) was used to communicate from the PC to the motor-drive board, via a USB port. The control box consisted of three motor-drive boards in total, with each motor-drive board controlling the motors of two actuators.

Each actuator also had an encoder, which used 'driving counts' to relate the position of the actuator stroke from the origin, to the maximum stroke length (i.e. the driving count was zero when the stroke length was zero). It was the relationship between the driving counts for each division of stroke length (i.e. per mm) that was used to drive the actuators to a designated stroke length (which in turn was determined by the inverse kinematic solution). The communication of this data from the PC and the control box was through ASCII commands, which could either be serial line commands, or they could be saved as text files containing multiple commands and executed simultaneously.

Six text files in total were executed for testing purposes, and the results observed from translating the manipulator's top platform ±200 mm in all three axes from the central position and back, and repeated several times. There were no observed visible faults

when this testing was performed; the translated movements of the top platform were verified using a tape measure.

4.5.2. Stability test

In order to satisfy the second objective, a stability test was carried out on the manipulator to check that the drift for the period of time covering shape data acquisition, was less than the established accuracy of the optical SMS. An octahedral artefact was setup on the manipulator, making use of all three manipulator supports for the artefact, at a stand-off distance of approximately 2500 mm from an SMS1200 DBE optical SMS. An ASCII command was issued to transform the manipulator's top platform to an arbitrary position. As soon as this position was accomplished, three measurements to acquire the shape data of the artefact were made consecutively.

The first measurement was taken immediately after the manipulator had achieved its new position, the second measurement approximately two minutes later, and a third measurement approximately four minutes after the first measurement. These measurements were captured so that if any drift was present, it would be noticeable from the shape data from the three measurements. Although the time between measurements was around two minutes, the shape data acquisition took approximately 30 seconds, this was because another measurement could only be started once the processing of the measured data by the server computer within the optical SMS had completed its duty.

Post-processing of the 3-D point cloud data was then done using Polyworks (version 11.0.4). Polyworks is a general purpose commercially available software that is used for analysing point clouds [114]. It is also a more cost effective solution than developing an in-house like-for-like counterpart. Some other similar software packages that could be used include Geomagic [115], Tecplot [116], and Meshlab [117]. Table 4-1 shows the results that were obtained from a Polyworks analysis, the 3-D Cartesian coordinates of the sphere centre coordinates of the 'front' three spheres of the octahedral artefact are presented, for all three measurements (thus nine sphere centre coordinates in total).

Spheres were fitted to areas manually selected that represented the point cloud data for the front three spheres of the artefact, for all three measurements.

The results show that the average displacement for all corresponding spheres across all three measurements was 53 µm. This was the average displacement over two minutes between measurements and not over the period of time covering the shape data acquisition (i.e. ~ 15 seconds). Therefore, assuming a constant drift velocity, the displacement over the period covering shape data acquisition will be approximately one quarter of the observed displacement, i.e. approximately 7 µm. Although this was a little higher than the desired value, the effect of the drift on measured sphere separation is likely to be lower than this value as the measured position of a given sphere will be an average of its position whilst drifting. The addition of extra braking features for the actuators was therefore deemed unnecessary.

4.6. Summary

An electronically-controlled Stewart platform manipulator with six DOF has been developed. The manipulator will help manoeuvre the large volume calibration artefact across the measurement volumes of two adjacently positioned optical SMSs, in readiness for implementing the calibration process which is described in Chapter 6. The design intent and the subsequent manufacturing of the base and top platforms of the manipulator have been described. The inverse kinematics solution for calculating the actuator stroke lengths used to control the movement of the top platform relative to the base platform has been presented. The mechanical requirements of the three supports that hold the artefact on top of the manipulator, i.e. the required constraints on allowable movement, have also been accounted for.

A stability test was carried out to check the drift of the manipulator for the period of time covering shape data acquisition. An octahedral artefact was setup on the manipulator, and an ASCII command was issued to transform the manipulator's top platform to an arbitrary position. Three measurements to acquire the shape data of the artefact were made consecutively at this new position. The average displacement of the spheres across all three of these measurements was shown to be around 13 µm over the

timescale of a single measurement. This displacement was lower than the established accuracy of the optical SMS; the addition of extra braking features for the actuators was thus deemed unnecessary.

4.7. Tables

(a)

Sphere Number	Measurement One – Coordinates (mm)		
	x	y	z
1	-93.312	-165.237	-162.957
2	43.392	321.849	-485.862
3	-525.651	141.920	-444.364

(b)

Sphere Number	Measurement Two – Coordinates (mm)		
	x	y	z
1	-93.355	-165.287	-162.999
2	43.232	321.797	-485.860
3	-525.592	141.882	-444.428

(c)

Sphere Number	Measurement Three – Coordinates (mm)		
	x	y	z
1	-93.338	-165.299	-163.022
2	43.256	321.648	-485.851
3	-525.629	141.899	-444.466

Table 4-1: The 3-D Cartesian coordinates of the sphere centres relating to the front three spheres measured during the stability test experiments. (a), (b) and (c) are the results from measurements 1, 2 and 3, respectively.

4.8. Figures

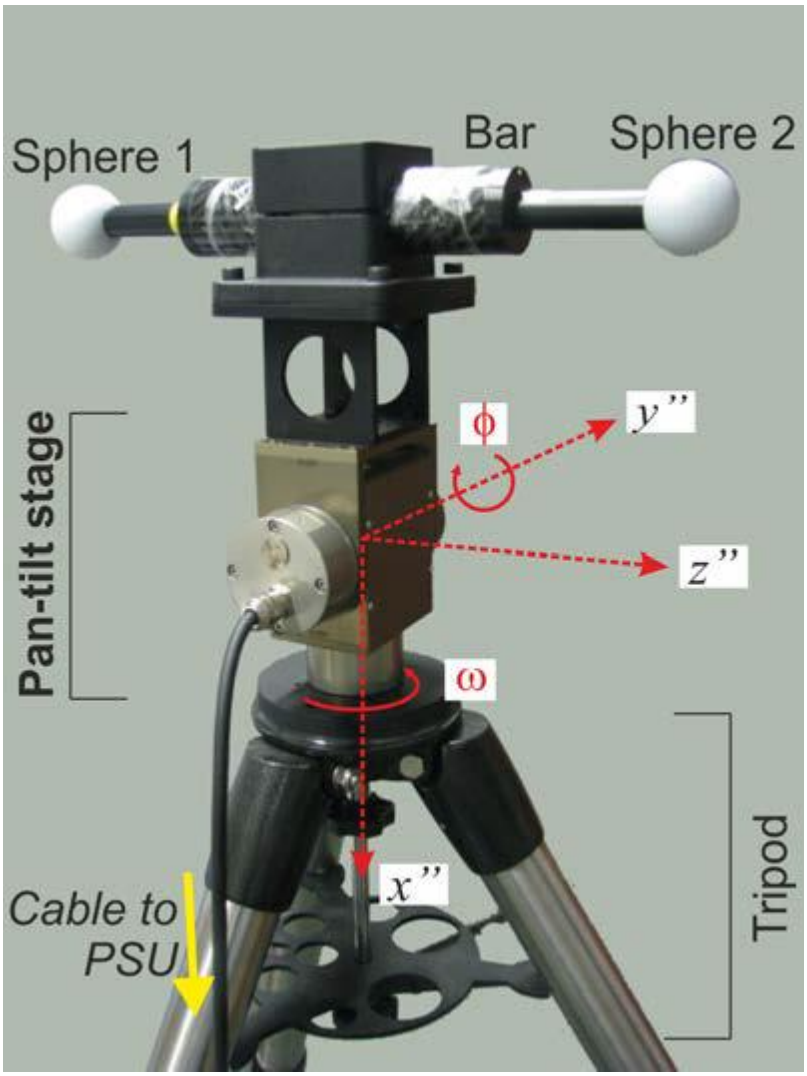

Figure 4-1: A computer controlled pan-tilt stage with two rotational DOF attached to a tripod, and supporting a ball-bar artefact [78].

Figure 4-2: Fully functional Stewart platform manipulator with six DOF.

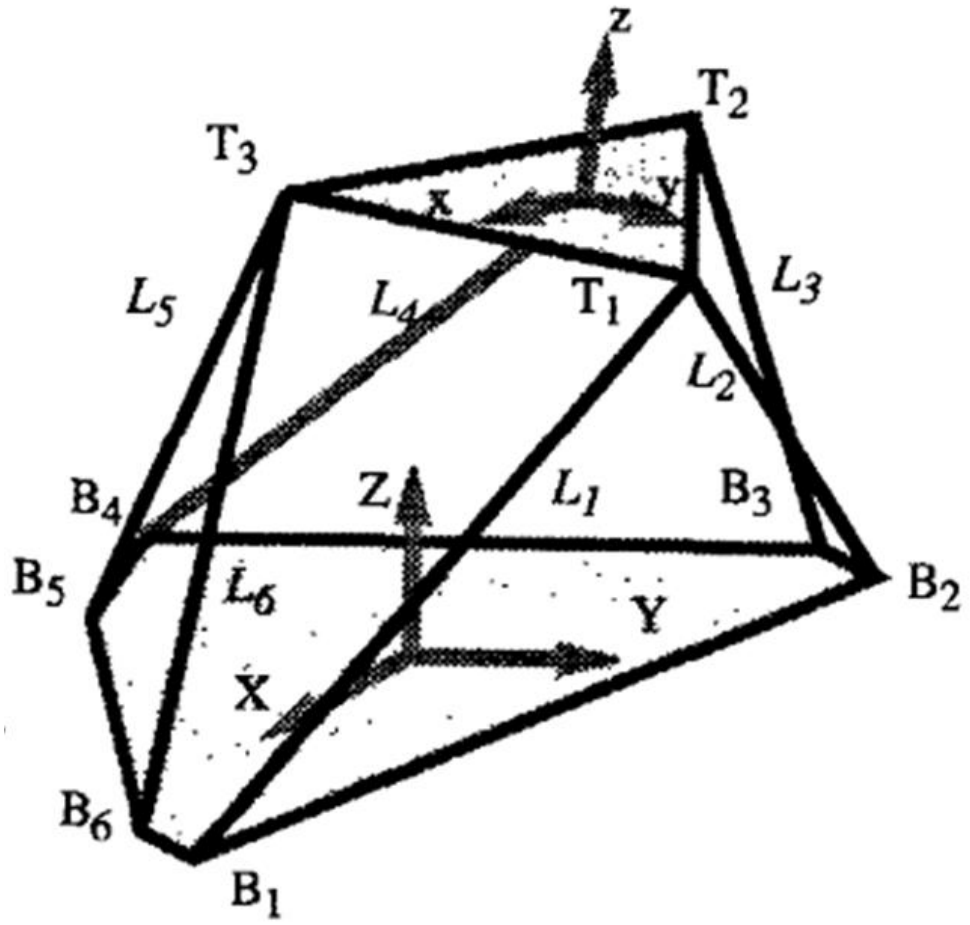

Figure 4-3: Stewart platform geometry showing the notations used for the inverse kinematics solution [111].

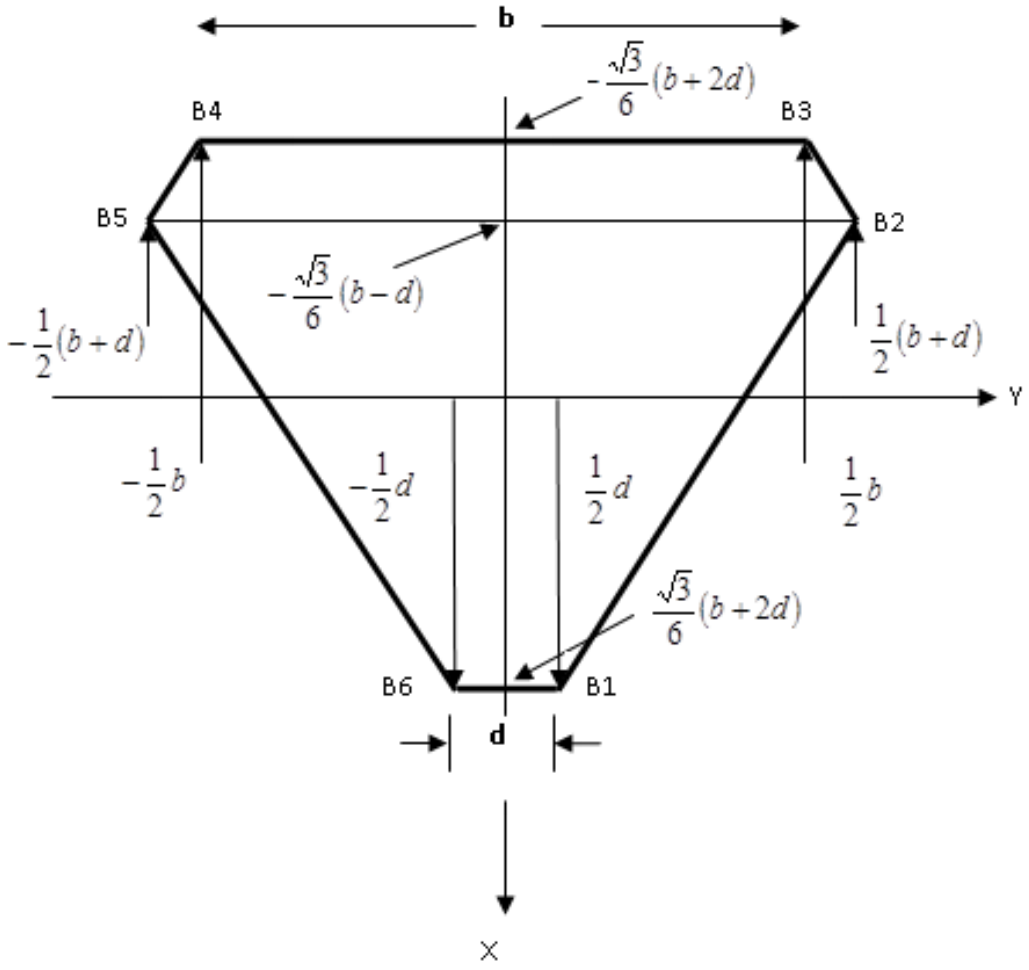

Figure 4-4: Top view of the geometry of the base platform in which the physical dimensions are defined through the parameters *b* and *d* [111].

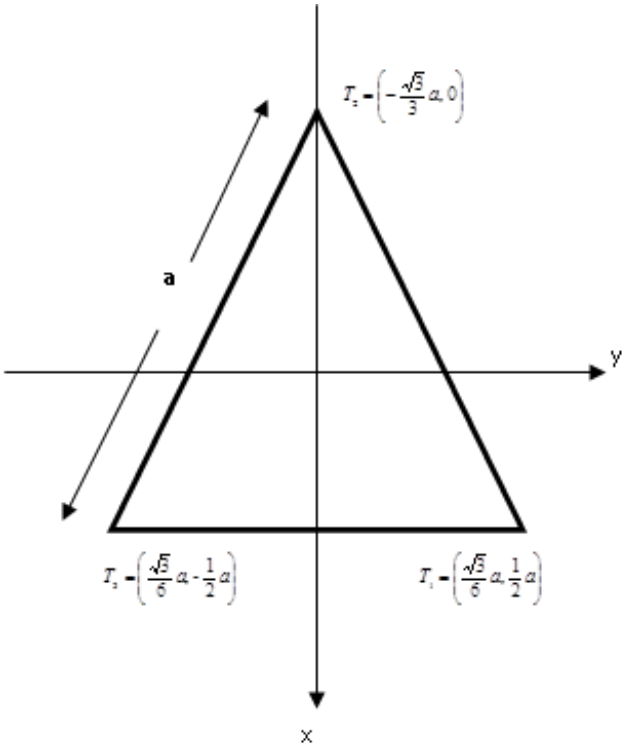

Figure 4-5: Top view of the geometry of the top platform in which the physical dimensions are defined through the parameter *a* [111].

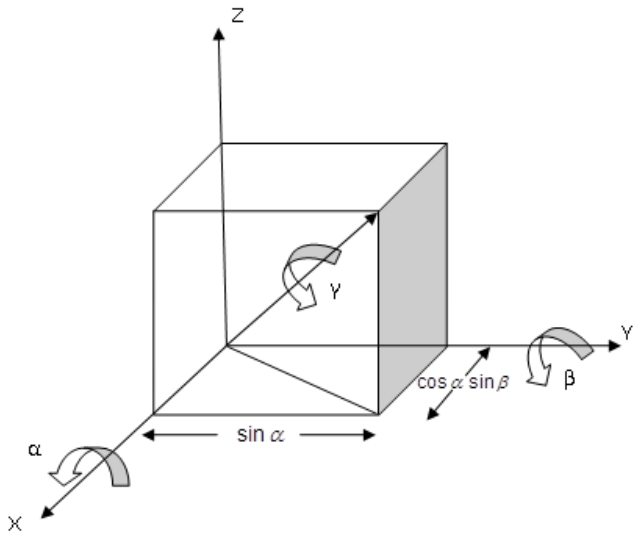

Figure 4-6: Rotation angles [111].

(a)

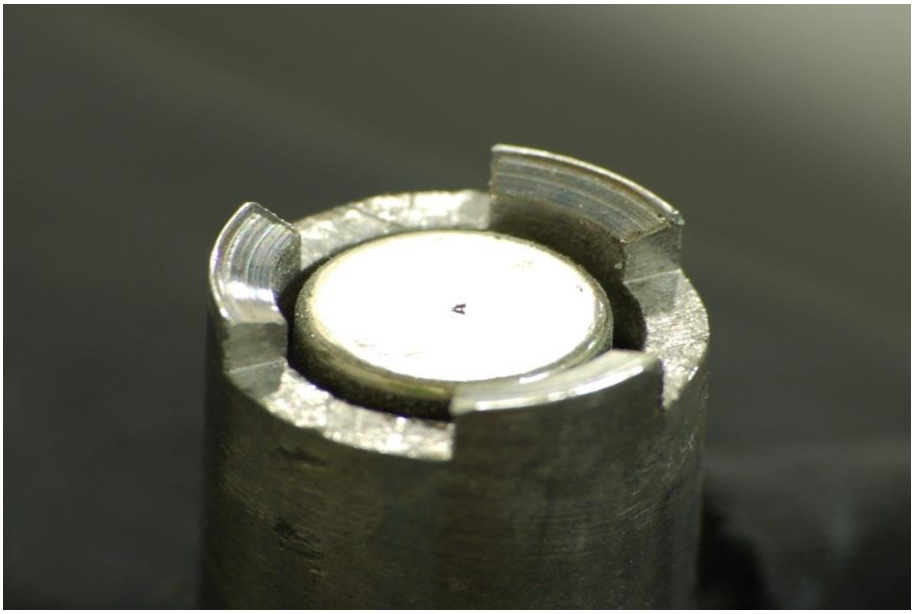

(b)

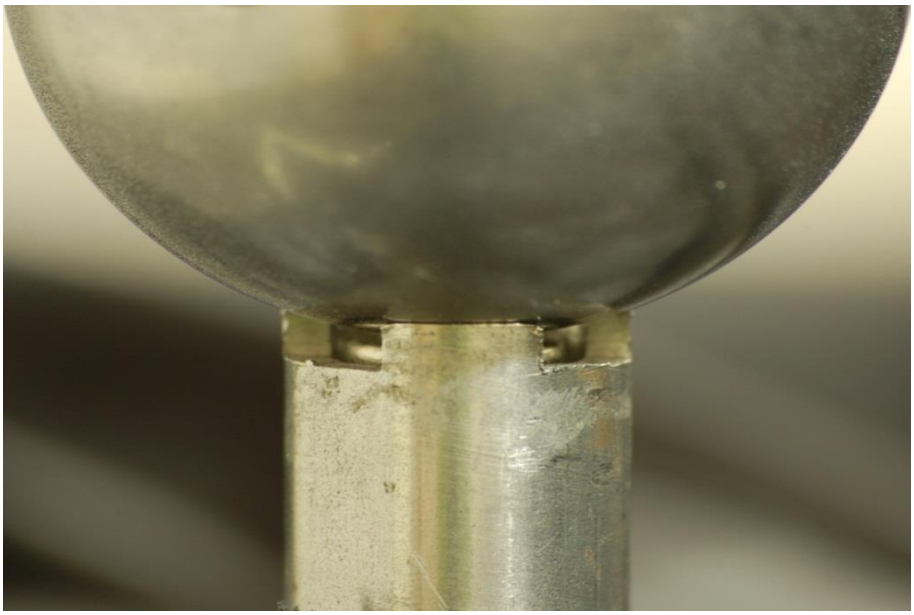

Figure 4-7: The first support, manufactured to provide the artefact with three rigid body constraints in translation. (a) Support without sphere positioned showing the magnet which provides the contact force between the sphere and the three contact areas of the support. (b) Support with sphere positioned highlighting the contact between the two mating surfaces.

(a)

(b)

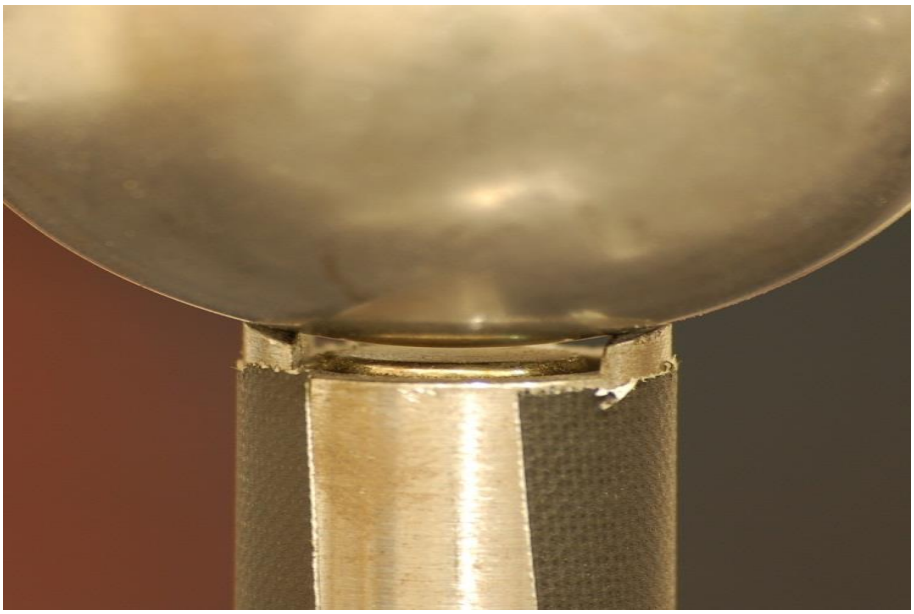

Figure 4-8: The second support, manufactured to provide two of the rigid body constraints in translation. (a) Support without sphere positioned showing the magnet which provides the contact force between the sphere and the two contact areas of the support. (b) Support with sphere positioned highlighting the contact between the two mating surfaces.

(a)

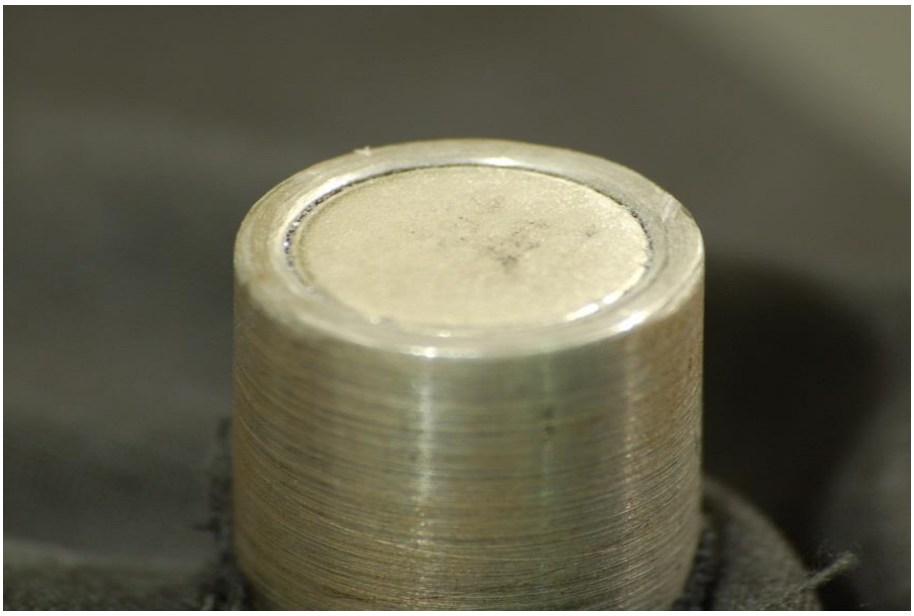

(b)

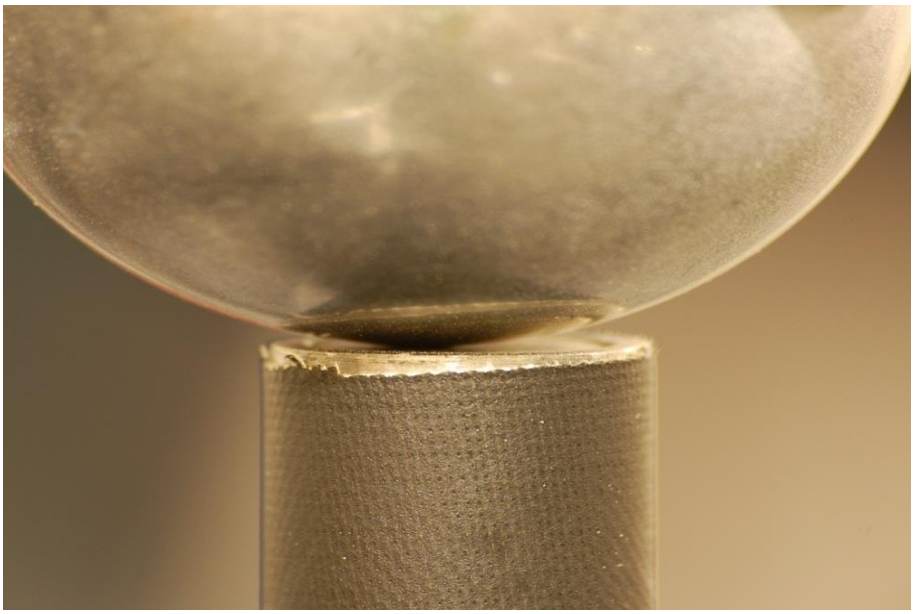

Figure 4-9: The third support, manufactured to provide the remaining rigid body constraint, in the direction normal to the plane defined by the three supports. (a) Support without sphere positioned showing the magnet which provides the contact force between it and the sphere. (b) Support with sphere positioned highlighting the contact between the two mating surfaces.

Chapter 5

Experimental analysis of measurement errors in the presence of spatial intensity gradients

5.1. Introduction

The large volume calibration artefact (as described in Chapter 3) consists of 15 spheres made from chrome steel, separated by known, fixed distances, using carbon fibre length tubing and mild steel end caps. Although the spheres provide the major benefit of defining a point in space from all viewing directions from the optical SMS, they do also have one significant drawback: the rapidly varying surface normal direction can cause strong variations in the back-scattered light intensity across a sphere's surface as measured at a fixed camera location. This in turn can introduce systematic measurement errors in the computed point cloud from the SMS (also referred to as intensity gradient errors). Therefore, it is important that this effect is well understood, so that the scale of the systematic error can be known.

The back-scattered illumination intensity (or intensity gradient) issue arises from the finite pixel size which integrates light from a finite region of a sphere's surface. If the light is brighter at one side of the pixel than the other, the computed phase change is weighted in favour of the photons landing on the bright side of the pixel. This therefore causes a bias in the direction of the computed ray from the SMS's projector into object space, and hence leads to a potential error in the calculated coordinate of the scattering point. In this chapter, this effect will be investigated experimentally to assess in practice whether significant bias is introduced into the measured location of a sphere.

5.2. Sphere-plate artefact

The chosen geometry for the experiment to test for spatial intensity gradient effects consisted of a sphere-plate artefact; a sphere made from chrome steel with nominal diameter, 20 mm, was mounted on a stalk, a fixed distance from a flat reference plate

(see Figure 5-1). The reason for using this type of artefact was to have two contrasting reference surfaces; in theory the sphere's surface would generate relatively strong intensity gradients and therefore be expected to give rise to a relatively large offset in the measured versus true sphere location.

The planar surface of the plate on the other hand has the benefit of a relatively constant surface normal, resulting in weak intensity gradients. These two contrasting surfaces were characterised using a mechanical CMM. Hence, the approach was to use the plate's planar surface as a reference surface, and then to look out for apparent shifts in the sphere's position relative to the planar surface as viewed by the camera, as the plate's planar normal vector was changed.

If there is a systematic error in the measured sphere location that causes the sphere to apparently move relative to the plane, then as the plane is pivoted around the sphere through 90º, the sphere will appear to move, either away from the plane or closer to the plane depending on where the brighter pixels are, from the point-of-view of the camera. By monitoring the apparent distance between sphere and plane over a wide range of sphere-plane orientations, changes in this distance will therefore provide an order of magnitude estimate of the errors in sphere location due to the intensity gradient phenomenon.

The planar back plate, which had dimensions of approximately 160 × 80 mm^2, was made from precision ground steel. The steel stalk attaching the sphere to the plate was machined so that a magnet could be inserted inside to provide the holding force for the sphere against the stalk. The sphere was made from precision ground chrome steel.

5.3. Experimental setup and method

The experimental setup is shown in Figure 5-2. A Phase Vision SMS1200 DBE optical SMS consisting of one projector (Projection Design F22 SX+) and one camera (Vosskuhler CCD 4000 camera with 2048 × 2048 pixel count) was used throughout. Cross hairs were projected into the measurement volume of the SMS so that the sphere-plate artefact could be positioned centrally and always close to the same physical

location within the measurement volume for all poses. Different poses of the artefact were achieved using a tilted swivel vice, which provided ample movement in all tilt, θ, and rotation, φ, directions.

For all the poses, the artefact was manually positioned so that the sphere was always positioned close to the centre of the measurement volume, using the projected cross hairs. The tilt angles, θ, were 0°, 30°, 60° and 70° (where θ is defined in Figure 5-3, 0° being normal to the SMS). The rotation angles, φ, used were -45°, -20°, 0°, +20° and +45° (where φ is defined in Figure 5-4, 0° being normal to the SMS). For every tilt angle, θ, the full range of five rotation angles, φ, were scanned; this therefore provided 20 separate measurements which were then analysed using Polyworks – version 11.0.4 (Figure 5-5 shows screen shots of a typical analysis).

The analysis involved manually selecting a ROI belonging to the plane, and a ROI belonging to the sphere. The selected points belonging to the plane and sphere, respectively, are not bound by any slope gradient threshold. A plane was fitted to the planar surface points selected, and a sphere to the spherical surface points selected, from which the perpendicular distance of the sphere centre to the plane could be computed. The Polyworks analysis was repeated five times for every measurement to quantify the variability introduced by the operator, with the mean value then used to compare the separation distance between the sphere centre and the planar surface of the plate. Graphs were then plotted using these results, with the standard deviation shown as an error bar, to see if there was any correlation between the separation distances and the rotation angle at each of the tilt angles.

5.4. Sphere-plate artefact characterisation

The sphere-plate artefact was inspected using the Zeiss UPMC 550 mechanical CMM, located at the National Physical Laboratory (NPL). Measurements were carried out to provide the plate flatness, and the separation distance from the best-fit plane to the sphere's centre. The measurement procedure involved the use of an automated stage that probed the surface of the plate in 48 different locations, including both the perimeter edge and other points spread across the plate (as shown in Figure 5-6 and

Figure 5-7). It then probed the sphere in six different locations around the sphere's surface. The measurement was repeated two more times, with the user prompted to remove the sphere from the stalk and reattach between each measurement. In this way, the repeatability of the distance between the sphere centre and plate surface was established. Table 5-1 shows the results from the CMM measurements, which show that the average plate flatness was 3 μm, and the average separation distance between the plate and sphere centre was 50.645 mm.

5.5. Experimental results

Across all 20 measured poses of the artefact, for all combinations of θ and φ, the agreement between the separation distance from the sphere centre to the surface of the plate, as measured on the mechanical CMM and optical SMS can be regarded as good. The difference between the averaged separation distance across all poses as measured by the optical SMS and the mechanical CMM measurement was 34 μm (i.e. 50.645 mm and 50.611 mm respectively). This difference was less than the measurement accuracy of the optical SMS – one part in 20 000 of the measurement volume diagonal (measurement volume ~ 850 x 850 x 1000 mm^3). The mean standard deviation of all 20 poses was 35 μm, which was less than the measurement accuracy of the optical SMS.

There were also no obvious visible trends in the data (as shown in Tables 5-2 to 5-5 and Figures 5-8 to 5-11 respectively) as φ is varied for fixed θ. There is however some evidence of small increases in systematic error as θ is increased. At θ = 0º (i.e., the normal to the plate lies in the plane containing the optical axes of camera and projector), the agreement between optical and mechanical measurement is excellent with a mean error from the optical SMS of just 4 μm. As the plate is tilted away from the plane containing camera and projector optical axes, the deviation increases monotonically with tilt angle θ: 25 μm at θ = 30º , 41 μm at θ = 60º and 64 μm at θ = 70º. A tilt angle of 70º is however a relatively shallow glancing angle for both illumination and observation directions.

Previous work by Kühmstedt et al. has demonstrated significantly increased random errors in the measured coordinates of plane surfaces under such circumstances [118];

the angular dependence of the systematic errors have not however been previously analysed in detail in the literature. The fact that under good measurement conditions for the plane (i.e., $\theta = 0^o$) the mean error was only 4 μm (better than 1 part in 350 000 of the measurement volume diagonal), and the standard deviation was just 5 μm (better than 1 part in 300 000 of the large measurement volume diagonal), suggests that for the magnitudes of intensity gradient encountered here, the resulting systematic errors can be neglected. This would not necessarily be the case, however, for spheres with more specular reflection characteristics.

5.6. Summary

A systematic study on the effect of spatial intensity gradient errors on the measured coordinates from a projected fringe optical SMS has been carried out. A 'top-down' approach was implemented in which the measured separation between a sphere and a plane was determined for 20 different poses. This approach revealed good performance of the SMS1200 DBE optical SMS used to acquire the data, with a mean error of 34 μm (better than 1 part in 45 000 of the measurement volume diagonal) between the sphere-plane separation measured by the SMS and that measured by a Zeiss CMM at the National Physical Laboratory. The deviation of the sphere-plane separation difference was 35 μm. Under the best conditions for measuring the plane surface (i.e., $\theta = 0^o$), the corresponding figures were 4 μm and 5 μm respectively. This demonstrated that intensity gradient errors – which, if significant, would have resulted in significant variations in the apparent sphere-plane separation with orientation – were not a major influence for the gradients and camera resolution encountered. The results from this chapter therefore provide confidence that the optical measurement of sphere location is sufficiently accurate for the proposed calibration procedure; this will be described in detail in the next chapter.

5.7. Tables

Zeiss UPMC 550 CMM		
Measurement	**Standard Deviation of Plate Flatness (mm)**	**Separation Distance (mm)**
1	0.003	50.645
2	0.003	50.645
3	0.003	50.645
Average	0.003	50.645

Table 5-1: Results from the Zeiss UPMC 550 mechanical CMM at the National Physical Laboratory (NPL) for the sphere-plate artefact.

Rotation Angle, φ (°)	Mean Separation Distance (mm)	Mean Standard Deviation of Separation (mm)	Mean Standard Deviation of Plate Flatness (mm)
-45	50.689	0.005	0.041
-20	50.689	0.005	0.071
0	50.639	0.006	0.074
20	50.598	0.006	0.085
45	50.589	0.004	0.094
Average	50.641	0.005	0.073

Table 5-2: Summarised results at tilt angle $\theta = 0°$.

Rotation Angle, φ (°)	Mean Separation Distance (mm)	Mean Standard Deviation of Separation (mm)	Mean Standard Deviation of Plate Flatness (mm)
-45	50.652	0.002	0.035
-20	50.646	0.007	0.056
0	50.585	0.006	0.078
20	50.599	0.005	0.085
45	50.616	0.005	0.084
Average	50.620	0.005	0.068

Table 5-3: Summarised results at tilt angle $\theta = 30°$.

Rotation Angle, φ (°)	Mean Separation Distance (mm)	Mean Standard Deviation of Separation (mm)	Mean Standard Deviation of Plate Flatness (mm)
-45	50.614	0.003	0.035
-20	50.603	0.005	0.046
0	50.613	0.003	0.054
20	50.584	0.005	0.059
45	50.606	0.003	0.057
Average	50.604	0.004	0.050

Table 5-4: Summarised results at tilt angle θ = 60°.

Rotation Angle, φ (°)	Mean Separation Distance (mm)	Mean Standard Deviation of Separation (mm)	Mean Standard Deviation of Plate Flatness (mm)
-45	50.615	0.005	0.044
-20	50.587	0.006	0.036
0	50.523	0.006	0.052
20	50.591	0.004	0.053
45	50.587	0.003	0.097
Average	50.581	0.005	0.057

Table 5-5: Summarised results at tilt angle θ = 70°.

5.8. Figures

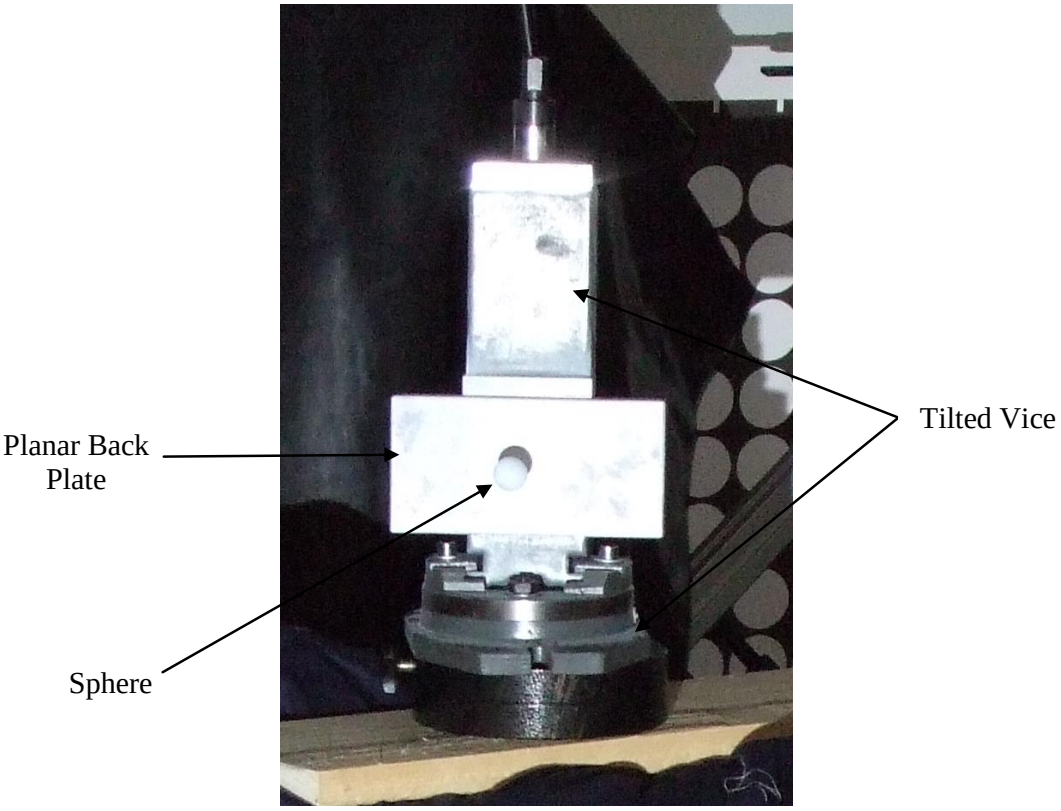

Figure 5-1: A magnified view of the sphere-plate artefact as seen by the optical SMS.

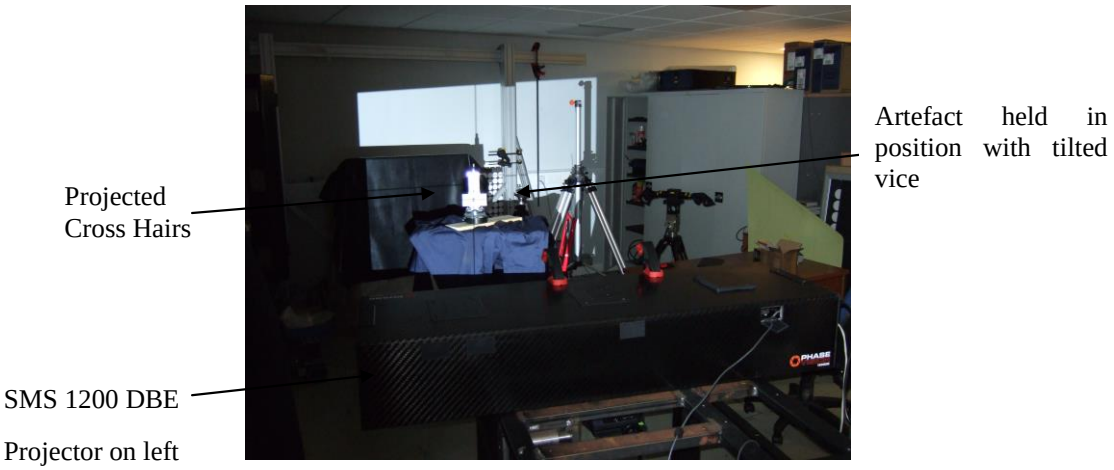

Figure 5-2: Experimental setup as viewed from behind the optical SMS.

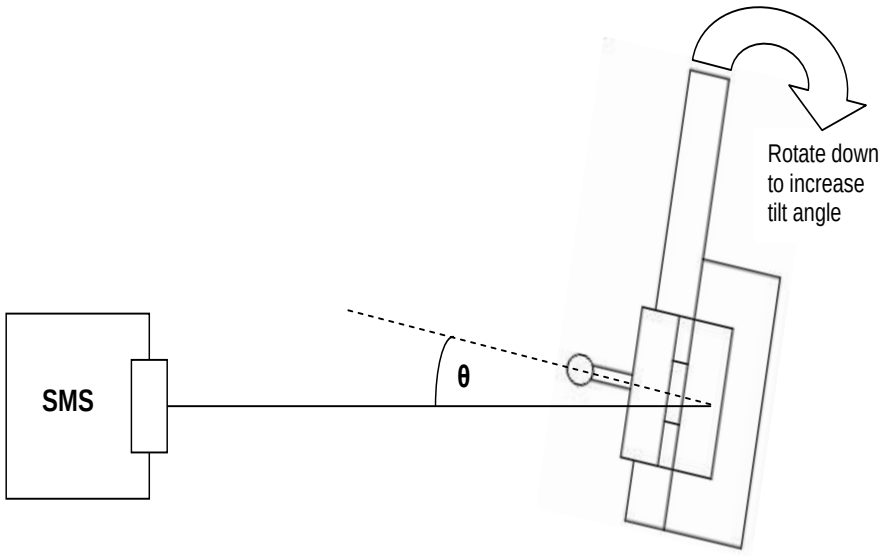

Figure 5-3: Schematic side view of the experimental setup showing the tilt angle, θ, used in the experiments. The tilted vice is rotated down around a pivot point approximately where the dotted line meets the horizontal solid line.

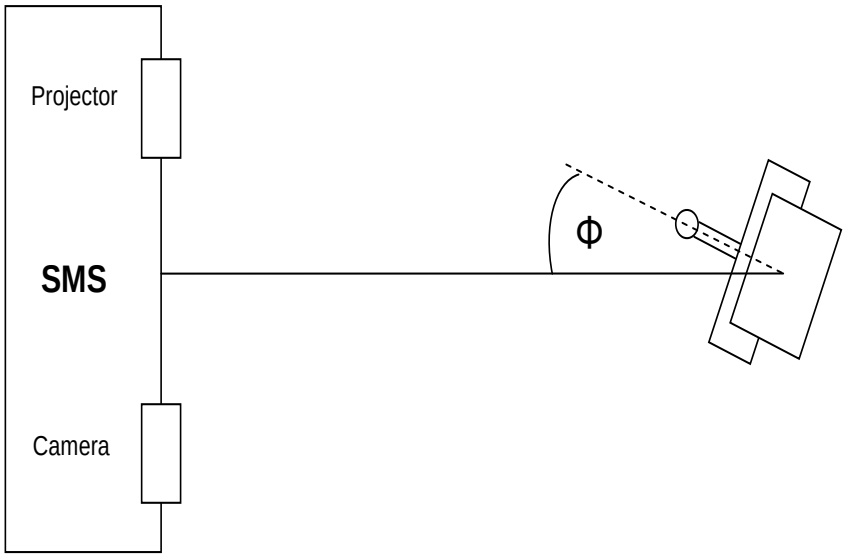

Figure 5-4: Schematic top view of the experimental setup showing the rotation angle, φ, used in the experiments. The tilted vice is rotated down a pivot point approximately where the dotted line meets the horizontal solid line.

(a)

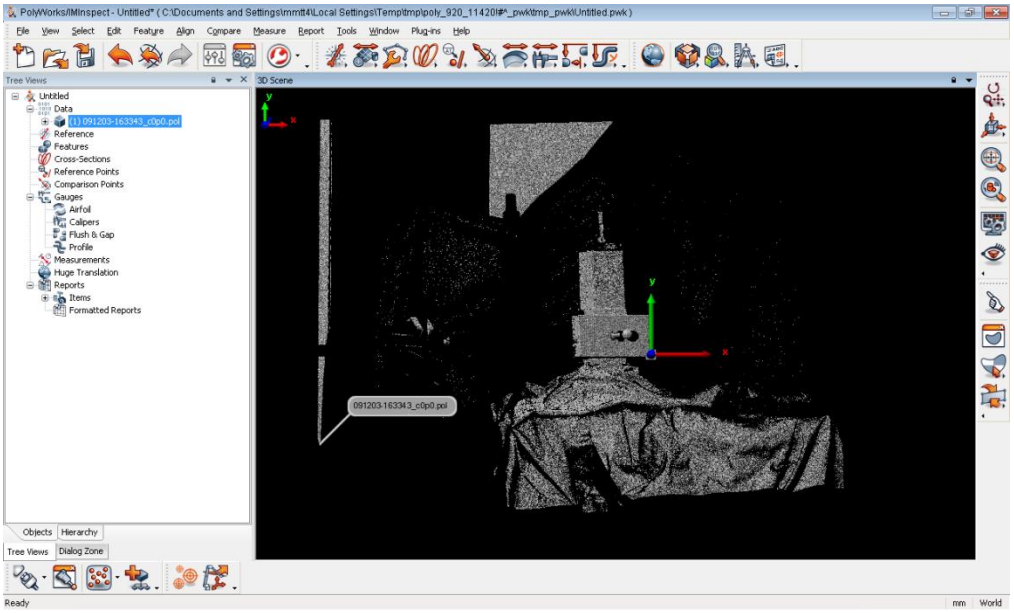

(b)

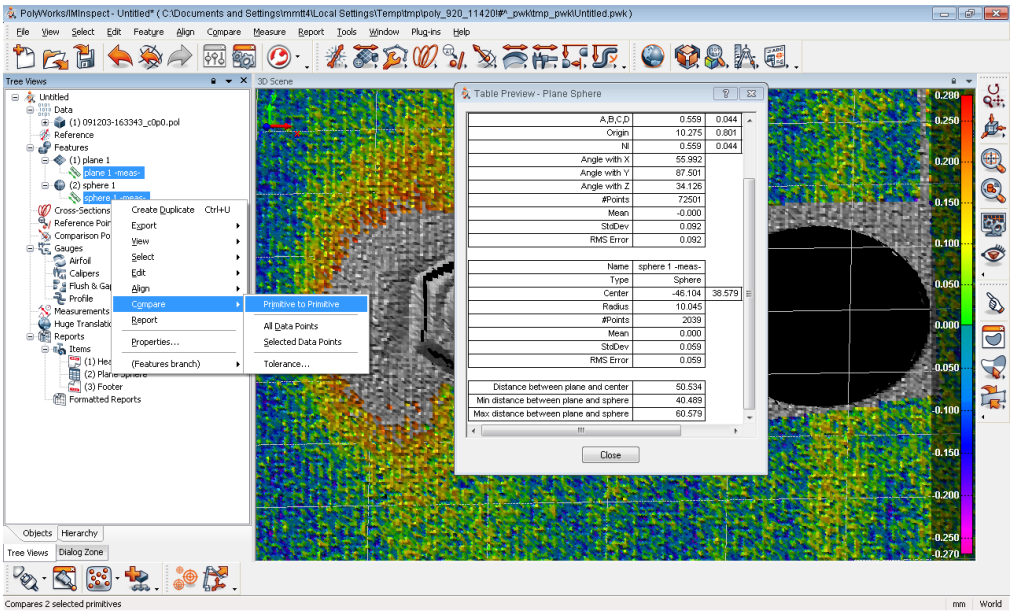

Figure 5-5: Two example screen shots showing a typical Polyworks analysis. (a) Original point cloud that is exported into Polyworks. (b) End results in a table from the user-selected point cloud data.

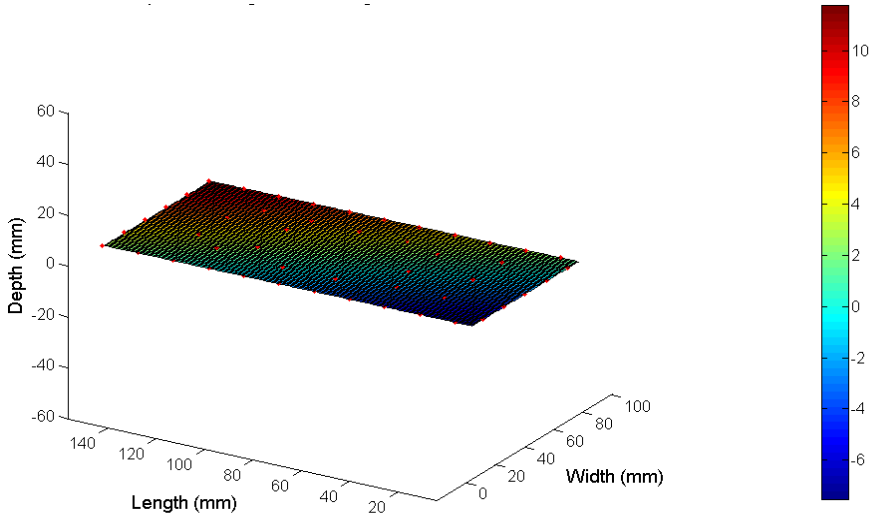

Figure 5-6: Points that were probed by the CMM on the surface of the plate (shown by the red dots) and the variation in the depth from the best-fit plane across the plate surface, indicated by the colour bar ($\times 10^{-6}$ mm).

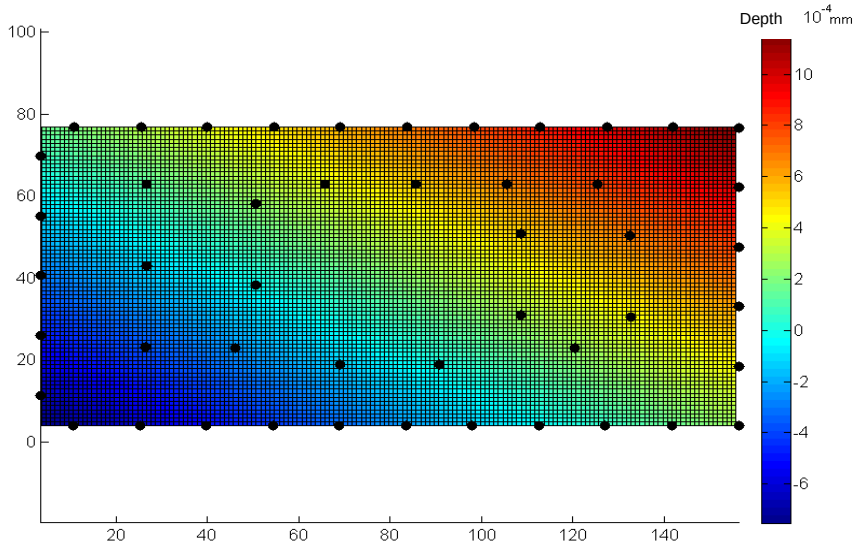

Figure 5-7: Top view of the points that were probed by the CMM on the surface of the plate (shown by the black dots) and the variation in the depth from the best-fit plane across the plate surface, indicated by the colour bar ($\times 10^{-4}$ mm).

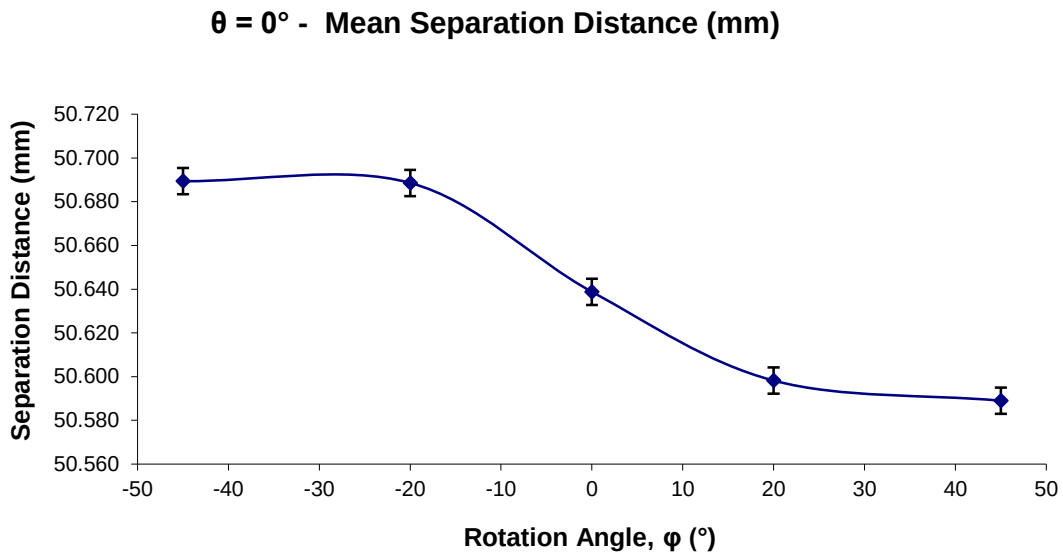

Figure 5-8: Mean separation distance of the sphere centre from the plane at the different rotation angles, φ (°). Error bars indicate variability between five repetitions of the Polyworks analysis.

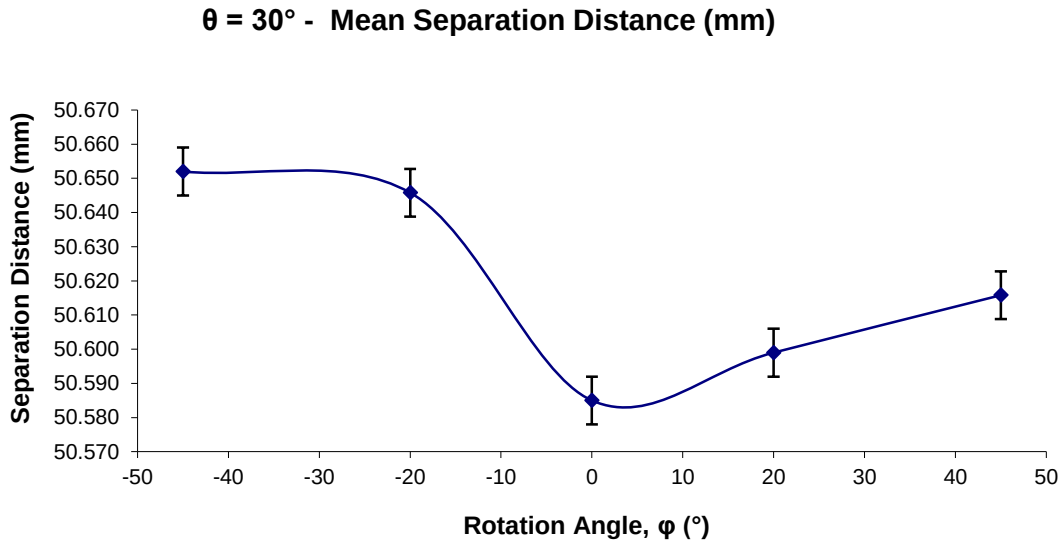

Figure 5-9: Mean separation distance of the sphere centre from the plane at the different rotation angles, φ (°). Error bars indicate variability between five repetitions of the Polyworks analysis.

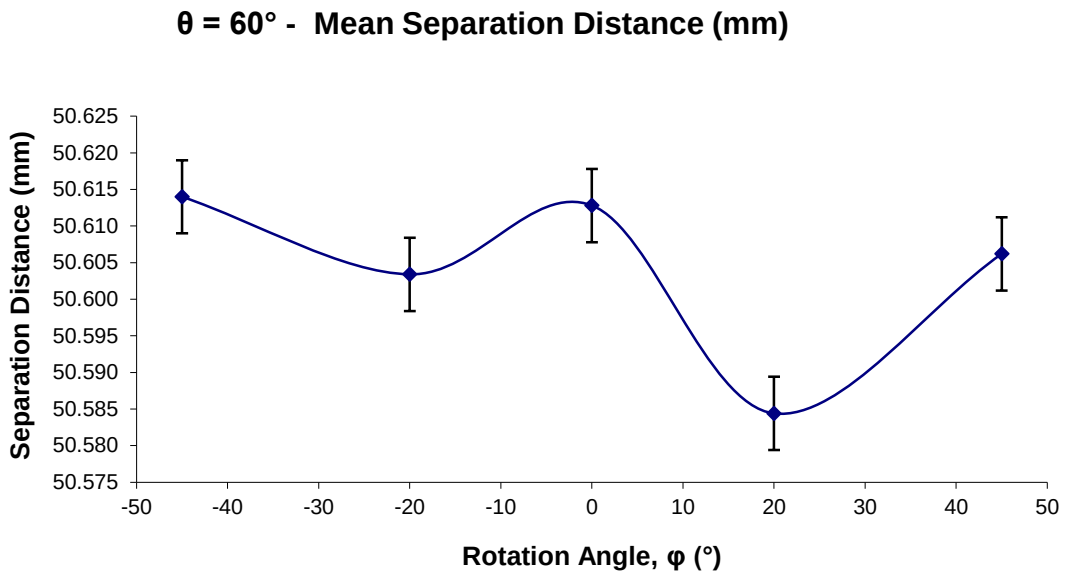

Figure 5-10: Mean separation distance of the sphere centre from the plane at the different rotation angles, φ (°). Error bars indicate variability between five repetitions of the Polyworks analysis.

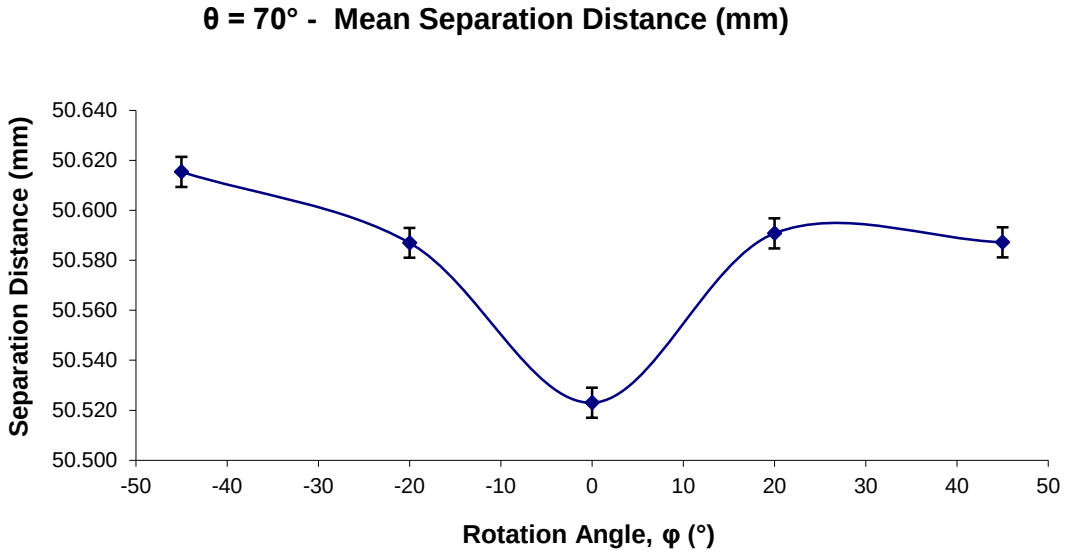

Figure 5-11: Mean separation distance of the sphere centre from the plane at the different rotation angles, φ (°). Error bars indicate variability between five repetitions of the Polyworks analysis.

Chapter 6

Implementation of calibration process

6.1. Introduction

The Phase Vision optical SMS has been through ~15 years of development; from initial laboratory prototypes (see Figure 6-1), to the commercialised SMS1200 DBE (also referred to as a 'scanner' and shown in Figure 6-2). Two of these SMS1200 DBE scanners were used in the implementation of the calibration process (as shown in Figure 6-3). The scanners were designed and manufactured to industry standards by the Phase Vision engineers; in each scanner, a high quality projector (Projection Design F22 SX+) and camera (Vosskuhler CCD4000) were installed. The server computer is also embedded within the carbon fibre reinforced plastic (CFRP) casing, between the nominal 1200 mm separation of the camera and projector. The CFRP casing's lay-up was designed to minimise the effects of thermal expansion. The computer performs the tasks of measurement acquisition control via a graphical user interface (GUI) and image processing of the acquired measurements from the camera-projector pairing of the scanner. In total, there were two combinations of camera-projector pairings used in acquiring the results for the calibration process, the camera-projector pairing for the first scanner, referred to as C_1P_1 or 'scanner one', and the camera-projector pairing for the second scanner, referred to as C_2P_2 or 'scanner two'.

The arrangement of the two scanners during implementation of the calibration process is shown in Figure 6-3 (Figures 6-4, 6-5 and 6-6 show alternative views of the setup and implementation). Each scanner is held in position and supported by two tripods bolted to the underside surface, thus providing the scanner stability when acquiring measurements. The compact and modular design of the scanners allows for this type of arrangement, in which all camera-projector pairs (C_1P_1 and C_2P_2 of scanner one and scanner two respectively) are aligned adjacent to one another. The corresponding measurement volume of each scanner as a result is independent and non-overlapping. The large volume calibration artefact is positioned across these measurement volumes

via the manufactured Stewart platform manipulator (described in Chapter 4). Each scanner has visibility of one part of the artefact. There is thus several reference points in each scanner's field of view (FOV), none of which are visible to the other scanner, but which can nevertheless be used as control points during the calibration process because of the known separations between all the reference spheres in the artefact. The manipulator is used to position the artefact so that there is an even distribution of these control points in each measurement volume, by positioning the artefact at different locations in the measurement volume.

In chapter 2 the calibration process based on a bundle adjustment algorithm was introduced. The two major phases, i.e. (1) initialisation and (2) refinement, along with the four corresponding sub-processes (1) shape data acquisition, (2) sensor parameter initialisation, (3) shape data post-processing and (4) bundle adjustment were explained. Shape data acquisition refers to measurements of the calibration artefact, and is performed during both the initialisation and refinement phases. The measurement data for all acquisitions is saved to disk, from where it can be read and used either to initialise or refine the calibration parameters.

The initialisation phase of the calibration process usually involves shape data acquisition and sensor parameter initialisation of the optical SMS. However, during the implementation of this calibration process, the sensor parameters were pre-defined through prior calibration of each optical SMS. This calibration was performed using a 2-D calibrated planar artefact consisting of circles on a plate, which were imaged, detected, and fitted by ellipse fitting the imaged circles (as a circle is a special case of an ellipse), through a calibration process developed by the Phase Vision engineers. For each of the two scanners, using each camera-projector pair, 12 poses of the planar artefact were measured (i.e. shape data acquisition at different orientations and locations in the measurement volume), from which estimates of the sensor parameters were computed from the DLT method (described in Chapter 2), then refined through control point selection and bundle adjustment. This then provided all the calibration parameters for each scanner, in each scanner's independent measurement volume (Figure 6-7).

The refinement phase of the calibration process comprised shape data acquisition, sensor parameter initialisation, shape data post-processing and bundle adjustment. During shape data acquisition, the large volume calibration artefact was measured by both scanners alternately, and the shape datasets saved to disk. The unwrapped phase maps, τ_x and τ_y respectively, contained within each shape dataset were then converted to point clouds. The spheres from the artefact were used as control points for estimating the artefact's pose; the sphere centre coordinates were estimated using Newton's method – modified according to the Levenberg and Marquardt algorithm [19], [55].

It should be noted that the calibration artefact's position and orientation in a local frame of reference was already pre-established by measurements taken on a large volume mechanical CMM (as described in Chapter 3). It is from this local reference frame along with the point cloud data that the transformation between the coordinates from the mechanical CMM and optical SMS were estimated (i.e., the artefact pose for both scanners). After this, the artefact pose parameters for the second scanner were registered into the coordinate system of the first scanner, the new sensor parameters for scanner two were then used by the 3-D DLT method, for verifying the sensor parameters of scanner two, in the coordinate system of scanner one.

Shape data post-processing then allowed the user to define the number of control points on each artefact feature in readiness for bundle adjustment, in every measurement pose, and save this information to disk. The control point information, estimated artefact poses and sensor parameters, for both scanners, were then used as initial estimates in the bundle adjustment. The bundle adjustment refined all the sensor parameters and the distortion parameters (collectively termed as the calibration parameters), in a non-linear optimisation (Figure 6-7). In the MATLAB code developed to implement the algorithm, a number of parameters were introduced that allowed user control of parameters such as the number of measurement poses used for calibration, the number of control points per artefact feature, and the threshold values for the phase error and modulation maps for selecting valid pixels in each measurement.

Ideally once the artefact poses and the internal sensor parameters have been estimated, the rest of the refinement phase should run automatically, as long as the user has defined the number of control points for bundle adjustment on each artefact feature (spheres in this case). The accuracy of the refined calibration parameters was thus strongly dependent on the acquisition of good shape data, and selecting control points that were positioned completely on the surface of the artefact features used for calibration. If unreliable shape data and/or rogue control points are present, the bundle adjustment will fail to reach its potential minimum value.

This is a particular issue with the connecting rod end pieces as it is difficult to ensure automatically that points from the end pieces are not included in the bundle adjustment. For this reason, for the experiments described here a user defined mask for each sphere surface was established manually and used to force the selection of the control points from the spheres' surfaces alone. Hence, if satisfactory convergence does not occur, either the bundle adjustment can be restarted by altering the user defined controls and/or the calibration parameters from the initial bundle adjustment can be re-processed in a subsequent loop of the bundle adjustment. An absolute minimum is reached for the initial input parameters when the bundle adjustment's objective function ceases to reduce further for multiple iterations (a threshold of ten iterations per μm of reduction was used), and also when the constituents of the objective function reach a level that is comparable to the expected system accuracy. This in combination advocates that an absolute minimum has been reached by the objective function rather than a local minimum.

In this chapter; the shape data acquisition process applied during the refinement phase of implementing the calibration process is further explained. The procedure for estimating the initial artefact poses from the transformation from the local coordinate system established by the mechanical CMM, to the global coordinate system of the optical SMSs, is explained in Section 6.2. Estimating the sensor parameters of scanner two in the coordinate system of scanner one is also described in Section 6.3. The process for selecting the pixels in image space used as control points of the artefact during refinement is presented in Section 6.4. The bundle adjustment in object space is

discussed in Section 6.5 in terms of the calibration parameters. The chapter concludes with discussions focussed on the results achieved from implementation of the calibration process, with particular attention drawn to the performance of the process, and the verification of the measurement accuracy of the refined calibration parameters.

6.2. Shape data acquisition

The shape data acquisition during refinement involved positioning the large volume calibration artefact across the two measurement volumes of the two respective scanners, and then taking measurements while maintaining visibility of the artefact features in each scanner's FOV. The calibration artefact was positioned across the measurement volumes, on the Stewart platform manipulator (described in Chapter 4). For each scanner the projector projected a sequence of fringe patterns, whilst the camera acquired the images of these patterns on the measured artefact. The output from each scanner included an intensity map for the horizontal and vertical fringes, phase gradient map for each fringe orientation, phase modulation and phase error maps (Figure 6-8).

It should be noted that the dimensions of the maps is equivalent to the dimensions of the camera. Hence, for a 2048 x 2048 pixel camera, each phase gradient map was a 2048 x 2048 matrix, and the corresponding point cloud was expressed as three 2048 x 2048 matrices for the respective *x*, *y*, *z* coordinates, along with an epsilon one error map. For all measurements the datasets were saved to disk; there were 12 maps for each pose, at 64 bytes per pixel, 16 Mb per map, and 192 Mb per pose. There were two SMSs and 12 poses per SMS, hence, 4.8 Gb of data in total.

6.2.1. Estimate artefact pose and ordering of coordinates

As stated in Chapter 2, the pose of an artefact is the transformation from the artefact's local coordinate system (established on a mechanical CMM) to the measurement volume's coordinate system (i.e. the world coordinate system of the optical SMS). This is described in terms of position and orientation by six parameters, t_x, t_y, t_z (constituents of a translation vector along the *x, y, z* axes), and the Euler angles, ω, ϕ, κ (rotations about the *x, y, z* axes). The parameters estimated were the rotation matrix, **R** (with the Euler angles ω, ϕ, κ extracted), and the translation vector, **T**, that describe the

transformation from the artefacts local coordinate system to the measurement volume's coordinate system. These parameters together provide the initial estimation of the large volume calibration artefact's pose for each scanner.

From the point clouds of each measurement; the sphere centre coordinates of the large volume calibration artefact were estimated using Newton's method – modified according to the Levenberg and Marquardt algorithm [19], [55]. This method was applied only in the regions of interest (ROI) manually selected by the user. In this way control could be maintained by the user by knowing that the algorithm was being applied to points corresponding only to the surfaces of the artefact spheres visible to the cameras. With this information, the transformation between the mechanical CMM and the optical SMS frames was then estimated for each of the poses, and for each scanner.

There exists a rigid body transformation between the two sets of 3-D coordinates, which can be estimated by the singular value decomposition technique (SVD). This technique has been shown to be both a reliable and numerically efficient way of calculating the transformation matrices for this type of problem [119]. The objective here is to find the transformation that minimises the sum *S* over *n* spheres by suitable choice of the variables **R** and **T** where:

$$S = \sum_{i=1}^{n} \|(\mathbf{R}\mathbf{A_i} + \mathbf{T}) - \mathbf{B_i}\|^2 \tag{6-1}$$

and where $\mathbf{A_i}$ = misaligned dataset,

$\mathbf{B_i}$ = reference dataset,

R = 3x3 rotation matrix, **T** = 3x1 translation vector.

The transformation is carried out by first calculating the zero mean matrices, $\bar{\mathbf{A}}_\mathbf{i}$ and $\bar{\mathbf{B}}_\mathbf{i}$ i.e. the deviations from the centroid for each dataset respectively:

$$\bar{\mathbf{A}}_\mathbf{i} = \mathbf{A_i} - \bar{\mathbf{A}} \tag{6-2}$$

$$\bar{\mathbf{B}}_\mathbf{i} = \mathbf{B}_\mathbf{i} - \bar{\mathbf{B}} \tag{6-3}$$

$$[\mathbf{u}, \mathbf{w}, \mathbf{v}] = SVD(\bar{\mathbf{B}}_\mathbf{i}\, \bar{\mathbf{A}}_\mathbf{i}^\mathbf{T}), \tag{6-4}$$

where $\bar{\mathbf{A}} = \frac{\sum_{i=1}^{n} \mathbf{A_i}}{n}$, the centroid of the misaligned dataset,

$\bar{\mathbf{B}} = \frac{\sum_{i=1}^{n} \mathbf{B_i}}{n}$, the centroid of the reference dataset,

SVD = singular value decomposition function,

u = 3x3 orthogonal matrix,

w = 3x3 diagonal matrix,

v = 3x3 orthogonal matrix.

The optimal rotation matrix, **R**, between **A** and **B** in the least squares sense is then

$$\mathbf{R} = \mathbf{u}\mathbf{v}^\mathbf{T}. \tag{6-5}$$

The corresponding optimal translation vector, **T**, is:

$$\mathbf{T} = \bar{\mathbf{B}} - \mathbf{R}\bar{\mathbf{A}}. \tag{6-6}$$

The associated values of $\bar{\mathbf{A}}_\mathbf{i}$, $\bar{\mathbf{B}}_\mathbf{i}$, **R** and **T** are then used as inputs to Eqn. (6-1) for all poses of each scanner in order to compute the minimised error between the two registered datasets. The transformed coordinates, $\mathbf{D_i}$, for a given pose are calculated by:

$$\mathbf{D_i} = \mathbf{R}\mathbf{A_i} + \mathbf{T}. \tag{6-7}$$

When the sphere centre coordinates are estimated by the Levenberg and Marquardt algorithm, the resulting list of coordinates is in arbitrary order, while the coordinates are specified in the coordinate system of the optical SMS. Before the above algorithm can be applied, it is therefore essential to label and identify all the estimated sphere centre locations so that they could be identified with those attributed to the large volume

calibration artefact. The sphere centre coordinates in the coordinate system of both scanners were labelled in the same manner as they were for the CMM measurements (i.e. spheres labelled from '1' to '15') and the ordering was done manually.

The manually selected ROI for each sphere was used to compute the visible sphere centre coordinates, in the coordinate system of the scanner that measured it. Provided at least three spheres were visible in the measurement volume for a given pose, these coordinates were then registered with those measured by the CMM using the SVD technique to calculate the rotation matrix, **R**, and translation vector, **T**. This was done for all the poses. These matrices were then saved to disk: one file containing the data for all the poses from scanner one, and one file containing the data for all the poses from scanner two. The transformed sphere centre coordinates were also saved to disk: one file containing the transformed visible sphere centre coordinates in the coordinate system of scanner one for all the poses, and one file containing the transformed visible sphere centre coordinates in the coordinate system of scanner two for all the poses.

6.3. Sensor parameter initialisation

The sensor parameters for the two scanners were known in their own respective coordinate systems from prior calibration. However, to calibrate the two scanners to bring their respective coordinate systems into a global coordinate system (i.e. one coordinate system identifiable to both scanners), the sensor parameters for scanner two were registered into the coordinate system of scanner one. This registration was once again carried out using the SVD technique (as described in section 6.2.1). Eqn. (6-7) was used to calculate the transformed visible sphere centre coordinates from scanner two into the coordinate system of scanner one. The equivalent visible sphere centre coordinates from the CMM measurements for scanner two were transformed into the coordinate system of scanner one, using scanner one's rotation matrix, **R**, and translation vector, **T**, previously established (and described in section 6.2.1).

The 3-D DLT method described in Chapter 2, which involves the minimisation of an algebraic error function, was then used for verifying the estimated new sensor parameters for scanner two (in scanner one's coordinate system). The 3-D DLT method

required the use of control points – at least six non-coplanar points that were well distributed in the sensor's FOV. These were provided by the registered 3-D sphere centre coordinates (48 in total), originally from scanner two's coordinate system but now in scanner one's coordinate system. The 3-D DLT between points (x_m, y_m, z_m) in object space and their corresponding image coordinates $\left(\xi_M^{(c)}, \eta_M^{(c)}\right)$ for scanner two is given by Eqns (2-11) and (2-12).

By rearranging Eqn. (2-12), **L** can be solved directly using Gaussian elimination, hence providing a solution in a least squares sense:

$$\mathbf{L} = \mathbf{M^{-1}} \begin{bmatrix} \xi_M^{(c)} \\ \eta_M^{(c)} \end{bmatrix}. \tag{6-8}$$

where **M** is defined in Eqn. (2-12). The minimised error over the set of points for scanner two in image space $\left(\xi_M^{(c)}, \eta_M^{(c)}\right)$ and object space (x_m, y_m, z_m), is calculated as:

$$\min_L \Sigma \left(\begin{bmatrix} \xi_M^{(c)} \\ \eta_M^{(c)} \end{bmatrix} - \mathbf{ML} \right)^2 \tag{6-9}$$

By solving the eleven DLT parameters for scanner two ($\mathbf{L}_{=1\ldots11}$) using Eqn. (6-8), the internal and external parameters can be calculated. The internal parameters are given by the Equations (2-13)-(2-17).

Three of the external parameters i.e. scanner two's sensor pinhole coordinates $\left(x_O^{(c)}, y_O^{(c)}, z_O^{(c)}\right)$ in the coordinate system of scanner one, can be calculated by Eqn. (2-18).

The remaining three external parameters i.e. the Euler angles are extracted from the 3x3 rotation matrix, **R**, the elements of which were retrieved by the following equations:

$$R_{31} = \frac{L_9}{P} \qquad R_{32} = \frac{L_{10}}{P} \qquad R_{33} = \frac{L_{11}}{P} \tag{6-10}$$

$$R_{11} = \frac{\xi_H^{(c)} R_{31} - \frac{L_1}{P}}{c_x} \qquad R_{12} = \frac{\xi_H^{(c)} R_{32} - \frac{L_2}{P}}{c_x} \qquad R_{13} = \frac{\xi_H^{(c)} R_{33} - \frac{L_3}{P}}{c_x} \tag{6-11}$$

$$R_{21} = \frac{\eta_H^{(c)} R_{31} - \frac{L_5}{P}}{c_y} \qquad R_{22} = \frac{\eta_H^{(c)} R_{32} - \frac{L_6}{P}}{c_y} \qquad R_{23} = \frac{\eta_H^{(c)} R_{33} - \frac{L_7}{P}}{c_y} \tag{6-12}$$

where $P = {L_9}^2 + {L_{10}}^2 + {L_{11}}^2$.

The Euler angles, ω, ϕ, κ can then be extracted from **R** [52]:

$$\phi = \sin^{-1} R_{31}, \qquad \omega = \cos^{-1} \frac{R_{33}}{\cos \phi}, \qquad \kappa = \cos^{-1} \frac{R_{11}}{\cos \phi} \tag{6-13}$$

With the Euler angles extracted, this then provided verified estimates of the full set of nine sensor parameters for scanner two (excluding distortion parameters) in scanner one's coordinate system. Hence, the estimates of the parameters of both scanners were now ready for refinement via bundle adjustment, the non-linear optimisation described in Section 6.5 that provided the full set of calibration parameters.

6.4. Control point selection for bundle adjustment

During the implementation of the calibration process, two types of control point coordinates are considered: known control points and calculated control points. Known control point coordinates are those established by an independent measurement system such as a mechanical CMM. Calculated control point coordinates are the coordinates of scattering points that lie on a 'control surface' and established by using the sensor parameters to project rays from image space of the camera and projector, to object space, as described in Section 2.3.3. Knowing that a scattering point lies on a control surface provides a useful constraint in the bundle adjustment, even though the exact coordinates of the point are unknown. The uncertainty surrounding where the scattering point lies is further minimised by allowing the user to manually select the ROI of a control surface. This method was used on the large volume calibration artefact, and allowed the pixel coordinates belonging to the spheres (i.e. the control surfaces) from the phase maps to be identified.

The number of control points used in the bundle adjustment directly affects the computation time in executing the bundle adjustment. Therefore, for optimum execution, the control points used consisted of points that were completely on the surface of the artefact's spheres, and distributed evenly across these respective surfaces. An algorithm developed by Ogundana in [19] was used for automatic selection of a given number of pixel coordinates for each visible sphere surface. The algorithm works on the principle that if a sphere from the large volume calibration artefact is fully visible to the optical SMS, it will produce an elliptical region of interest (ROI) in image space of the pixels that belong to the sphere. In this way, the number of control points selected would be evenly distributed (with the spacing between control points user defined) across the number of rows and columns of the pixels representing the sphere in image space. In the results presented in this chapter, a spacing of 10 pixels between control points was used.

6.5. Bundle adjustment in object space

In Chapter 2, the bundle adjustment used in the calibration process was described. The bundle adjustment model was expressed as an objective function, F, with two terms, ε_1, the sum of squares of errors between the rays projected from camera and projector

pinholes, and ε_2, the sum of squares of errors between the known and calculated control point coordinates. Calculating ε_1 indicates the level of quality of the calculated Cartesian coordinate at each pixel of the measured shape data i.e. the relevant phase gradient maps. The process for calculating ε_2 was dependent on the characterisation of the 3-D features which constituted the large volume calibration artefact.

As the large volume calibration artefact utilised spheres as features during the calibration process, when the bundle adjustment was applied, the rotation matrix, **R**, (computed from the Euler angles, ω, ϕ, κ), and the translation vector, **T**, from the artefact pose, was applied to the known control point coordinates, $\mathbf{s_{oi}}$, in order to register the control point coordinates in the global coordinate system of the measurement volumes. The 3-D coordinates of the pixels selected as control points, $\mathbf{s_{i,j}}$, on the sphere surfaces for bundle adjustment (as described in section 6.4), were calculated using the estimated sensor parameters to project rays from image space into object space.

For each respective sphere in a pose from the scanners, the relationship between the i^{th} point on the sphere surface and the corresponding sphere centre, $\mathbf{s_{oi}}$, was established by the known radius, r_i, of the sphere. The sphere centre coordinates were transformed into the global coordinate system thus:

$$\mathbf{s_{ti}} = \mathbf{R}\mathbf{s_{oi}} + \mathbf{T} \tag{6-14}$$

where $\mathbf{s_{ti}}$ is sphere centre coordinates in the global coordinate system.

The errors present in the initial estimates of the sensor parameters imply that the distance between a calculated control point on the sphere's surface, $\mathbf{s_{i,j}}$ (the 3-D Cartesian coordinates), and $\mathbf{s_{ti}}$ (the position vector of sphere centres determined from data from the optical SMS) would normally be different from r_i. The bundle adjustment therefore aimed to minimise this error, ε_2, which can be expressed as:

$$\varepsilon_{2,i,j} = \left|\mathbf{s_{i,j}} - \mathbf{s_{ti}}\right| - r_i \tag{6-15}$$

Between datasets acquired for the bundle adjustment, the large volume calibration artefact undergoes rigid body translation. This implies that the six pose parameters would be free to change during bundle adjustment for each scanner. Due to the physical setup of the scanners and the calibration artefact, constraints had to be applied to certain parameters, to ensure convergence of the bundle adjustment, and as a result, accurately refined calibration parameters. Parameters to which constraints were applied during bundle adjustment were referred to as 'fixed', whilst the parameters with no constraints were referred to as 'free'. The main fixed parameters were the pinhole locations and corresponding Euler angles for camera one i.e. six parameters in total. Parameters were declared 'fixed' or 'free' by the user by editing the *artefact definition* file which also contained the sphere centre coordinates of the large volume calibration artefact (as measured on the mechanical CMM).

6.6. Artefact definition

The 3-D coordinates of the 15 known sphere centre coordinates constituting the large volume calibration artefact were used as known control points during the calibration process. The location of the 15 sphere centre coordinates use sphere seven as the origin, with the *x*, *y*, *z* coordinates set to (0, 0, 0) in units of mm. These coordinate's (alongside the coordinates of the other 14 sphere centres), as well as the radius, *r*, of each sphere, were written to a text file known as the *artefact definition* file. The artefact definition file consisted of four rows and four columns per sphere, an example of which is shown below:

x	1	600	0
y	1	600	0
z	1	600	0
r	1	25	0

The first column was the description, and the second column a flag array indicating which parameters were fixed and which were set to free (a value of '0' means fixed, while a value of '1' means free). The third column was an array of the values linked to the description, and the fourth column reserved to allow the accuracy of the values in

the third column to be specified, although not used in the current Phase Vision software release. Hence, the artefact definition file for the large volume calibration artefact consisted of a 60 x 4 array (15 spheres with four rows per sphere). When estimating the artefact's pose during the shape data acquisition phase, the sphere centre coordinates saved in the artefact definition file were read from disk, and used for matching with the estimated sphere centre coordinates from the measured data throughout the calibration process, as described in previous sections.

6.7. Extensible markup language

Due to the nature of the initialisation and refinement processes of the optical SMS, it is good programming practice to keep the input data file containing information of the hardware and software parameters separate from the software code and the measurement output files. In the present optical SMS, the input data file associated with the optical SMS is saved in an extensible markup language (XML) document. Generally, an XML document is a well-structured text file that is put into a computer readable format, while still maintaining human readability [120]–[123].

The structure of an XML document is hierarchical, which can be broken down into several 'elements'. An element is representative of a logical component within the document, and can contain many different data types i.e. strings, integers, Boolean etc. The master element which contains all other elements is referred to as the *root* element, and the elements contained within elements are known as sub-elements. Sub-elements containing one or more sub-elements are called *branches*, whereas those not containing further sub-elements are called *leaves*.

To access the input XML document, an XML processor (or parser) was required. In this work, a third party XML processor developed in Java by jdom.org was used to parse XML documents into computer readable format [124]. This XML processor also provided the ability to read, write and transfer XML elements, and could also be called upon by other programming languages such as C++ and MATLAB.

6.8. Software structure

The software chosen to control the hardware of the optical SMS, the measurement procedure and the calibration process can have implications on overall system performance and implementation efficiency. The measurement acquisition procedure requires low-level and real-time communication between the hardware and software, and requires efficient management of large amounts of acquired data. Hence, the C/C++ programming language was used by the engineers at Phase Vision to develop the computationally rigorous shape data acquisition measurement system and graphical user interface (GUI). The prototype calibration process developed in this thesis, in contrast, can be utilised in a less intensive manner with relatively lower computational speed, and does not require real-time processing.

The calibration process can be performed offline (i.e., data processing after measurement acquisition is fully completed). MATLAB was selected as the main programming language for executing the calibration process. MATLAB is a high level programming language with many mathematical algorithms that are needed for the calibration process already built into the main language or available via toolboxes. The original bundle adjustment code was written in MATLAB, as was a wide variety of functions developed within Phase Vision to read and manipulate the experimental datasets.

During shape data acquisition, in the C/C++ measurement acquisition system, the XML input file is parsed for the controlling parameters, such as the phase shifting and phase unwrapping parameters, and then passed on to the measurement acquisition function. A seven-frame phase-stepping is used along with a ‘reverse exponential’ temporal phase unwrapping algorithm (TPUA). The TPUA involved decreasing the fringe density exponentially from the maximum of 64 fringes, i.e. $s = 64$, across the field-of-view. The fringe sequence was thus t = 64, 63, 62, 60, 56, 48 and 32 fringes (i.e. seven different fringe patterns, per fringe orientation, per frame). Therefore, a total of 7 x 7 = 49 vertical fringe patterns were projected, followed by 49 horizontal fringe patterns. These fringe patterns were recorded by the SMS’s camera and saved to disk, then inputted to the phase estimation function. This function returned three maps each for the vertical

and horizontal fringe patterns: one phase gradient map, one phase error map and one intensity modulation map, which were all saved to disk alongside the white-light texture image.

The two phase gradient maps were then utilised by the point cloud calculation function, which used a triangulation algorithm alongside the calibration parameters from the XML file, to produce a 3-D point cloud. The 3-D point cloud was saved to disk as three matrices corresponding to *x*, *y*, *z* coordinates of the respective points in the point cloud. An epsilon one error map was also saved. The phase gradient maps, phase error maps, intensity modulation maps, texture image, epsilon one error map and point cloud data for a completed measurement, comprised one dataset. Each dataset was saved in a time-stamped folder, named with the information of the date and time the measurement was acquired. All of this occurred as part of the standard measurement process. These datasets were then accessed by MATLAB in order to implement the calibration process.

6.9. Experimental results

6.9.1. Description of experiments

The experimental results discussed in this section were acquired using two SMS1200 DBE scanners, with each scanner consisting of one camera and one projector. Hence, there were two combinations of camera-projector pairings used in total, i.e. the camera-projector pairing for scanner one, referred to as C_1P_1, and the camera-projector pairing for scanner two, referred to as C_2P_2. The specification for the camera (Vosskuhler CCD4000) was M = 2048 pixels, N = 2048 pixels, ${N_x}^c = 15.1$ mm, ${N_y}^c = 15.1$ mm. The specification for the projector (Projection Design F22 SX+) was M = 1400 pixels, N = 1050 pixels, ${N_x}^c = 19.0$ mm, ${N_y}^c = 14.3$ mm.

The camera and projector for each scanner were aligned so that the measurement volume was within the respective FOV of the camera and projector. Both scanners were setup with a stand-off distance of approximately 2500 mm from the centre of the proposed measurement volume. The initial pinhole locations for the cameras and projectors within each scanner's measurement volume were obtained from independent prior calibration of each scanner using a planar artefact.

The planar artefact was a composite panel, aluminium skins on a honeycomb core, with an array of circles printed onto one skin. These circles were imaged, detected, and fitted by ellipse fitting the imaged circles (as a circle is a special case of an ellipse), through a calibration process developed by the Phase Vision engineers. For each of the two scanners, using each camera-projector pair, 12 poses of the planar artefact were measured (at different orientations and locations in the measurement volume), from which estimates of the sensor parameters were computed from the DLT method (described in Chapter 2), and refined through bundle adjustment. This then provided all the calibration parameters for each scanner, in each scanner's independent measurement volume.

The arrangement of the two scanners during implementation of the calibration process is shown in Figure 6-3. The compact and modular design of the scanners allowed them to be aligned next to one another. The corresponding measurement volume for each scanner was similarly aligned, where one scanner's measurement volume was independent from the other scanner, with no overlap between the two. The approximate measurement volume of each scanner was 850 mm (width) x 850 mm (height) x 1000 mm (depth). The focus of the projectors had to be set so that projected images were defocused within the measurement volumes [10], [18].

The large volume calibration artefact supported by the Stewart platform manipulator was placed towards the front of the two respective measurement volumes (~ 2000 mm stand-off distance), and measurements were taken by both scanners alternately. Subsequent measurements of the artefact were made at eleven different positions evenly distributed within the respective measurement volumes. The initial measured pose of the artefact allowed four spheres to be measured within each camera's FOV. The artefact was then translated in the x-axis for further measurements by approximately 100 mm and 200 mm from the initial position. These three measurements were then repeated at approximately the following stand-off distances from the scanners: 2330 mm, 2670 mm and 3000 mm. The acquired data from both scanners were saved to disk;

in total there were 24 measurements, twelve from each scanner. Offline calibration was then carried out using the measured datasets on a separate computer.

The following sub-section will focus on assessing the performance of the calibration process by comparing the values of specific quantities before and after calibration. These quantities include the objective function, F, and its two constituent terms, ε_1 and ε_2; the corresponding weightings for these terms were fixed as $\gamma_1 = \gamma_2 = 1$. The values of F, ε_1 and ε_2 quoted are the square root of their mean values as calculated over all control points used in the bundle adjustment. In total, the bundle adjustment optimised 14 calibration parameters for each for each camera and projector, i.e. 56 parameters in total (as there are two cameras and two projectors in total), six fixed parameters and 50 free parameters, with typical run times using approximately 13 000 control points of 300 s.

6.9.2. Calibration results using large volume calibration artefact

Results obtained from the calibration of a multi-sensor optical SMS (the two scanner setup shown in Figure 6-3) using the large volume calibration artefact are discussed in this section. The artefact was fully characterised using a large volume mechanical CMM. The results from this (described in Chapter 3) were used to set up the artefact definition file. The artefact was positioned across the measurement volume of both scanners via the manufactured Stewart platform manipulator. Each scanner had visibility of one end of the artefact, thus providing several reference points in each camera's FOV, which were then used as control points during the implementation of the calibration process. Very fine dusting of the spheres was also carried out using developer powder; a layer of approximately 5 µm was created, thus much smaller than the sensitivity of the sensors. This 5 µm value comes from the information supplied with the developer powder, which advises that a fine dusting of a surface will provide a coating of approximately 5 µm. This was done to reduce the specular component of the scattered light and also to reduce the effects of intensity gradients on the measurements (see Chapter 5).

The initial measured pose of the artefact was taken with it positioned approximately 2000 mm away from the scanners (plan view is shown in Figure 6-9), with visibility of four spheres in each camera's FOV. The artefact was then translated along the x-axis for

further measurements by approximately 100 mm and 200 mm from the initial position. These three measurements were then repeated at approximately the following stand-off distances from the scanners: 2330 mm, 2670 mm and 3000 mm. This gave twelve measurements in total for each scanner, with four visible spheres in each measurement, hence 96 spheres in total across the two scanners. The point cloud data from all these measurements was acquired using the calibration parameters of each scanner from prior calibration using the 2-D planar artefact.

For all 96 measured spheres in total, regions of interest (ROI) were manually selected and the pose of the artefact was estimated for each scanner. The rotation matrix, **R**, Euler angles, ω, ϕ, κ, translation vector, **T**, and the sphere centres coordinates calculated for scanner one are shown in Table 6-1, Table 6-2 and Table 6-3 respectively. The corresponding quantities for scanner two are shown in Table 6-4, Table 6-5 and Table 6-6 respectively. There were 13604 calculated control point coordinates selected in total for the bundle adjustment process, with each control point corresponding to a scattering point on the surface of any one of the 96 spheres.

For the bundle adjustment process: the values corresponding to the respective camera and projector calibration parameters for both scanners, both before and after bundle adjustment, are shown in Table 6-7 and Table 6-8 respectively. Figure 6-10 shows a histogram of values for ε_1 calculated using both the estimated sensor parameters and the refined calibration parameters. The histogram of the estimated sensor parameters has a range of ε_1 errors, ±1 mm, as distortion isn't taken into account and the parameters have not yet been refined. However, the histogram of the refined calibration parameters has a smaller range as the parameters have been fully optimised and include distortion; the majority (i.e. approximately 95%) of the refined ε_1 errors are within ±90 μm.

Figure 6-11 shows a histogram of the values for ε_2 calculated using both the estimated sensor parameters and the refined calibration parameters. The histogram of the estimated sensor parameters has range of ε_2 errors, ±1.7 mm, as distortion is not taken into account and the parameters haven't yet been refined. However, the histogram of the refined calibration parameters has a smaller range as the parameters have been fully

optimised and include distortion; the majority (i.e. approximately 95%) of the refined ε_2 errors are within ±0.17 mm.

The square root of the mean value of the objective function, *F*, reduced from 2.2 mm to 98 µm. The ε_1 term reduced from 1 mm to 45 µm, whilst the ε_2 term reduced from 2 mm to 87 µm. Therefore, for the global measurement volume of 2.5 x 1 x 1 m^3 (i.e. the maximum approximate size of the combined measurement volumes of scanner one and scanner two), the figure of 87 µm for the ε_2 value represents an accuracy of approximately one part in 17 000 of the measurement volume diagonal with 95% confidence (k = 1.96).

6.9.3. Verification of calibration accuracy

To verify the calibration accuracy, measurements were taken of a Phase Vision carbon fibre ball-bar reference artefact. These measurements were taken after the XML input file was updated with the newly refined calibration parameters for both scanners, so that the output data from both scanners were now in a combined global coordinate system. The ball-bar consisted of two 50.850 mm diameter tungsten carbide spheres, and the average distance between the centres of the two spheres was 1015.650 mm ± 0.4 µm as obtained (and stated on the calibration certificate) from three repeat measurements by the Metris LK Ultra CMM. Following the guidance in VDI/VDE 2634, in total there were nine poses measured of this artefact, with one of the spheres always visible to scanner one, whilst the other sphere was always visible to scanner two. Post-processing of the 3-D point clouds was done via MATLAB, where for each point cloud, a manually selected region of interest was created to identify each sphere so that a sphere fitting algorithm could be used, in order to calculate the sphere centre coordinates using Newton's method modified according to the Levenberg and Marquardt algorithm [55].

The results that were obtained for all the verification poses are shown in Table 6-9: the sphere centre coordinates of the spheres visible to both scanners are calculated in the global coordinate system. The average separation distance between sphere centres, for all nine poses of the ball-bar artefact was 1015.612 mm ± 0.03 mm, a difference of 38 µm between the mechanical CMM measurements and those made using the optical

SMSs. However, in accordance with VDI/VDE 2634, the maximum deviation between the mechanical CMM measurements and those made using the optical SMSs was 149 µm. This represents an accuracy of approximately one part in 19 000 of the measurement volume diagonal. None of the deviations exceed the accuracy of the calibration; hence, verification of the calibration can be accepted.

6.10. Summary

The calibration process has been described in terms of the four sub-processes: shape data acquisition, sensor parameter initialisation, shape data post-processing, and bundle adjustment. Prior calibration of each of the two optical SMSs using the Phase Vision 2-D planar artefact consisting of ellipses meant that point clouds could be generated from the shape data acquired from each scanner in the multi-sensor setup shown in Figure 6-3. From the generated point clouds, user defined ROI were manually selected, to provide information for estimating the pose of the large volume calibration artefact. The artefact pose is the transformation from the artefact's local coordinate system (established on a mechanical CMM) to the measurement volume's coordinate system (i.e. the world coordinate system of the optical SMS). This is described in terms of position and orientation by six parameters, t_x, t_y, t_z (constituents of a translation vector along the *x*, *y*, *z* axes), and the Euler angles, ω, ϕ, κ (rotations about the *x*, *y*, *z* axes).

In order to align scanner two's coordinate system with scanner one, the spheres visible to scanner two were registered into the coordinate system of scanner one using the SVD technique. The estimated pose parameters of scanner one alongside the CMM measurements of the spheres visible to scanner two were used to generate the visible sphere centre coordinates of scanner two, in the coordinate system of scanner one. These newly generated sphere centre coordinates along with the corresponding image plane coordinates of scanner two were then used by the 3-D DLT method to generate both the external and internal sensor parameters of scanner two, in scanner one's coordinate system.

In addition, an algorithm developed by Ogundana in [19] was then used for automatic and uniform selection of pixels corresponding to scattering points on the surface of the

measured spheres. The estimated pose and sensor parameters were then refined by the bundle adjustment process through a non-linear optimisation. The physical setup of the sensors and the geometry of the large volume calibration artefact require constraints to be introduced during bundle adjustment. The external parameters of one of the sensors should be fixed, so that during bundle adjustment the global coordinate system remains fixed too. The setting up of constraints and the geometric properties of the artefact (i.e. control point coordinates) are done within the artefact definition file. It is from this file that the coordinates of the control points are read during the calibration process, and used when estimating the pose of the artefact.

The calibration process was used to calibrate a multi-sensor optical SMS with non-overlapping measurement volumes, consisting of two scanners aligned adjacently, each with one camera and one projector (the experimental setup used is shown in Figure 6-3). A measurement volume of 2.5 x 1 x 1 m^3 was calibrated using information from the large volume calibration artefact. The calibration was carried out offline. These datasets were then utilised by the calibration software for later processing and calculating the calibration parameters.

The artefact was positioned across the measurement volume of both scanners via the manufactured Stewart platform manipulator. Each scanner had visibility of one end of the artefact, thus providing several reference points in each camera's FOV, which were later used as control points during the implementation of the calibration process. The initial measured pose of the artefact allowed four spheres to be measured within each camera's FOV. The artefact was then translated in the x-axis for further measurements by approximately 100 mm and 200 mm from the initial position. These three measurements were then repeated at approximately the following stand-off distances from the scanners: 2330 mm, 2670 mm and 3000 mm. This gave twelve measurements altogether for each scanner, with four visible spheres in each measurement, hence 96 spheres in total across the two scanners. It took approximately two hours to capture all of the measurement poses.

Using this measurement data for the large volume calibration artefact, results show a significant reduction in the value of the two contributing terms of the objective function. It took approximately two further hours to complete the sensor parameter initialisation, shape data post-processing and bundle adjustment phases, hence, in total it took approximately four hours to complete the full calibration process. The ε_1 term reduced from 1 mm to 45 µm, whilst the ε_2 term reduced from 2 mm to 87 µm. With respect to the global measurement volume (i.e. the combined measurement volumes of scanner one and scanner two), the refined value of ε_2 value represented an accuracy of approximately one part in 17 000 of the measurement volume diagonal with 95% confidence (k = 1.96).

This figure was representative of what was achieved using the Phase Vision carbon fibre ball-bar reference artefact when verifying the calibration accuracy following the guidance in VDI/VDE 2634. The maximum deviation between the mechanical CMM measurements and those made using the optical SMSs was 149 µm. The maximum deviation represented an accuracy of approximately one part in 19 000 of the measurement volume diagonal. Hence, none of the deviations exceeded the calibration accuracy; hence, verification of the calibration could be accepted. This proved that the large volume calibration artefact was capable of calibrating a multi-sensor optical SMS setup with non-overlapping measurement volumes.

6.11. Tables

Pose	Translation Vector (mm)			Euler Angles (radians)		
	t_{x_1}	t_{y_1}	t_{z_1}	ω_1	ϕ_1	κ_1
1	200.048	-94.194	-457.934	-1.570	-0.0013	1.646
2	176.679	-94.657	-464.667	-1.570	-0.0013	1.657
3	297.172	-94.626	-432.991	-1.569	-0.0002	1.630
4	194.665	-93.419	-538.509	-1.570	-0.0013	1.647
5	153.851	-93.771	-536.388	-1.570	-0.0015	1.643
6	285.116	-94.088	-502.204	-1.570	0.0000	1.624
7	176.009	-90.661	-724.069	-1.569	-0.0012	1.631
8	66.728	-91.425	-719.376	-1.569	-0.0015	1.631
9	250.087	-90.161	-692.939	-1.569	-0.0008	1.617
10	93.863	-88.251	-904.556	-1.569	-0.0014	1.659
11	-9.333	-89.770	-892.113	-1.569	-0.0014	1.656
12	202.099	-87.465	-884.060	-1.568	-0.0007	1.637

Table 6-1: Estimated pose parameters for all poses of the large volume calibration artefact, as measured by scanner one.

Rotation Matrix		
-0.075	-0.997	-0.001
0.001	-0.001	1.000
-0.997	0.075	0.001

Table 6-2: Rotation matrix for scanner one calculated using the SVD technique.

Pose	Visible Sphere	Sphere Centre Coordinates (mm)		
		X	Y	Z
1	5	-265.224	-266.493	-122.150
	6	-241.360	252.471	177.264
	8	224.966	423.598	-159.616
	9	245.299	-95.708	140.247
2	5	-284.704	-266.946	-123.546
	6	-257.419	252.079	175.506
	8	204.992	423.135	-166.676
	9	228.793	-96.079	132.931
3	5	-173.679	-266.591	-104.936
	6	-154.146	252.131	195.159
	8	317.788	423.029	-134.067
	9	332.670	-96.588	165.902
4	5	-270.377	-265.747	-202.426
	6	-246.276	253.178	97.014
	8	219.766	424.309	-240.109
	9	240.331	-95.013	59.635
5	5	-312.382	-266.217	-202.034
	6	-289.534	252.713	97.517
	8	177.758	423.923	-237.849
	9	197.263	-95.369	61.883
6	5	-187.811	-265.877	-177.039
	6	-170.000	252.929	123.033
	8	303.954	423.620	-203.267
	9	316.931	-95.899	96.907
7	5	-294.119	-263.131	-395.237
	6	-274.583	255.628	-95.171
	8	196.580	426.858	-424.987
	9	212.507	-92.613	-125.324
8	5	-403.350	-264.062	-390.577
	6	-384.038	254.759	-90.524
	8	87.132	426.094	-420.310
	9	103.082	-93.261	-120.683
9	5	-224.643	-262.569	-370.752
	6	-209.068	256.054	-70.223
	8	266.691	427.294	-393.447
	9	278.283	-92.414	-93.690
10	5	-366.966	-260.922	-562.919
	6	-339.281	257.827	-263.405
	8	122.533	429.200	-606.045
	9	146.841	-90.263	-307.063
11	5	-471.188	-262.436	-551.874
	6	-444.472	256.331	-252.327
	8	18.438	427.688	-593.520
	9	41.719	-91.736	-294.509
12	5	-266.310	-259.977	-552.779
	6	-244.874	258.548	-252.466
	8	224.515	429.851	-584.697
	9	241.914	-89.945	-285.504

Table 6-3: Estimated visible sphere centre coordinates of scanner one.

Pose	Translation Vector (mm)			Euler Angles (radians)		
	t_{x_2}	t_{y_2}	t_{z_2}	ω_2	ϕ_2	κ_2
1	1675.549	-84.059	-451.066	-1.544	-0.003	1.557
2	1652.830	-84.267	-459.949	-1.544	-0.003	1.569
3	1770.116	-85.221	-417.150	-1.543	-0.002	1.541
4	1677.217	-81.358	-532.061	-1.544	-0.003	1.558
5	1636.303	-81.739	-533.852	-1.544	-0.003	1.554
6	1764.145	-82.954	-487.554	-1.544	-0.002	1.535
7	1674.809	-73.971	-719.436	-1.544	-0.003	1.543
8	1565.547	-74.698	-725.039	-1.544	-0.003	1.543
9	1745.795	-74.278	-681.788	-1.543	-0.003	1.529
10	1608.785	-66.924	-907.185	-1.544	-0.003	1.570
11	1504.767	-68.578	-904.857	-1.543	-0.003	1.567
12	1714.699	-66.654	-877.172	-1.543	-0.003	1.548

Table 6-4: Estimated pose parameters for all poses of the large volume calibration artefact, as measured by scanner two.

Rotation Matrix		
0.014	-1.000	-0.003
0.027	-0.003	1.000
-1.000	-0.014	0.027

Table 6-5: Rotation matrix for scanner two calculated using the SVD technique.

Pose	Visible Sphere	Sphere Centre Coordinates (mm)		
		X	Y	Z
1	11	-284.183	429.482	-160.807
	12	-289.273	-100.358	120.367
	14	204.234	-268.178	-176.965
	15	202.879	243.726	136.187
2	11	-303.594	428.570	-147.109
	12	-305.294	-101.236	134.065
	14	184.865	-268.933	-168.904
	15	186.879	243.031	144.182
3	11	-193.345	431.083	-158.777
	12	-203.763	-98.973	122.072
	14	294.171	-267.258	-167.390
	15	288.523	244.337	146.243
4	11	-282.283	432.220	-240.414
	12	-287.174	-97.651	40.829
	14	206.084	-265.460	-256.936
	15	204.960	246.451	56.299
5	11	-324.277	431.626	-249.265
	12	-330.204	-98.285	31.860
	14	164.232	-266.056	-264.125
	15	161.859	245.903	49.137
6	11	-200.654	434.150	-241.270
	12	-212.982	-95.857	39.712
	14	286.642	-264.391	-246.755
	15	279.285	247.304	66.791
7	11	-288.640	440.325	-457.400
	12	-298.054	-89.725	-176.319
	14	199.603	-257.578	-466.828
	15	193.886	254.202	-153.276
8	11	-398.075	438.782	-463.026
	12	-407.435	-91.249	-182.096
	14	90.464	-258.949	-472.524
	15	84.417	252.918	-159.070
9	11	-220.721	441.306	-446.621
	12	-234.360	-88.937	-165.909
	14	267.052	-256.899	-449.698
	15	257.494	254.631	-135.824
10	11	-347.182	445.308	-590.967
	12	-348.342	-84.767	-309.709
	14	141.373	-252.103	-613.926
	15	143.682	259.688	-300.342
11	11	-451.961	443.569	-593.964
	12	-454.171	-86.448	-313.052
	14	36.570	-253.783	-615.792
	15	37.885	258.046	-302.286
12	11	-247.092	447.767	-603.615
	12	-255.061	-82.575	-322.799
	14	240.885	-250.161	-616.436
	15	237.070	261.276	-302.257

Table 6-6: Estimated visible sphere centre coordinates of scanner two.

Calibration Parameters	Large Volume Calibration Artefact			
	Estimated Sensor Parameters			
	C_1	P_1	C_2	P_2
x (mm)	490.729	-358.630	-696.342	-1558.521
y (mm)	-287.066	-290.442	-219.798	-222.864
z (mm)	2615.312	2571.045	2740.811	2750.443
ω (radians)	-3.007	-3.036	-3.031	-3.058
ϕ (radians)	-0.174	0.137	-0.271	0.051
κ (radians)	3.135	-3.136	-3.138	-3.127
η_H (mm)	0.316	-0.209	0.316	-0.209
ζ_H (mm)	-0.569	1.006	-0.569	1.006
c (mm)	52.711	39.154	52.711	39.154
k_1 (mm^{-2})	-	-	-	-
k_2 (mm^{-4})	-	-	-	-
k_3 (mm^{-6})	-	-	-	-
p_1 (mm^{-1})	-	-	-	-
p_2 (mm^{-1})	-	-	-	-

Table 6-7: Estimated sensor parameters calculated using 3-D DLT.

Calibration Parameters	Large Volume Calibration Artefact			
	Refined Calibration Parameters			
	C_1	**P_1**	**C_2**	**P_2**
x (mm)	694.018	-219.316	-709.085	-1561.272
y (mm)	-211.648	-219.217	-219.568	-221.517
z (mm)	2585.780	2641.695	2702.901	2726.917
ω (radians)	-3.037	-3.037	-3.038	-3.067
ϕ (radians)	-0.264	0.099	-0.263	0.057
κ (radians)	3.139	-3.130	-3.138	-3.126
η_H (mm)	0.291	0.671	0.267	0.085
ξ_H (mm)	-0.060	0.421	-0.083	1.190
c (mm)	52.701	39.216	52.635	39.013
k_1 (mm^{-2})	-2.74×10^{-5}	-4.06×10^{-5}	5.50×10^{-5}	-6.58×10^{-5}
k_2 (mm^{-4})	1.11×10^{-7}	-3.90×10^{-7}	-1.19×10^{-7}	5.01×10^{-7}
k_3 (mm^{-6})	-1.04×10^{-9}	4.38×10^{-9}	3.81×10^{-9}	-2.47×10^{-9}
p_1 (mm^{-1})	-3.04×10^{-5}	-9.12×10^{-6}	5.62×10^{-5}	6.33×10^{-5}
p_2 (mm^{-1})	1.46×10^{-5}	9.03×10^{-5}	3.20×10^{-5}	4.46×10^{-5}

Table 6-8: Refined calibration parameters after bundle adjustment.

Pose	Scanner One Sphere Centre Coordinates (mm)			Scanner Two Sphere Centre Coordinates (mm)			Separation between Sphere Centres (mm)
	x	y	z	x	y	z	
1	-222.431	138.883	10.469	-1230.853	146.667	130.272	1015.543
2	-373.461	319.337	41.003	-1299.201	-90.879	119.205	1015.573
3	-250.490	152.276	-176.651	-1261.874	138.293	-84.801	1015.643
4	-345.090	-39.821	-403.436	-1177.710	299.526	68.874	1015.622
5	-481.773	364.310	-314.524	-1238.523	-178.348	90.677	1015.547
6	-311.708	172.645	-146.882	-1322.336	115.277	-228.252	1015.520
7	-289.590	147.740	-308.303	-1301.571	144.533	-221.624	1015.692
8	-541.012	143.835	-348.546	-1549.532	143.163	-227.152	1015.799
9	-110.591	153.182	-351.609	-1122.377	147.401	-264.213	1015.570
				Mean Separation between Sphere Centres (mm)			1015.612

Table 6-9: Sphere centre coordinates of the carbon fibre ball-bar in the global coordinate system. These measurements were taken to verify the accuracy of the calibration.

6.12. Figures

Figure 6-1: Initial prototype optical SMS developed by Coggrave in 2001 [10].

Figure 6-2: Latest SMS1200 DBE scanner, of which two were used in this work.

Figure 6-3: Experimental setup during implementation of the calibration process.

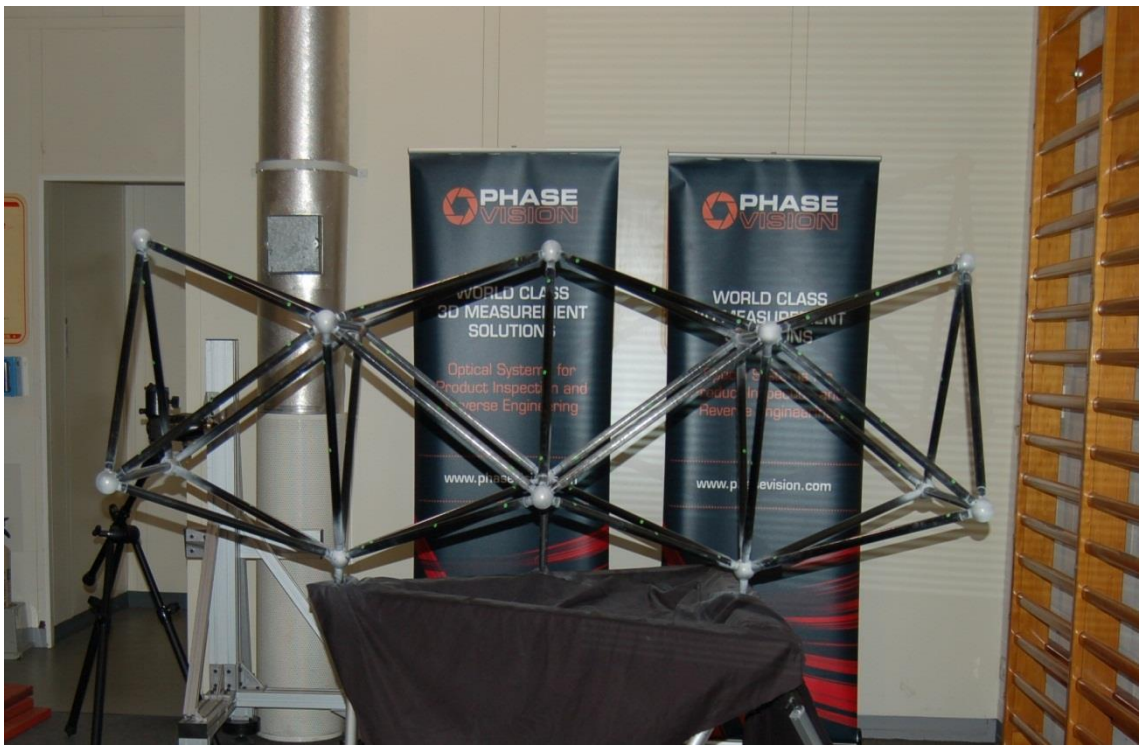

Figure 6-4: View of large volume calibration artefact from behind the optical SMSs.

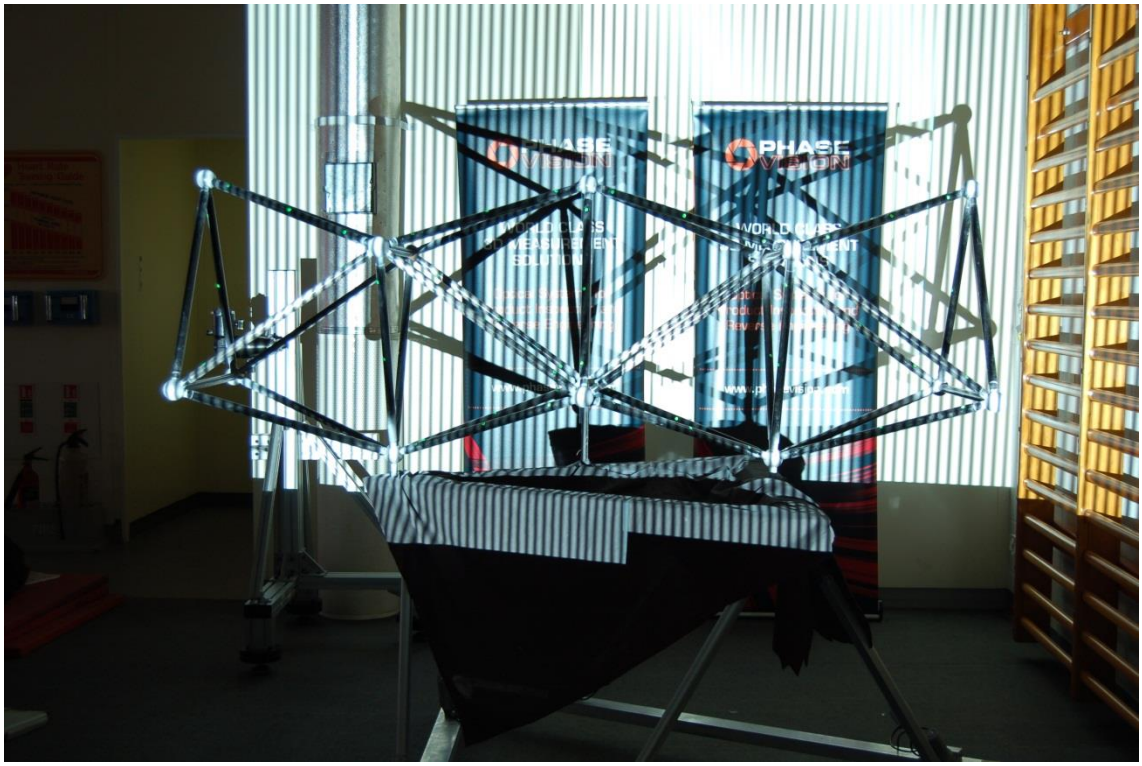

Figure 6-5: Vertical fringe patterns being projected during measurement acquisition.

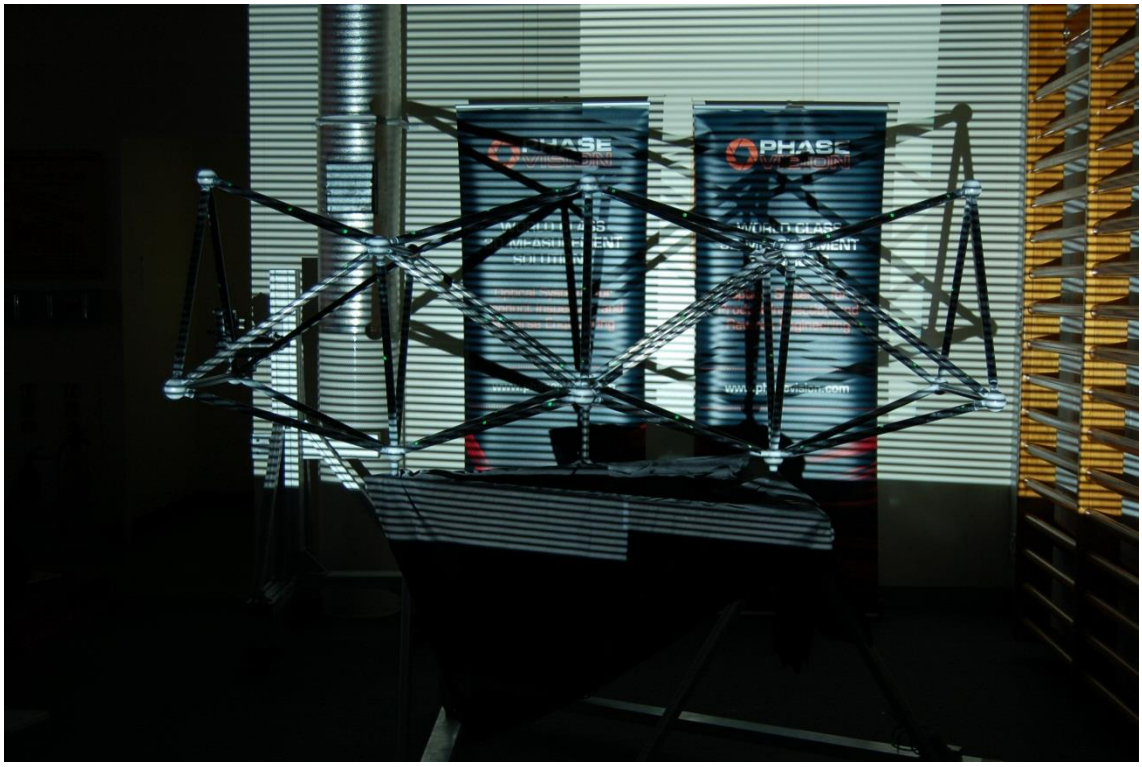

Figure 6-6: Horizontal fringe patterns being projected during measurement acquisition.

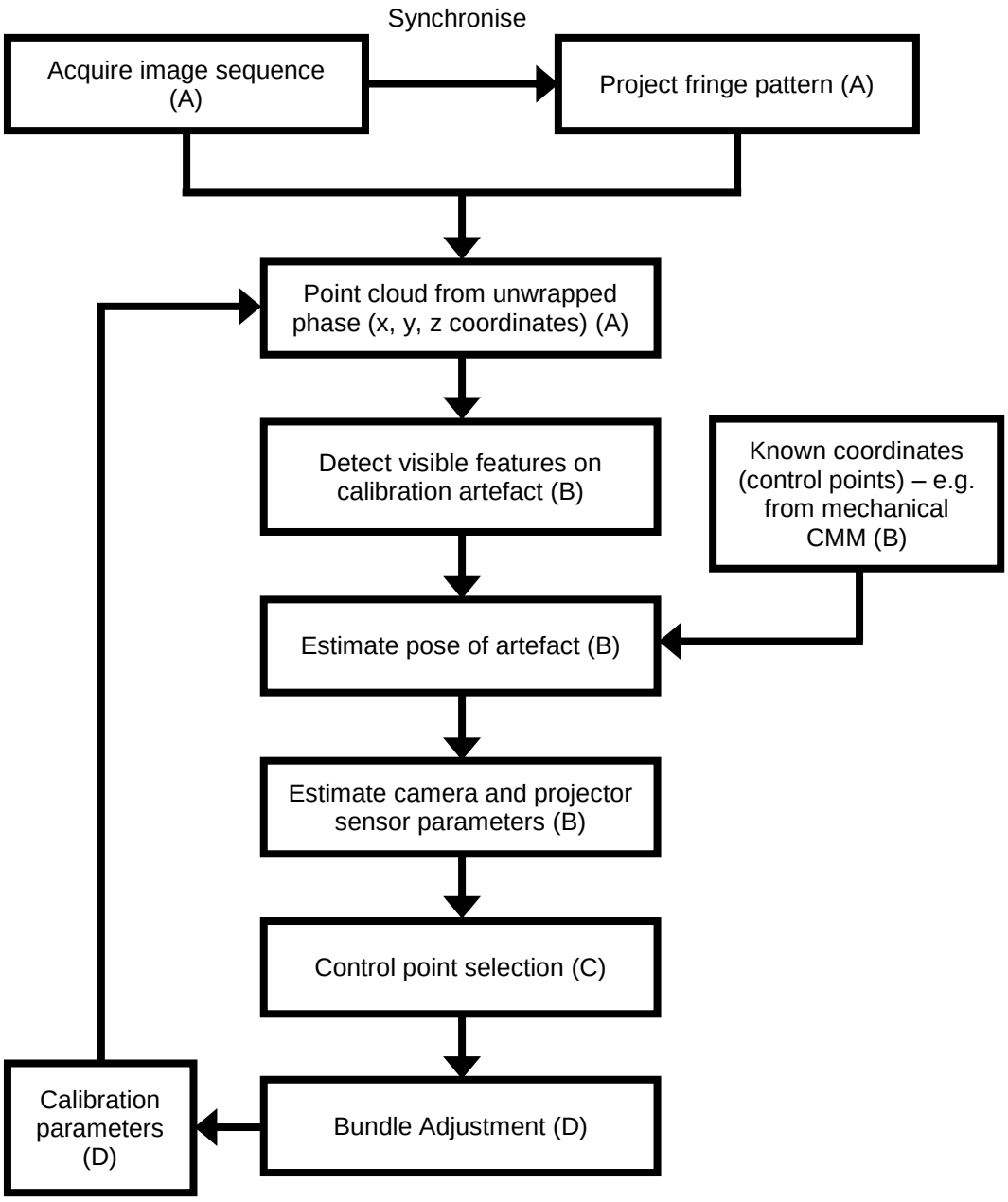

Figure 6-7: Initialisation and refinement phases of the calibration process both follow the same sequence: the initialisation phase refers to calibration performed on each individual SMS, with its independent measurement volume. Whereas the refinement phase refers to calibration performed for allowing the two independent measurement volumes to be combined into one global coordinate system. The letters A, B, C, and D denote the four sub-processes: shape data acquisition (A), sensor parameter initialisation (B), shape data post-processing (C), and bundle adjustment (D).

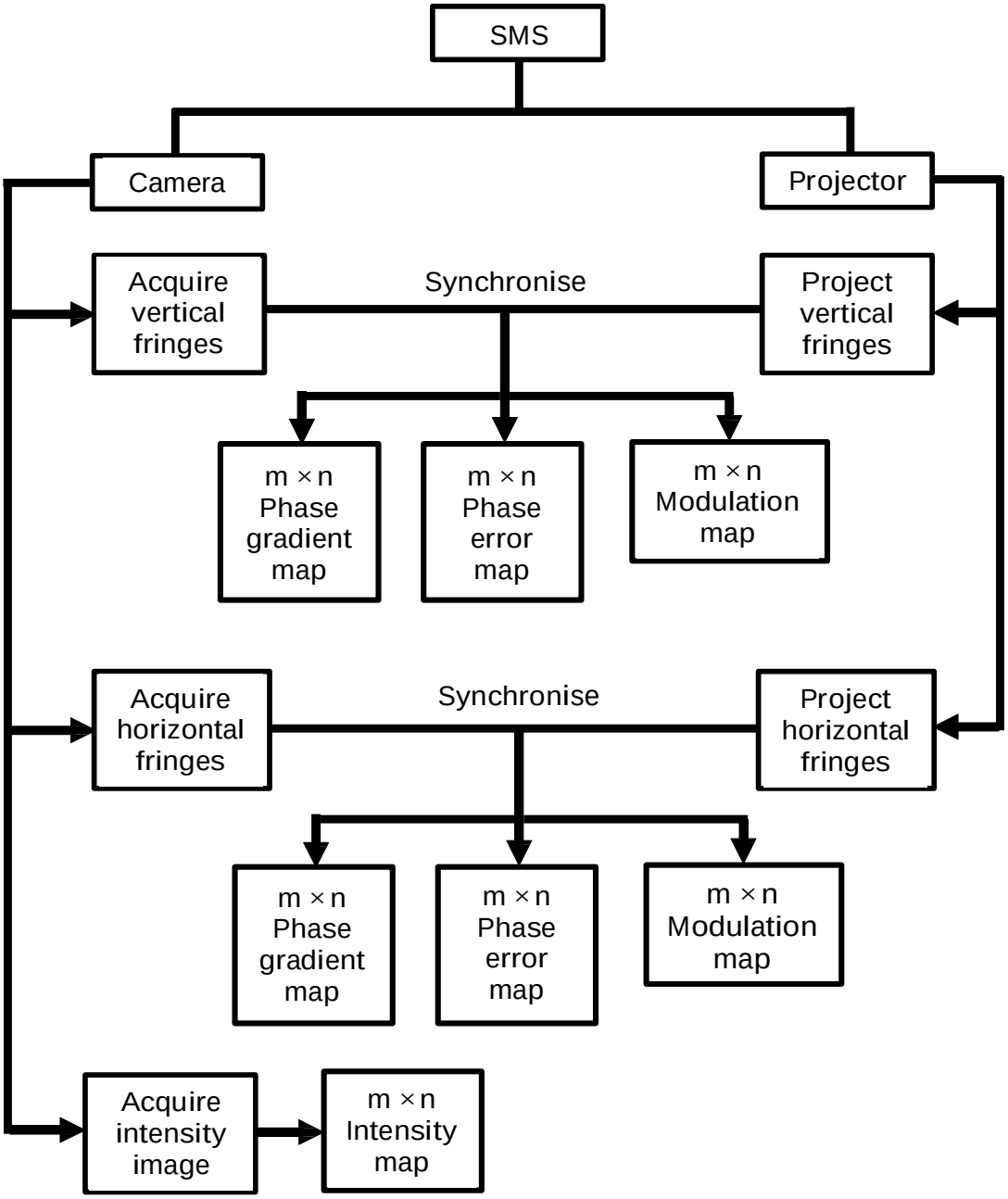

Figure 6-8: Process of shape data acquisition.

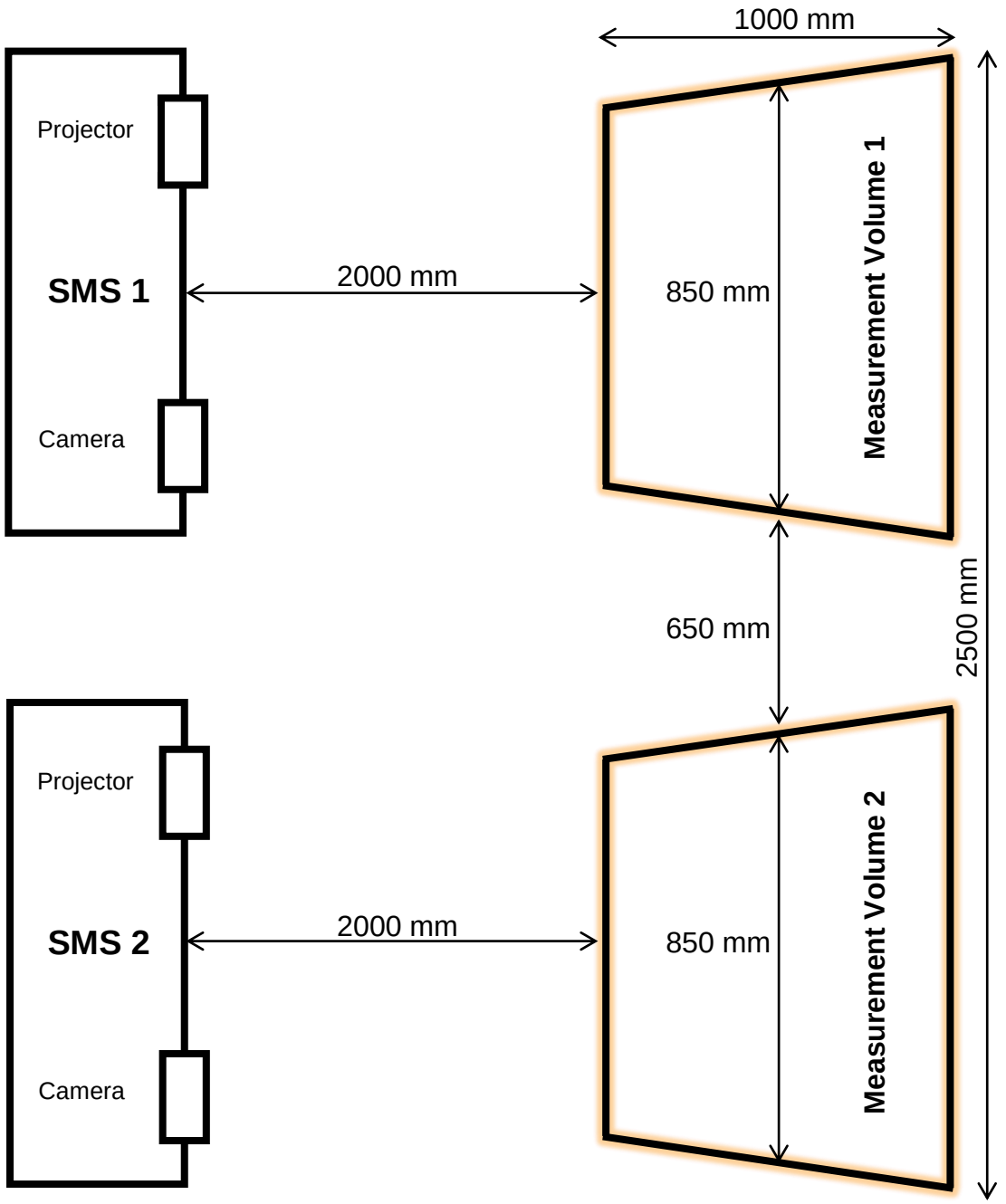

Figure 6-9: Plan view of the measurement volumes for each respective SMS, along with the approximate dimensions of the setup used during calibration. Calibration was performed to allow the two independent measurement volumes to be combined into one global coordinate system.

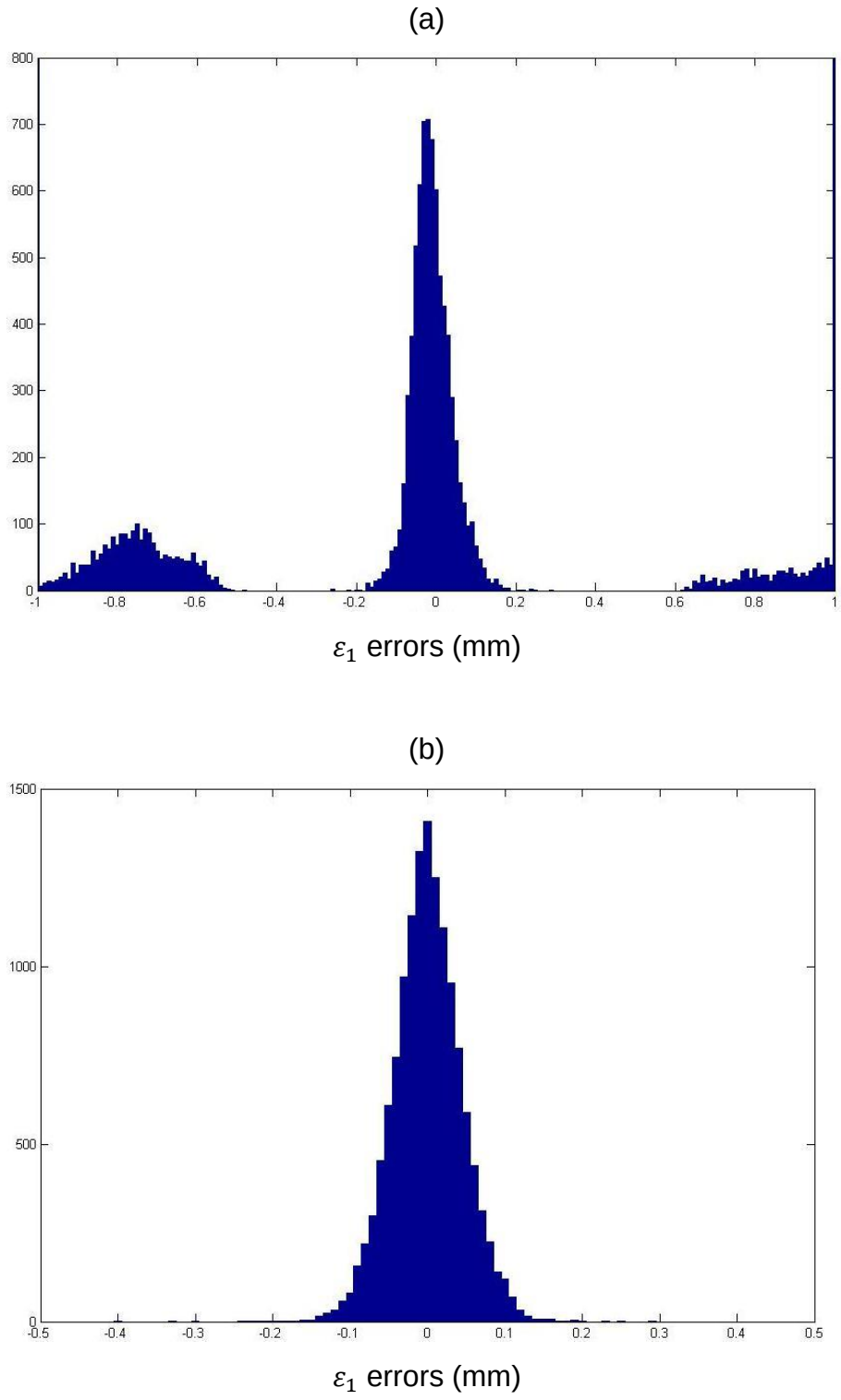

Figure 6-10: Histogram of 100 bins for ε_1 values of valid pixels calculated using the calibration parameters for both scanners across all poses of the large volume calibration artefact. The vertical axis represents the number of votes in each bin. (a) Histogram with values calculated using initial sensor parameters of both scanners. (b) Histogram with values calculated using refined calibration parameters.

(a)

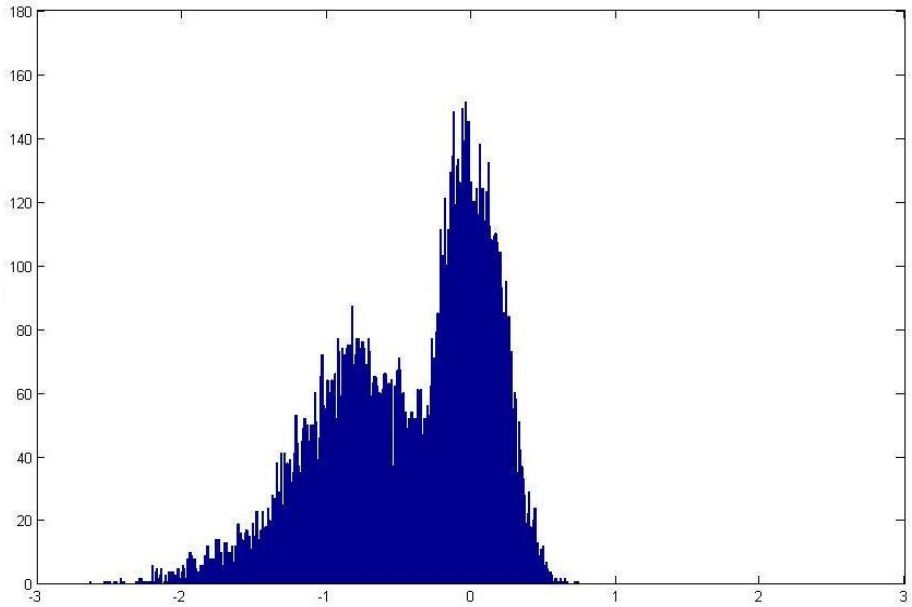

ε_2 errors (mm)

(b)

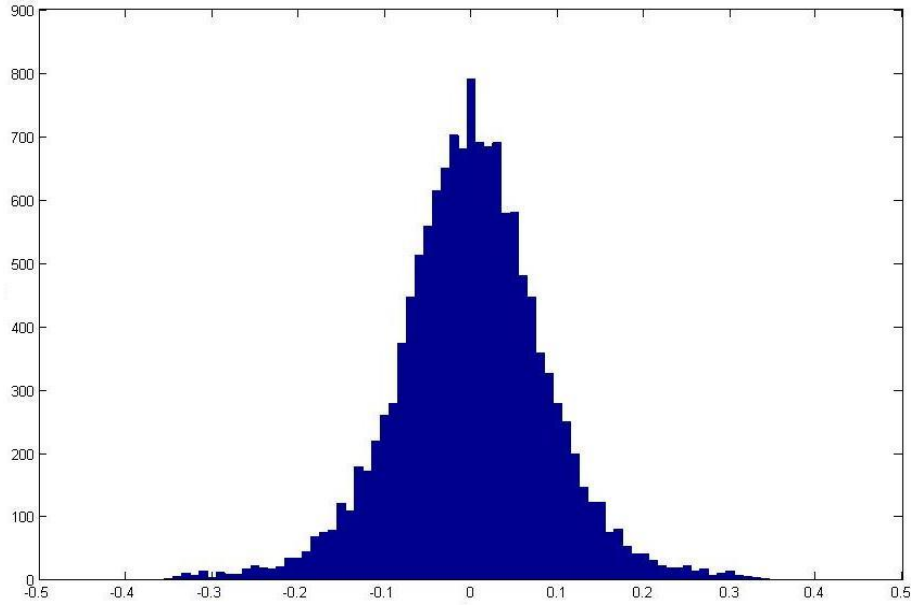

ε_2 errors (mm)

Figure 6-11: Histogram of 100 bins for ε_2 values of valid pixels calculated using the calibration parameters for both scanners across all poses of the large volume calibration artefact. The vertical axis represents the number of votes in each bin. (a) Histogram with values calculated using initial sensor parameters of both scanners. (b) Histogram with values calculated using refined calibration parameters.

Chapter 7

Conclusions

Shape measurement of 3-D objects using optical methods has developed rapidly over the last ten to twenty years [11]. An optical shape measurement system (SMS) based on the principle of fringe projection has been developed at Loughborough University and commercialised by its spin-out company Phase Vision Ltd. In this optical SMS, horizontal and vertical sinusoidal fringe patterns, with time varying fringe pitch and phase shifting, are computer generated. A spatial light modulator (SLM) inside a data projector is used to project these fringes on to a surface of an object which is to be measured. An off-axis digital camera, located a fixed distance from the projector is used simultaneously to capture the images of the fringe patterns in real time.

The temporal changes in phase of the fringes, seen at each image pixel of the camera, are used to deduce the 3-D coordinates of the scattering points on a measured object's surface. The phase gradients from the changes in phase are estimated explicitly by a temporal phase unwrapping technique. A pair of phase gradients is estimated for each pixel of the camera that together defines the location of a point in the image plane of the projector. The 3-D coordinates of the scattering point are then determined using a triangulation algorithm by calculating the midpoint of the closest points of approach between a ray from the camera pixel with the corresponding projector ray.

The calibration process for the optical SMS based on a photogrammetric approach combined with the fringe projection technique was initially developed by Ogundana [19]. This process was further enhanced in this work so that it could be used for linking and calibrating the non-overlapping measurement volumes of multiple independent optical SMSs. Although the approach was demonstrated here with two scanners, it can be extended to arbitrarily large numbers of devices. These measurement volumes were calibrated into one global measurement volume and coordinate system. Hence, the work described in this thesis has been focussed on addressing the issues involved in achieving

this objective, and the conclusions of the main findings of the thesis are discussed as follows.

The calibration method used in this work was based on a photogrammetric approach where quantifiable parameters were used to describe the sensor geometries. Control points on the surface of a calibration artefact, which had been independently measured using a mechanical coordinate measuring machine (CMM), were used to obtain the calibration parameters. The calibration parameters for both the camera(s) and projector(s) include sensor external, internal and lens distortion parameters, as well as the rigid body translation and rotation parameters that define the poses of the calibration artefact. The calibration process combined the advantages of fringe projection, i.e. high coordinate throughput and high spatial sampling rate, and photogrammetry i.e. robust and accurate calibration.

The calibration process can be broken down into two major phases: (1) initialisation, where acquired shape data of a 2-D calibration artefact is used to initialise sensor parameters, and (2) refinement, where acquired shape data of multiple poses of a calibration artefact are used in a bundle adjustment process i.e. the refinement of the calibration parameters in a non-linear optimisation. For the initialisation phase a 2-D planar artefact consisting of ellipses developed by Phase Vision was used for estimating the sensor parameters of each optical SMS. The main novel features presented in this thesis concerned the refinement phase in which a process has been developed to allow the creation of a larger global measurement volume from the setup of two or more adjacent SMSs with non-overlapping local measurement volumes.

In order to achieve this goal a new 3-D large volume calibration artefact, together with suitable means to move the artefact within the measurement volume, were designed and manufactured. This artefact was built from high strength carbon fibre tubing, chrome steel spheres, and mild steel artefact supports and end caps containing rare earth rod magnets. The major advantage of using the larger calibration artefact over the previously used ball-bar artefact was that it provided a dimensionally stable relationship between multiple features spanning multiple individual measurement volumes, thereby allowing calibration of several such scanners within a global coordinate system even

when they have non-overlapping fields of view. The calibration artefact is modular, providing the scalability needed to address still larger measurement volumes and volumes of different geometries. Both it and the translation stage are also easy to transport and to assemble on site. The artefact also carried forward the benefits of the previously used ball-bar artefact, in that it provided traceabitity for calibration through independent measurements on a mechanical CMM.

To ensure the artefact was suitable for its intended purpose, a structural analysis was performed so that the forces and displacements present due to gravity on the artefact structure could be modelled. As the calibration process was to be implemented in well controlled laboratory conditions, an analysis of the dynamic response of the artefact was not of primary concern. However, as these systems are designed to be used in industrial environments, future calibrations maybe performed in less well controlled environments. In this scenario it would be beneficial to perform a dynamic analysis of the artefact to verify that resonance of the artefact does not displace the spheres beyond the static structural analysis.

This structural analysis model was used to validate the integrity of the materials used to manufacture the artefact. The materials used were thoroughly tested for their thermal and hygroscopic behaviours. An inherently simple and robust method was used to quantify the thermal effects, in which a support tube ball-bar enclosed in a chamber was heated and then measured as it cooled on a mechanical CMM. The observed changes in length between sphere centres was then recorded, from which the magnitude of the thermal effects could defined and subsequently compensated for if necessary. The structural analysis shows that the artefact in its current design has the capability to be extended by up to 1 m. This is possible by using the same magnets but changing in combination features such as the separation between sphere centres and by changing the positioning of the three supports of the artefact. More support tubes could also be added to extend the volume, but to do this the strength of the magnets used would have to be amplified to overcome the tensile forces that would exist with such a structure.

An experimental study was carried out to observe the moisture absorption in carbon fibre tube samples at two different levels of relative humidity. The mass uptake in moisture was observed, from which the diffusion coefficients were calculated using Fick's second law of diffusion. The length change that was observed on the sample at 75% relative humidity (RH) was smaller than the measurement uncertainty of the mechanical CMM used to observe it (i.e. less than 1 μm). Hence, an estimate of the worst case was used to determine the strain, and along with the mass uptake data, was used to determine the coefficient of moisture expansion. This value was found to be comparable with other similar studies done previously on carbon fibre, and was found to have negligible dimensional effect on the materials.

During implementation of the calibration process using the large volume calibration artefact, the artefact was supported by a specially designed and manufactured Stewart platform manipulator, which was used to position the artefact at different locations across the measurement volumes of the two optical SMSs. The initial measured pose of the artefact was taken with it positioned approximately at the front of the measurement volumes, with visibility of four spheres in each camera's field-of-view (FOV). Twelve measurements in total for each SMS were captured, with four visible spheres in each measurement, hence 96 spheres in total across both SMSs.

A procedure was developed to align one SMS's coordinate system with the other, in order to link them both into one global coordinate system. The sphere centre coordinates from acquired shape data by the second SMS were registered into the coordinate system of the first SMS, using the singular value decomposition (SVD) technique. These registered sphere centre coordinates along with their corresponding image plane coordinates were then used by the 3-D DLT method to generate estimates of both the external and internal sensor parameters of the second SMS, in the coordinate system of the first SMS. The estimated artefact pose and sensor parameters were then refined by the bundle adjustment process through a non-linear optimisation. Implementing this calibration process produced an accuracy of the order one part in 17 000 of the global measurement volume diagonal.

This figure was representative of what was achieved using the Phase Vision carbon fibre ball-bar reference artefact when verifying the calibration accuracy following the guidance in VDI/VDE 2634. The maximum deviation between the mechanical CMM measurements and those made using the optical SMSs was 149 µm. The maximum deviation represented an accuracy of approximately one part in 19 000 of the measurement volume diagonal. Hence, none of the deviations exceeded the calibration accuracy; hence, verification of the calibration could be accepted. This proved that the large volume calibration artefact was capable of calibrating a multi-sensor optical SMS setup with non-overlapping measurement volumes.

References

[1] G. M. S. de Silva, *Basic metrology for ISO 9000 certification*. A Butterworth-Heinemann Title, 2002.

[2] J. S. Wilson, S. Ball, C. Huddleston, E. Ramsden, and D. Ibrahim, *Test and Measurement: Know It All: Know It All*. Newnes, 2008.

[3] S. K. Kimothi, *The Uncertainty of Measurements: Physical and Chemical Metrology : Impact and Analysis*. Asq Press, 2002.

[4] A.M.Badadhe, *Metrology And Quality Control*. Technical Publications, 2006.

[5] P. P. L. Regtien, "Metrology as part and parcel of training programmes for science and engineering," *Measurement Science Review. Section 1: Theoretical problems of measurement*, 2007.

[6] P. Sydenham, N. H. Hancock, and R. Thorn, *Introduction to measurement science and engineering*, New edition. Wiley-Blackwell, 1992.

[7] C.-H. Menq, H.-T. Yau, and G.-Y. Lai, "Automated precision measurement of surface profile in CAD-directed inspection," *IEEE Transactions on Robotics and Automation*, vol. 8, no. 2, pp. 268 –278, Apr. 1992.

[8] T. Proulx, *Optical Measurements, Modeling, and Metrology, Volume 5: Proceedings of the 2011 Annual Conference on Experimental and Applied Mechanics*. Springer, 2011.

[9] R. Sirohi, *Optical Methods of Measurement: Wholefield Techniques, Second Edition*. CRC Press, 2010.

[10] C. R. Coggrave, "Temporal phase unwrapping: development and application of real-time systems for surface profile and surface displacement measurement," 2001.

[11] J. M. Huntley, "Optical shape measurement technology: past, present, and future," in *Society of Photo-Optical Instrumentation Engineers (SPIE) Conference Series*, 2000, vol. 4076, pp. 162–173.

[12] F. Chen, G. M. Brown, and M. Song, "Overview of three-dimensional shape measurement using optical methods," *Opt. Eng*, vol. 39, no. 1, pp. 10–22, Jan. 2000.

[13] H. O. Saldner and J. M. Huntley, "Temporal phase unwrapping: application to surface profiling of discontinuous objects," *Appl. Opt.*, vol. 36, no. 13, pp. 2770–2775, May 1997.

[14] H. O. Saldner and J. M. Huntley, "Profilometry using temporal phase unwrapping and a spatial light modulator-based fringe projector," *Opt. Eng*, vol. 36, no. 2, pp. 610–615, Feb. 1997.

[15] J. M. Huntley and H. O. Saldner, "Shape measurement by temporal phase unwrapping: comparison of unwrapping algorithms," *Measurement Science and Technology*, vol. 8, no. 9, pp. 986–992, Sep. 1997.

[16] J. M. Huntley and H. O. Saldner, "Error-reduction methods for shape measurement by temporal phase unwrapping," *J. Opt. Soc. Am. A*, vol. 14, no. 12, pp. 3188–3196, Dec. 1997.

[17] C. R. Coggrave and J. M. Huntley, "High-speed surface profilometer based on a spatial light modulator and pipeline image processor," *Opt. Eng*, vol. 38, no. 9, pp. 1573–1581, Sep. 1999.

[18] J. M. Huntley and C. R. Coggrave, "Optimization of a shape measurement system based on spatial light modulators," pp. 104–114, Sep. 1999.

[19] O. O. Ogundana, "Automated calibration of multi-sensor optical shape measurement system," PhD thesis, Loughborough University, 2007.

[20] W. Schreiber and G. Notni, "Theory and arrangements of self-calibrating whole-body three-dimensional measurement systems using fringe projection technique," *Opt. Eng*, vol. 39, no. 1, pp. 159–169, Jan. 2000.

[21] D. Flack and J. Hannaford, *Fundamental good practice in dimensional metrology - measurement good practice guide no. 80. : Publications : National Physical Laboratory*. 2006.

[22] L. Kirkup and B. Frenkel, *An Introduction to Uncertainty in Measurement*. Cambridge University Press, 2006.

[23] S. G. Rabinovich, *Measurement Errors and Uncertainties: Theory and Practice*. Springer, 2006.

[24] M. Grabe, *Measurement Uncertainties in Science and Technology*. Springer, 2005.

[25] S. V. Gupta, *Measurement Uncertainties: Physical Parameters and Calibration of Instruments*. Springer, 2012.

[26] R. H. Dieck, *Measurement Uncertainty: Methods and Applications*. ISA, 2007.

[27] H. W. Coleman and W. G. Steele, *Experimentation, Validation, and Uncertainty Analysis for Engineers*. John Wiley & Sons, 2009.

[28] L. Kirkup, *Data Analysis for Physical Scientists: Featuring Excel®*. Cambridge University Press, 2012.

[29] B. C. Nakra and K. K. Chaudhry, *Instrumentation, Measurement And Analysis*. Tata McGraw-Hill Education, 2004.

[30] Bewoor, *Metrology & Measurement*. Tata McGraw-Hill Education, 2009.

[31] J. A. Bosch, *Coordinate measuring machines sys*. Marcel Dekker, 1995.

[32] R. J. Hocken and P. H. Pereira, *Coordinate Measuring Machines And Systems*. Taylor & Francis, 2012.

[33] "ISO 10360 - Acceptance and reverification tests for coordinate measuring machines (CMM)," *The International Organization for Standardization*.

[34] T. A. Clarke, "Non-contact measurement provides six of the best," *Quality Today*, pp. s46–s48 (July 1998).

[35] W. Osten, "Application of optical shape measurement for the nondestructive evaluation of complex objects," *Opt. Eng*, vol. 39, no. 1, pp. 232–243, Jan. 2000.

[36] J. M. Huntley, "Automated fringe pattern analysis in experimental mechanics: a review," *Journal of Strain Analysis for Engineering Design - J STRAIN ANAL ENG DESIGN*, vol. 33, no. 2, pp. 105–125, 1998.

[37] W. Linder, *Digital Photogrammetry: A Practical Course*. Springer, 2009.

[38] Y. Egels and M. Kasser, *Digital Photogrammetry*. CRC Press, 2003.

[39] T. Luhmann, S. Robson, and S. Kyle, *Close Range Photogrammetry: Principles, Techniques and Applications*. Wiley, 2006.

[40] E. M. Mikhail, J. S. Bethel, and J. C. McGlone, *Introduction to modern photogrammetry*. Wiley, 2001.

[41] C. Bräuer-Burchardt, A. Breitbarth, P. Kühmstedt, I. Schmidt, M. Heinze, and G. Notni, "Fringe projection based high-speed 3D sensor for real-time measurements," 2011, vol. 8082, pp. 808212–808212–8.

[42] K. Kraus, *Photogrammetrie Vol 1 and 2*. Ferd, Dummler Verlag, Bonn, 1996.

[43] F. Chen, "Application of least-squares adjustment technique to geometric camera calibration and photogrammetric flow visualization," 1997.

[44] K. B. Atkinson, *Close range photogrammetry and machine vision*, Illustrated edition. Whittles Publishing, 2001.

[45] B. Triggs, P. F. McLauchlan, R. I. Hartley, and A. W. Fitzgibbon, "Bundle adjustment - a modern synthesis," in *Proceedings of the International Workshop on Vision Algorithms: Theory and Practice*, London, UK, UK, 2000, pp. 298–372.

[46] R. Hartley and A. Zisserman, *Multiple view geometry in computer vision*, 2nd ed. Cambridge University Press, 2004.

[47] C. S. Fraser, "Multisensor system self-calibration," 1995, vol. 2598, pp. 2–18.

[48] C. S. Fraser, "Digital camera self-calibration," *ISPRS Journal of Photogrammetry and Remote Sensing*, vol. 52, no. 4, pp. 149–159, Aug. 1997.

[49] R. Hartley and P. Sturm, *Triangulation*, vol. Computer Analysis of Images and Patterns: 7th International Conference, CAIP '97, Kiel, Germany, September 10–12, 1997. Proceedings. Springer Science & Business Media, 1997.

[50] J. Heikkila, "Geometric camera calibration using circular control points," *IEEE Transactions on Pattern Analysis and Machine Intelligence*, vol. 22, no. 10, pp. 1066 – 1077, Oct. 2000.

[51] F. Remondino and S. Fraser, "Digital camera calibration methods: considerations and comparisons."

[52] Y. Abdel-Aziz and H. Karara, "Direct linear transformation from comparator coordinates into object space coordinates in close-range photogrammetry," presented at the Proceedings of the Symposium on Close-Range photogrammetry, 1971, vol. 1, p. 18.

[53] J. M. Huntley, "Bundle adjustment method based on object-side ray tracing." Phase Vision Ltd, Loughborough, UK, 2005.

[54] B. Triggs, P. F. McLauchlan, R. I. Hartley, and A. W. Fitzgibbon, "Bundle Adjustment — A Modern Synthesis," in *Vision Algorithms: Theory and Practice*, B. Triggs, A. Zisserman, and R. Szeliski, Eds. Springer Berlin Heidelberg, 2000, pp. 298–372.

[55] J. McKeown, D. Meegan, and D. Sprevak, *An introduction to unconstrained optimisation*, 1st ed. Taylor & Francis, 1990.

[56] S. Zhang and P. S. Huang, "Novel method for structured light system calibration," *Opt. Eng. 45(8) pp.083601-1-083601-8*, 2006.

[57] J. X. Fengkai Ke, "A fast and accurate calibration method for the structured light system based on trapezoidal phase-shifting pattern," *Optik - International Journal for Light and Electron Optics*, vol. 125, no. 18, 2014.

[58] T. Liu, L. N. Cattafesta, III, R. H. Radeztsky, and A. W. Burner, "Photogrammetry Applied to Wind Tunnel Testing," *AIAA J*, vol. 38, pp. 96497–1, 2000.

[59] J. Sun, Q. Liu, Z. Liu, and G. Zhang, "A calibration method for stereo vision sensor with large FOV based on 1D targets," *Optics and Lasers in Engineering*, vol. 49, no. 11, pp. 1245–1250, Nov. 2011.

[60] G. Z. Zhen Liu, "Novel calibration method for non-overlapping multiple vision sensors based on 1D target," *Optics and Lasers in Engineering - OPT LASER ENG*, vol. 49, no. 4, pp. 570–577, 2011.

[61] Y. A. P. Baker, "Complete calibration of a multi-camera network," pp. 134 – 141, 2000.

[62] E. Klaas, K.-P. Erben, and S. Zinck, "Robotic Scanning Using a White Light Scanner | Quality Digest." [Online]. Available: http://www.qualitydigest.com/inside/cmsc-article/robotic-scanning-using-white-light-scanner.html. [Accessed: 12-Apr-2015].

[63] L.-C. Chen and C.-C. Liao, "Calibration of 3D surface profilometry using digital fringe projection," *Meas. Sci. Technol.*, vol. 16, no. 8, p. 1554, Aug. 2005.

[64] R. Sitnik, "Digital fringe projection system for large-volume 360-deg shape measurement," *Optical Engineering*, vol. 41, no. 2, p. 443, Feb. 2002.

[65] P. S. Huang, "Calibration of a three-dimensional shape measurement system," *Optical Engineering*, vol. 42, no. 2, p. 487, Feb. 2003.

[66] A. Godhwani, G. H. Bhatia, and M. W. Vannier, "Calibration of a multisensor structured light range scanner," *Opt. Eng*, vol. 33, no. 4, pp. 1359–1367, 1994.

[67] A. M. M. R. J. Valkenburg, "Accurate 3D measurement using a structured light system," *Image and Vision Computing*, vol. 16, no. 2, pp. 99–110, 1998.

[68] M. A. Penna, "Camera calibration: a quick and easy way to determine the scalefactor," *Pattern Analysis and Machine Intelligence, IEEE Transactions on*, vol. 13, no. 12, pp. 1240–1245, 1992.

[69] G. Xu, Y. Inoue, and H. Teramoto, "Determining Camera Intrinsic and Extrinsic Parameters from Multiple Images of Multiple Balls," *Workshop on science of computer vision,* Sep. 2002.

[70] H. Zhang, K. K. Wong, and G. Zhang, *Camera Calibration from Images of Spheres*. 2007.

[71] H. Zhang, K. K. Wong, and G. Zhang, *Camera Calibration from Images of Spheres: linear approaches*. 2005.

[72] B. Acko, M. McCarthy, F. Haertig, and B. Buchmeister, "Standards for testing freeform measurement capability of optical and tactile coordinate measuring machines," *Meas. Sci. Technol.,* vol. 23, no. 9, p. 094013, Sep. 2012.

[73] "VDI/VDE 2634: Optical 3-D measuring systems - optical systems based on area scanning." Aug-2002.

[74] F. Pedersini, A. Sarti, and S. Tubaro, "Accurate and simple geometric calibration of multi-camera systems," *Signal Processing 77(3) pp.309-304,* 1999.

[75] M. Machacek, M. Sauter, and T. Rosgen, "Two-step calibration of a stereo camera system for measurements in large volumes," *Measurement Science and Technology 14(9) pp.1631-1639,* 2003.

[76] H. Bakstein, "A complete DLT-based camera calibration with a virtual 3D calibration object," *Faculty of Mathematics and Physics, Charles University, Prague,* 1999.

[77] S. J. Marshall, D. N. Whiteford, and R. C. Rixon, "Assessing the performance of 3D whole body imaging systems," *Proc. 6th Numerisation 3D/scanning 2001 congress, Paris, France,* 2001.

[78] T. N. Nguyen, "Optical measurement of shape and deformation fields on challenging surfaces," Ph.D., Loughborough University, 2012.

[79] D. Menon, *Advanced structural analysis*. Indian Institute of Technology Madras: Alpha Science Internation Ltd, 2009.

[80] A. Kassimali, *Matrix analysis of structures*. Southern Illinois University - Carbondale: ITP Brooks/Cole, 1999.

[81] M. F. Thorpe and P. M. Duxbury, "Rigidity theory and applications," *Kluwer Academic / Plenum Publishers*, 1999.

[82] B. Jackson and T. Jordan, "Rigid Components in Molecular Graphs," *pp399-412, Algorithmica, Vol. 48.*, 2007.

[83] J. Graver, B. Servatius, and H. Servatius, "Graduate Studies in Mathematics - Combinatorial Rigidity," *American Mathematics Society*, 1993.

[84] P. Pearce, "Structure in nature is a strategy for design," *The MIT Press*, 1990.

[85] I. Streinu and L. Theran, "Combinatorial genericity and minimal rigidity," *pp365-374, ACM, Vol. 10.*, 2008.

[86] M. R. Hatch, "Vibration simulation using MATLAB and ANSYS," *CRC Press*, 2001.

[87] "S-12-60-N: Rod magnet Ø 12 mm H 60 mm (Neodymium magnets) - supermagnete." [Online]. Available: http://www.supermagnete.de/eng/S-12-60-N. [Accessed: 06-Oct-2013].

[88] B. J. Skinner, "Section 6: Thermal Expansion," *Geological Society of America Memoirs*, vol. 97, pp. 75–96, Jan. 1966.

[89] J. S. Dugdale and D. K. C. MacDonald, "The Thermal Expansion of Solids," *Phys. Rev.*, vol. 89, no. 4, pp. 832–834, Feb. 1953.

[90] R. A. Schapery, "Thermal Expansion Coefficients of Composite Materials Based on Energy Principles," *Journal of Composite Materials*, vol. 2, no. 3, pp. 380–404, Jul. 1968.

[91] T. A. Mary, J. S. O. Evans, T. Vogt, and A. W. Sleight, "Negative Thermal Expansion from 0.3 to 1050 Kelvin in ZrW2O8," *Science*, vol. 272, no. 5258, pp. 90–92, Apr. 1996.

[92] E. G. Wolff, *Introduction to the Dimensional Stability of Composite Materials*. DEStech Publications, Inc, 2004.

[93] G. Staab, *Laminar Composites*. Butterworth-Heinemann, 1999.

[94] T. A. Bullions, A. C. Loos, and J. E. McGrath, "Moisture Sorption Effects on and Properties of a Carbon Fiber-reinforced Phenylethynyl-terminated Poly(etherimide)," *Journal of Composite Materials*, vol. 37, no. 9, pp. 791–809, May 2003.

[95] J. L. Abot, A. Yasmin, and I. M. Daniel, "Hygroscopic Behavior of Woven Fabric Carbon-Epoxy Composites," *Journal of Reinforced Plastics and Composites*, vol. 24, no. 2, pp. 195–207, Jan. 2005.

[96] G. C. Grimes, *Composite Materials: Testing and Design (tenth Volume)*. ASTM International, 1992.

[97] A. Poenninger and B. Defoort, "Determination of the coefficient of moisture expansion (CME)," *In: Proceedings of the 9th International Symposium on Materials in a Space Environment, Noordwijk, The Netherlands. Compiled by K. Fletcher. ESA SP-540, Noordwijk, Netherlands: ESA Publications Division, ISBN 92-9092-850-6, 2003, p. 567 - 572*.

[98] S. Bell, "The Beginner's Guide to Humidity Measurement - NPL Good Practice Guide No. 124." National Physical Laboratory, 2012.

[99] R. Roy, B. K. Sarkar, and N. R. Bose, "Effects of moisture on the mechanical properties of glass fibre reinforced vinylester resin composites," *Bull Mater Sci*, vol. 24, no. 1, pp. 87–94, Feb. 2001.

[100] G. M. Cândido, M. L. Costa, M. C. Rezende, and S. F. M. Almeida, "Hygrothermal effects on quasi-isotropic carbon epoxy laminates with machined and molded edges," *Composites Part B: Engineering*, vol. 39, no. 3, pp. 490–496, Apr. 2008.

[101] "Humidity charts." Metrology laboratory, Loughborough University.

[102] L. Greenspan, "Humidity fixed points of binary saturated aqueous solutions," *J of Research, National Bureau of Standards*, pp. 81–89, 1977.

[103] A. Wexler and S. Hasegawa, *Relative humidity-temperature relationships of some saturated salt solutions in the temperature range 0 degree to 50 degrees C*. National Bureau of Standards, 1954.

[104] J. F. Young, "Humidity control in the laboratory using salt solutions—a review," *Journal of Applied Chemistry*, vol. 17, no. 9, pp. 241–245, 1967.

[105] F. E. M. O'Brien, "The Control of Humidity by Saturated Salt Solutions," *J. Sci. Instrum.*, vol. 25, no. 3, p. 73, Mar. 1948.

[106] "BS 3718:1964 - Specification for laboratory humidity ovens (non-injection type)." 1964.

[107] H. . Choi, K. . Ahn, J.-D. Nam, and H. . Chun, "Hygroscopic aspects of epoxy/carbon fiber composite laminates in aircraft environments," *Composites Part A: Applied Science and Manufacturing*, vol. 32, no. 5, pp. 709–720, May 2001.

[108] P. Vaddadi, T. Nakamura, and R. P. Singh, "Inverse Analysis to Determine Hygrothermal Properties in Fiber Reinforced Composites," *Journal of Composite Materials*, vol. 41, no. 3, pp. 309–334, Feb. 2007.

[109] D. Stewart, "A Platform with Six Degrees of Freedom," *Proceedings of the Institution of Mechanical Engineers*, vol. 180, no. 1, pp. 371–386, Jun. 1965.

[110] E. H. Anderson, M. F. Cash, J. L. Hall, and G. W. Pettit, "Hexapods for precision motion and vibration control," *CSA Engineering Inc.*, 1993.

[111] K. Liu, J. M. Fitzgerald, and F. L. Lewis, "Kinematic analysis of a Stewart platform manipulator," *IEEE Transactions on Industrial Electronics*, vol. 40, no. 2, pp. 282–293, 1993.

[112] P. Houdek, "Design and implementation issues for Stewart Platform configuration machine tools," Thesis, Massachusetts Institute of Technology, 1997.

[113] K. Liu, F. L. Lewis, and M. Fitzgerald, "Solution of nonlinear kinematics of a parallel-link constrained Stewart platform manipulator," *Circuits Systems and Signal Process*, vol. 13, no. 2–3, pp. 167–183, Jun. 1994.

[114] "PolyWorks: 3d scanner software - 3d scanning software - 3d digitizers." [Online]. Available: http://www.innovmetric.com/polyworks/3D-scanners/home.aspx. [Accessed: 09-Sep-2013].

[115] "Geomagic 3D software from 3D Systems." [Online]. Available: http://geomagic.com/en/. [Accessed: 09-Dec-2013].

[116] "Tecplot - Master the View." [Online]. Available: http://www.tecplot.com/. [Accessed: 09-Dec-2013].

[117] "MeshLab." [Online]. Available: http://meshlab.sourceforge.net/. [Accessed: 09-Dec-2013].

[118] C. B.-B. P. Kühmstedt, "Measurement accuracy of fringe projection depending on surface normal direction," *Fraunhofer IOF*, 2009.

[119] M. Sjo¨dahl and B. F. Oreb, "Stitching interferometric measurement data for inspection of large optical components," *Opt. Eng*, vol. 41, no. 2, pp. 403–408, 2002.

[120] E. R. Harold and W. S. Means, *XML in a nutshell*. Sebastopol, CA: O'Reilly, 2004.

[121] C. F. Goldfarb and P. Prescod, *The XML handbook*. Upper Saddle River, NJ: Prentice Hall, 2001.

[122] E. T. Ray, *Learning XML*. Beijing; Cambridge, Mass.: O'Reilly, 2003.

[123] C. F. Goldfarb and P. Prescod, *The XML handbook*. Upper Saddle River, NJ: Prentice Hall, 2001.

[124] "JDOM: Binaries." [Online]. Available: http://jdom.org/downloads/. [Accessed: 09-Nov-2013].